Experimental deformation of mantle minerals at simultaneous high pressure and high temperature

DISSERTATION

Zur Erlangung des akademischen Grades eines Doktors
der Naturwissenschaften
- Dr. rer. nat.-
in der Bayreuther Graduiertenschule für
Mathematik und Naturwissenschaften (BayNAT)
der Universität Bayreuth

vorgelegt von

Julia Immoor

aus Bruchhausen-Vilsen

Bayreuth, 2021

Experimental deformation of mantle minerals at simultaneous high pressure and high temperature

DISSERTATION

Zur Erlangung des akademischen Grades eines Doktors
der Naturwissenschaften
- Dr. rer. nat.-
in der Bayreuther Graduiertenschule für
Mathematik und Naturwissenschaften (BayNAT)
der Universität Bayreuth

vorgelegt von

Julia Immoor

aus Bruchhausen-Vilsen

Bayreuth, 2021

Die vorliegende Arbeit wurde in der Zeit von September 2015 bis Dezember 2021 in Bayreuth am Bayerischen Geoinstitut unter Betreuung von Herrn Prof. Dr. Hauke Marquardt angefertigt.

Vollständiger Abdruck der von der Bayreuther Graduiertenschule für Mathematik und Naturwissenschaften (BayNAT) der Universität Bayreuth genehmigten Dissertation zur Erlangung des akademischen Grades eines Doktors der Naturwissenschaften (Dr. rer. nat.).

Dissertation eingereicht am: 16. Dezember 2021

Zulassung durch das Leitungsgremium: 16. Dezember 2021

Wissenschaftliches Kolloquium: 07. März 2022

Amtierender Direktor: Prof. Dr. Hans Keppler

Prüfungsausschuss:

Prof. Dr. Hauke Marquardt	(Gutachter)
Prof. Dr. Daniel Frost	(Gutachter)
PD Dr. Catherine McCammon	(Vorsitz)
Dr. Marcel Thielmann	

Experimental deformation of mantle minerals at simultaneous high pressure and high temperature

Julia Immoor

To Rika.

Abstract

Understanding the dynamics of the solid Earth and their relation to plate tectonics requires an understanding of the processes that occur in Earth's lower mantle. For example, seismic anisotropy observations can be used to map mantle flow patterns. However, not all these observations could be interpreted until now, such as the observed anisotropies at the edges of the Large Low Shear Velocity Provinces (LLSVP), where the origin of the shear wave splitting is unclear. Crystallographic preferred orientation of minerals can produce shear wave splitting and might help to understand the source. For this, the deformation behaviour of the mineral phases of the lower mantle need to be studied at simultaneous high pressure and high temperature.

For generating these conditions, a setup for radial diffraction experiments was used and further developed at the Extreme Conditions Beamline (ECB) P02.2 at PETRA III, DESY in Hamburg, Germany. A resistive heated diamond anvil cell provides the possibility to heat the sample evenly up to pressures and temperatures of mantle conditions. In combination with a newly developed water-cooled vacuum chamber, temperatures up to 1900 K have been reached in this thesis, while simultaneously performing *in-situ* x-ray diffraction measurements with synchrotron radiation in radial geometry. During the experiment the pressure in the DAC can be increased with a gas membrane device. The new setup was used on four different materials: (1) ferropericlase, (2) $CaSiO_3$ perovskite (synthesized from wollastonite), (3) a two-phase mixture of ferropericlase and bridgmanite, and (4) tantalum carbide.

In the framework of this thesis, I addressed several questions on the deformation behaviour of ferropericlase and cubic calcium perovskite. The experiments were carried out with graphite-heated diamond anvil cells. *In-situ* deformation experiments were done on ferropericlase and calcium perovskite at mantle conditions. The generated diffraction images were analysed with the software MAUD to obtain texture, inverse pole figures, cell parameters and lattice strains. Modelling of the experimental results was done using an Elasto-Viscoplastic Self Consistent code to simulate the texture development and lattice strain evolution in ferropericlase and calcium perovskite.

Four experiments with ferropericlase at different temperatures were examined. With the increase of pressure a texture development in the sample was observed. By combining the experimental data and modelling, data slip system activities were extracted. A change of slip systems with an increase in pressure and, above all, in temperature takes place in ferropericlase. At low temperatures the slip system $\{110\}<1\bar{1}0>$ is fully active. With an increase in temperature, there is an increase of $\{100\}<011>$ slip system. This means, slip can occur along $<110>$ directions on either the $\{100\}$ or the $\{110\}$ planes, i.e. the slip systems $\{100\}<011>$ and

{110}<1$\bar{1}$0> are likely both active at high temperatures. This change in slip system behaviour might explain shear wave splitting in the lower mantle.

Calcium perovskite forms a tetragonal structure at ambient conditions, whereas it is cubic at high pressures and high temperatures in the lower mantle. Considering this fact, a successful *in-situ* synthesis of cubic calcium perovskite is the basis of all further investigations. We were able to synthesize the cubic phase at 1150 K and pressures of the mantle. Crystallographic preferred orientation development with rising pressure was observed, suggesting that plastic deformation occurred in the sample. The plastic strength of $CaSiO_3$ perovskite has been derived from the experimental data. The results show a remarkable difference in strength between the tetragonal phase at room temperature and the cubic high-pressure, high-temperature phase. Compared to the other mantle minerals ferropericlase and bridgmanite, calcium perovskite is the weakest phase showing the lowest plastic strength. The transformation from garnet to calcium perovskite in a slab could therefore have an impact on the deformation behaviour of a subducting slab and influence the fate of oceanic crust subducted into the lower mantle.

Zusammenfassung

Um die Dynamik der festen Erde und ihre Beziehung zur Plattentektonik zu verstehen, müssen die Prozesse im unteren Erdmantel verstanden werden. So können beispielsweise seismische Anisotropiebeobachtungen genutzt werden, um Strömungsmuster im Erdmantel zu kartieren. Allerdings konnten bisher nicht alle dieser Beobachtungen interpretiert werden, wie z. B. die beobachteten Anisotropien an den Rändern der Gebiete mit niedriger Scherwellengeschwindigkeit (Large Low Shear Velocity Provinces, LLSVP), in welchen der Ursprung der Scherwellenaufspaltung unklar ist. Die kristallographische Vorzugsorientierung von Mineralen kann zu einer Aufspaltung der Scherwellen führen und könnte dazu beitragen den Ursprung der Schwerwellenaufspaltung zu verstehen. Dazu muss das Verformungsverhalten der Mineralphasen des unteren Erdmantels bei gleichzeitig hohem Druck und hoher Temperatur untersucht werden.

Um diese Bedingungen zu erzeugen, wurde ein Aufbau für radiale Beugungsexperimente verwendet und an der Extreme Conditions Beamline (ECB) P02.2 bei PETRA III, DESY in Hamburg, Deutschland, weiterentwickelt. Eine widerstandsbeheizte Diamantstempelzelle bietet die Möglichkeit, die Probe gleichmäßig bis zu Drücken und Temperaturen von Mantelbedingungen zu erhitzen. In Kombination mit einer neu entwickelten wassergekühlten Vakuumkammer wurden in dieser Arbeit Temperaturen bis zu 1900 K erreicht. Gleichzeitig wurden *in-situ* Röntgenbeugungsmessungen mit Synchrotronstrahlung in radialer Geometrie durchgeführt. Während des Experiments kann der Druck in der Diamantstempelzelle mit einer Gasmembranvorrichtung erhöht werden. Der neue Aufbau wurde für vier verschiedene Materialien verwendet:

Ferroperiklas, $CaSiO_3$-Perowskit (synthetisiert aus Wollastonit), ein Zweiphasengemisch aus Ferroperiklas und Bridgmanit sowie Tantalkarbid.

Im Rahmen dieser Arbeit befasste ich mich mit Fragen zum Verformungsverhalten von Ferroperiklas und kubischem Calcium-Perowskit. Dazu wurden Experimente mit graphitbeheizten Diamantstempelzellen durchgeführt. *In-situ*-Verformungsexperimente wurden an Ferroperiklas und Calcium-Perowskit unter Mantelbedingungen durchgeführt. Die erzeugten Beugungsbilder wurden mit der Software MAUD analysiert, um Texturinformationen, inverse Polfiguren, Zellparameter und Gitterdehnungen zu erhalten. Die Modellierung der experimentellen Ergebnisse erfolgte mit Hilfe eines Elasto-Viscoplastic Self Consistent Codes, um die Texturentwicklung und die Entwicklung der Gitterdehnung in Ferroperiklas und Calcium-Perowskit zu simulieren.

Es wurden vier Experimente mit Ferroperiklas bei verschiedenen Temperaturen untersucht. Mit der Erhöhung des Drucks wurde eine Texturentwicklung in der Probe beobachtet. Mit Hilfe der Kombination von experimentellen Daten und Modellierung wurden die Aktivitäten der Gleitsysteme extrahiert. Bei Ferroperiklas findet ein Wechsel der Gleitsysteme mit einer Erhöhung des Drucks und vor allem mit einer Erhöhung der Temperatur statt. Bei niedrigen Temperaturen ist nur das Gleitsystem $\{110\}<1\bar{1}0>$ aktiv. Bei einer Temperaturerhöhung kommt es zu einer Zunahme des $\{100\}<011>$ Gleitsystems. Das bedeutet, dass Gleiten entlang der $<110>$-Richtung entweder auf der $\{100\}$- oder der $\{110\}$-Ebene auftreten kann, d. h. die Gleitsysteme $\{100\}<011>$ und $\{110\}<1\bar{1}0>$ sind bei hohen Temperaturen wahrscheinlich beide aktiv. Diese Änderung im Verhalten der Gleitsysteme könnte die Aufspaltung der Scherwellen im unteren Erdmantel erklären.

Calcium-Perowskit bildet bei Raumtemperatur und atmosphärischem Druck eine tetragonale Struktur, während es im unteren Mantel bei hohem Druck und hohen Temperaturen kubisch ist. Eine erfolgreiche i*n-situ*-Synthese von kubischem Calcium-Perowskit ist daher die Grundlage für alle weiteren Untersuchungen. Es ist uns gelungen, die kubische Phase bei 1150 K und Drücken des Erdmantels zu synthetisieren. Eine Zunahme der Textur mit steigendem Druck wurde beobachtet, was darauf hindeutet, dass die Probe plastisch verformt wurde. Die plastische Festigkeit des $CaSiO_3$ - Perowskits wurde aus den experimentellen Daten abgeleitet. Die Ergebnisse zeigen einen bemerkenswerten Unterschied in der Festigkeit zwischen der tetragonalen Phase bei Raumtemperatur und der kubischen Phase bei hohem Druck und hoher Temperatur. Im Vergleich zu den anderen Mantelmineralen Ferroperiklas und Bridgmanit weist Calcium-Perowskit die geringste plastische Festigkeit auf. Die Umwandlung von Granat zu Calcium-Perowskit bei hohen Temperaturen und Drücken könnte sich daher auf das Verformungsverhalten einer subduzierenden Platte und auf die weitere Entwicklung der in den unteren Erdmantel subduzierten ozeanischen Kruste auswirken.

Acknowledgements

I am grateful that I could be part of this interesting and challenging project that I could grow with. First of all, I would like to thank my supervisor Prof. Hauke Marquardt (University of Oxford and Bayerisches Geoinstitut, BGI) for everything he has done for me, for his patience, the freedom to participate in conferences and workshops nationally and internationally and the really pleasant working atmosphere in his working group.

I thank Dr. Hans-Peter Liermann (Extreme Conditions Beamline, DESY) for showing me the beauty of diamond anvil cell preparation and the opportunity to learn how to make well-functioning graphite heaters. I would like to thank Dr. Sergio Speziale (German Research Centre for Geosciences) for his support during long beamtimes and instruction in loading the cells. I would further like to thank everyone who supported me during long beamtimes and nightshifts at DESY in Hamburg: Dr. Johannes Buchen (CIT), Dr. Kirsten Schulze, Dr. Alexander Kurnosov (BGI), Dr. Alba San José Méndez (DESY) and Dr. Konstantin Glazyrin (DESY). And I thank Iris Schark (DESY) and Anita Ehnes (DESY) for their technical support during the beam times. Other thanks you go to DESY colleagues Dr. Alexander Schökel, Dr. Martin Etter, Mario Wendt and Sergej Wenz, who made working at DESY feel like family.

My thanks to Prof. Sébastien Merkel (UMET - Unité Matériaux et Transformations), Dr. Nadège Hilairet (UMET), Prof. Lowell Miyagi (University of Utah) and Dr. Feng Lin (University of Utah) for introducing me to modelling and welcoming me to their cities.

Furthermore, I would like to thank Prof. Dan Frost (BGI) and Dr. Tiziana Boffa-Ballaran (BGI) for the mentorship, and Tiziana also for the profound advice.

Additionally, I would like to thank BGI stuff for their everlasting support in all administrative matters: Petra Buchert, Lydia Kison-Herzing, Janina Potzel, Dr. Stefan Keyssner and Nicole Fischer. And thanks to Detlef Krauße and Raphael Njul for handling the last-minute analysis requests. And of course, my thanks also go to all those who have shaped life at and around the BGI with me: Joana, Filippe, Stella and Fanis. Nicki, Fabian, Alex, Catherina. Iuliia, Egor, Philipp, Marcel, Niccolò, Greta, Jia, Takahiro, Sumith, Sophia and André.

Finally, I would like to thank everyone who has supported me and Rika over the last 1 ½ years, who has stood by us and without whom I would not have been able to complete this work. My thanks go in particular to: Lisa Goebel (for the supportive Corona-WG, the friendship, the phone calls, being there for each other and everything), Dr. Peter Appel (for the friendship, the refuge and safe haven in 2020 and the proofreading), Joana Polednia (who is always there for me when I need her and the proofreading), Kristin Lehner (the best and dearest neighbour, friend and "aunt" who so often had my back when I needed to catch my breath), the team of the Kinderparadies (who warmly welcomed us and supported us in every way), Heinrich and Ulrike Immoor (my parents, for all kinds of support) and Prof. Hauke Marquardt (his support and understanding for the challenging private incidents).

Contents

Figures

Tables

Chapter 1
Introduction

Earth's lower mantle plays a key role for global dynamics and is the connection between the liquid outer core and the upper mantle. It represents more than 50 % of Earth's volume and constitutes the largest geochemical reservoir for most elements. To understand global plate tectonics, knowledge of deformation behaviour of the lower mantle is needed. Heated diamond anvil cell experiments are the only possible solution to reach the high temperatures and high pressures of the lower mantle simultaneously. In this thesis I examine the deformation behaviour of two main mineral phases of the lower mantle ferropericlase and calcium silicate perovskite using an improved experimental setup.

1.1 Structure and dynamics of the Earth's mantle

Earth is special in our solar system as it has an atmosphere and active plate tectonics. Based on seismological observations, the Earth can be divided into different shells, which have significant differences in seismic velocities (Davies, 1999).

From this seismological point of view, the Mohorovičić discontinuity connects the crust, which ranges from ~5 – ~30 km depth (oceanic crust – continental crust), and the upper part of the mantle (0 – ~410 km depth) with a temperature up to ~1700 K (Clauser, 2009). The upper mantle can be divided into two dynamical layers: the lithospheric solid and therefore stiff upper part (up to ~100 km depth) and the highly viscous and plastic asthenosphere below. The upper mantle ends with the transition zone at ~410 – ~670 km depth (Figure 1.1). The lower mantle constitutes more than 50 % of Earth's volume and ranges from ~670 - ~2890 km depth with a temperature from around ~1700 – ~3500 K. Furthermore it constitutes the largest reservoir for many elements (Figure 1.1), and is composed of ~10 vol% calcium silicate perovskite $CaSiO_3$, ~25 vol% ferropericlase (Mg,Fe)O and ~65 vol% bridgmanite $(Mg,Fe)SiO_3$ (Ringwood, 1991). At around 2750 – 2891 km depth the D"- layer marks the deepest layer of the mantle, just above the core. The core is iron-rich, with an outer liquid part from ~2891 – ~5150 km depth and an inner solid part from 5150 km to the centre of the Earth at 6371 km depth. The temperature is estimated at 5000 K.

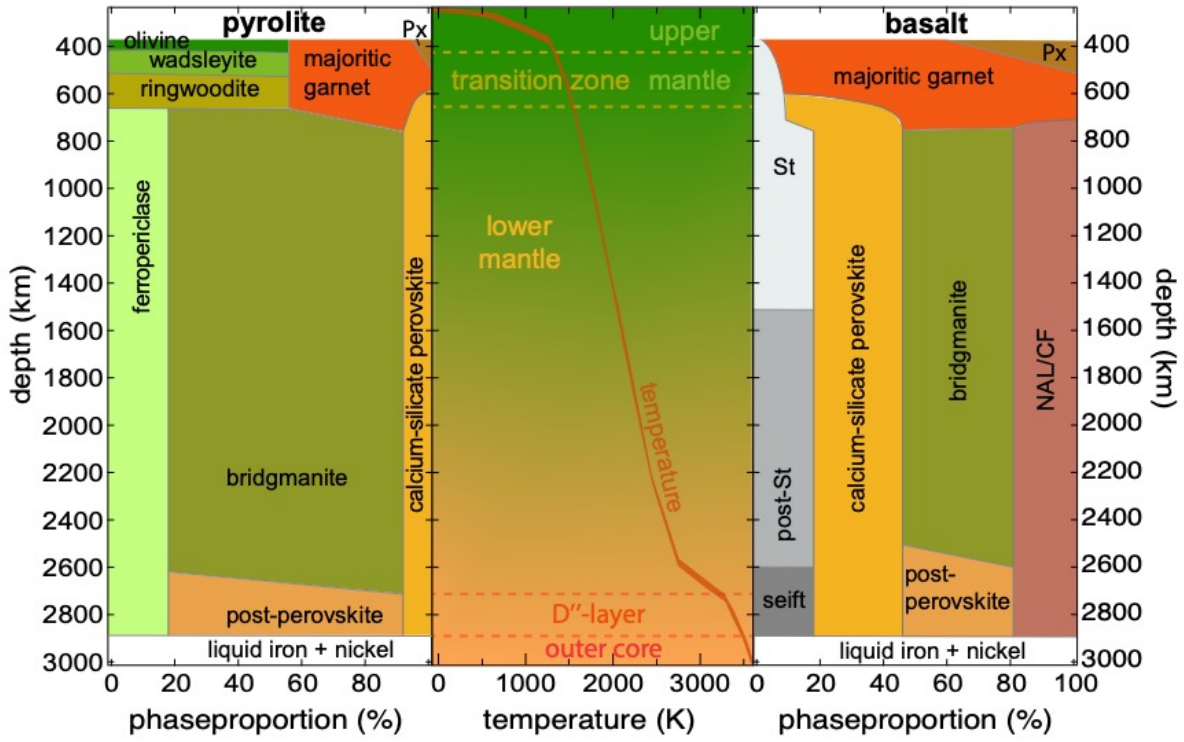

Figure 1.1: Depth-temperature-profile of the Earth (Dziewonski and Anderson, 1981; Clauser, 2009), including the upper and the lower mantle, as well as the transition zone and its mineral phases from a pyrolytic and basaltic composition; modified after Marquardt and Thomson 2020.

Mantle convection models changed and evolved during time. In the 90's Hofmann (1997) and O'Nions and Tolstikhin (1996) proposed a model with a layered Earth with convection in the upper mantle, but without connection to the lower part. However, there are seismological data, from which a mantle-wide convection flow can be derived and furthermore it seems that slabs reach the core mantle boundary (van der Hilst et al., 1997). More recent dynamic mantle model show that slabs penetrate the 660 km boundary after flattening temporarily there, because of mineral phase transition (Tackley, 2000). A similar scenario was proposed by Fukao and Obayashi, 2013 based on seismic tomography, where some subduction plates seem to stagnate at the 660 km discontinuity, whereas others penetrate it and stagnate in the lower mantle. Different seismic tomography studies suggest, that many subduction systems show the same scenario: slabs broaden and stagnate around 500 – 1000 km depth, e.g. under South America and Indonesia (Li et al., 2008; Fukao and Obayashi, 2013; Ballmer et al., 2015). The reason why this is happening is still unclear.

Carbon signatures in mantle diamonds show coherent carbon data from Earth's surface which can be related to deep mantle convection (Walter et al., 2011). To achieve a more complete image of mantle convection, the combination of geophysical observations with mineral physics and large-scale numerical models is needed.

Seismic anisotropy in Earth's lowermost mantle is among the most promising observables to map mantle flow patterns. A challenge is to pinpoint the origin of seismic shear wave anisotropy in the lowermost mantle. Is it produced by the lattice preferred orientation (LPO) of post-perovskite (Walte et al., 2009; Miyagi et al., 2010) and/or by ferropericlase (Yamazaki, 2002; Marquardt et al., 2009)? What does it mean in relation to mantle flow patterns? A solution to understand the structure of the lower mantle and its geodynamic processes is to study the occurring mineral phases and their deformation behaviour under lower mantle pressure and temperature conditions. With the help of laboratory input parameters like density or yield strength (related to viscosity), numerical modelling is becoming closer to reality (Morra et al., 2010; Marquardt and Miyagi, 2015).

1.2 Rheology of the mantle minerals

The study of the deformation behaviour of a material is called rheology. The investigation of rheological properties is needed to understand deep mantle flow mechanisms of the Earth's lower mantle. The deformation behaviour depends on the rock type, pressure, temperature, and the level of deviatoric stress. The result can be elastic to brittle failure near the surface, where pressure and temperature are low, or ductile to viscous behaviour of rocks at high pressure and temperature in the mantle. The rate of deformation, the strain rate $\dot{\varepsilon}$ can be described by (S. Karato & Wu, 1993):

$$\dot{\varepsilon} = A \left(\frac{\sigma}{G}\right)^n \left(\frac{b}{d}\right)^m \exp\left[-\frac{E^* + PV^*}{RT}\right] \qquad (1.1)$$

(original equation)

Where $\dot{\varepsilon}$ is the strain rate, σ the stress, n the stress component, A is a constant/pre-factor, G the elastic shear modulus, m the grain size dependence, b the length of the Burgers vector of the crystal structure (about 0.5 nm), d the grain size, E^* the activation energy, P the pressure, V the activation volume, R the gas constant and T the temperature. More generally, this can be described by

$$\dot{\varepsilon} = A\,\sigma^n \qquad (1.2)$$

Two main deformation mechanisms, which are strongly temperature and strain rate dependent, are important in the lower mantle. The first is deformation by diffusion creep, in which deformation is accommodated by element diffusion (Frost and Ashby, 1982) and the relationship between stress and strain rate is linear ($n=1$). Single atoms move via diffusion (vacancies) through grains or along grain boundaries, which causes plastic deformation and leads to an isotropic

structure regarding seismic wave velocities (Karato and Wu, 1993; Karato et al., 1995). One suggestion is, that this the main flow mechanism in the lower mantle (Karato and Li, 1992; Karato et al., 1995). The second is deformation by dislocation creep (or power-law creep), whereby deformation is accommodated by the motion of dislocations through grains (Frost and Ashby, 1982) and the stress dependence is nonlinear ($n \neq 1$). Dislocation creep can lead to a lattice- or crystallographic preferred orientation (LPO or CPO), which results in an anisotropic structure concerning seismic wave velocities (Karato, 1988; Karato et al., 1995). A preferred lattice orientation of crystals is consequently a response to stress. When applying stress and after reaching the critical shear stress (yield stress) crystals deform on certain preferred glide (or slip) planes along specific glide (or slip) directions. These are called active slip systems. A method to determine slip system activities is the combination of modelling and deformation experiments, where the lattice preferred orientation can be measured. Knowledge of slip system activities can be combined with single-crystal elastic properties and modelling to explain seismic anisotropy observations in the mantle link those to mantle flow patterns (Nowacki et al., 2011; Wenk et al., 2011).

Different minerals have different strength. If the strength contrast between minerals in a rock is large, the weaker phase might form thin layers in high strain areas. These layers can built an interconnected weak layer network (IWL) and can be described by theoretical models (Handy, 1994; Thielmann et al., 2020). The proposed deformation model for a two-phase mixture predicts that the weaker phase dominates the stronger one in high strain areas, where interconnected weak layers (IWL) are formed. The weaker phase forms a connecting film with homogeneous stress after large shear strain deformation (Yamazaki et al., 1999; Yamazaki and Karato, 2001b). In this case the stress is equally distributed between both phases. Another setting would be a load-bearing framework (LBF). Here, the strain rate is uniform, and the phases deform together as one unit.

1.3 Ferropericlase and calcium perovskite

In order to understand the deformation behaviour in the Earth, it is essential to understand the rheology of the occurring minerals. Ferropericlase and cubic calcium perovskite, together with bridgmanite, are the main components of a pyrolytic lower mantle (Ringwood, 1991). Cubic calcium perovskite is further an abundant mineral in the subducted basaltic crust. Even if bridgmanite is more abundant than ferropericlase (Figure 1.1, Marquardt and Thomson 2020), ferropericlase is plastically the weakest mineral phase and therefore it might play a key role in global dynamics (Karato, 1981; Handy, 1994; Takeda, 1998a; Yamazaki and Karato, 2001b; Girard et al., 2016). Previous deformation experiments on ferropericlase and cubic calcium perovskite

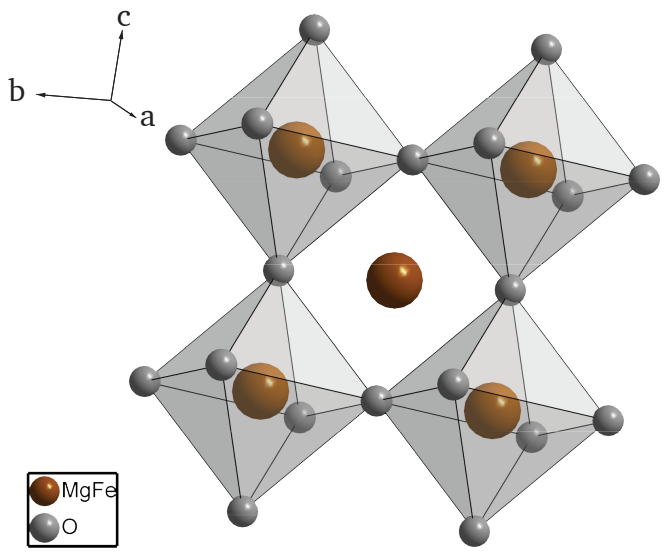

Figure 1.2: Cubic (Mg,Fe)O atomic model. Mg/Fe atoms are brown. O atoms are grey and octahedral coordinated (light grey).; (drawn from own data, Immoor et al., 2018).

were limited to room temperature and 49 GPa (calcium perovskite) and ~95 GPa (ferropericlase), because of experimental complexity (Miyagi et al., 2009; Marquardt and Miyagi, 2015). Our understanding of the high-pressure deformation behaviour of both phases is thus incomplete, particularly at high temperatures where no experimental data are published.

1.3.1 Ferropericlase

Ferropericlase (Mg,Fe)O can be formed via a complete solid solution of wüstite (FeO) and periclase (MgO) under ambient conditions (Kondo et al., 2004). In Earth's mantle, it forms by dissociation of ringwoodite (γ-$(Mg,Fe)_2SiO_4$) around the 660 km discontinuity, which decomposes into ferropericlase and bridgmanite ($(Mg,Fe)SiO_3$) (Figure 1.2) (Shim et al., 2001). Under lower mantle conditions ferropericlase forms a cubic ($a=b=c$; $\alpha=\beta=\gamma=90°$) B1 (rock salt) structure (Kondo et al., 2004).

Ferropericlase is rheologically weaker compared to bridgmanite and it might form thin layers in high strain areas, e.g. the D"-layer or around a subducting slab (Yamazaki and Karato, 2001b; Yamazaki et al., 2009; Marquardt and Miyagi, 2015; Girard et al., 2016). To evaluate such a scenario, knowledge of the high-pressure/-temperature strength is needed.

Moreover, there is also a need to identify the slip system activity of ferropericlase. The observed anisotropy in the lowermost mantle could potentially be explained with a lattice preferred orientation of this phase (McNamara et al., 2002; Yamazaki, 2002; Marquardt et al., 2009), mainly because ferropericlase shows the largest elastic anisotropy among all lower mantle phases. Many

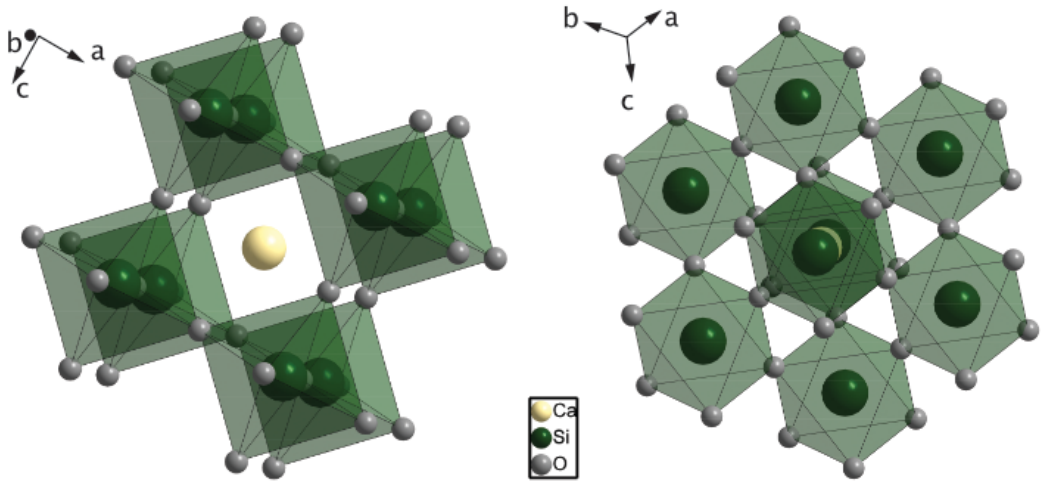

Figure 1.3: Atomic model of cubic calcium silicate perovskite in two different orientations. Yellow: Ca^{2+}, green: Si^{4+} grey: O_2. (drawn from own data: 32 GPa, cell parameter: 3.481 at 1150(±50) K).

studies have been done on periclase (Copley and Pask, 1965; Weaver and Paterson, 1969; Paterson and Weaver, 1970; Srinivasan and Stoebe, 1974) and these results can be used to get a better understanding of (Mg,Fe)O. Periclase has only one dislocation type with 1⁄2 <110> as a Burgers vector, which can glide in the planes {110}, {100} and {111} (Hirth and Lothe, 1968). One theoretical model predicts that there is a change in slip system activity of the two main slip planes {110} and {100} between 40-60 GPa: at low pressures up to 40 GPa and 0 – 1500 K the {110} slip is dominant; at pressures between 60 – 100 GPa and 0 – 3000 K the {100} slip is dominant and at high pressures up to 83 GPa and high temperatures between 1500 K – 3000 K both slip planes are active (Amodeo et al., 2012, 2016). Anyhow, these multi-scale modelling approach results need experimental verification. Furthermore, the model is related to single-crystals and it must be shown that this is also true for powders of (Mg,Fe)O.

1.3.2 Calcium perovskite

Calcium perovskite ($CaSiO_3$) forms a crystal structure with tetragonal symmetry ($a=b\neq c$, $\alpha=\beta=\gamma=90°$), at room temperature, whereas it will be cubic at temperatures typical for the lower mantle (Komabayashi et al., 2007; Thomson et al., 2019) (Figure 1.3). Calcium perovskite forms through decomposing of majoritic-garnet (Ono et al., 2001; Perrillat et al., 2006). In a pyrolytic mantle its proportion is about 10 % (Figure 1.1), in a subducted basaltic crust it is even 25 % (Irifune and Klemme, 2007). The proof of the presence of calcium perovskite in the lower mantle came in 2018 while analysing super-deep diamond inclusions (Nestola et al., 2018). A strong lattice preferred orientation of this phase may contribute to seismic anisotropy observations, particular in the shallow lower mantle or lowermost transition zone, where the elastic anisotropy of

calcium perovskite is the strongest. It is found that the shear modulus is about 26 % lower than predicted by computation models (Stixrude et al., 2007; Tsuchiya, 2011) and that the observed reduced sound velocities of subducted basaltic crust below 660 km depths (Liu et al., 2016) could be evoked by the cubic phase (Gréaux et al., 2019; Thomson et al., 2019). Calcium perovskite is not quenchable, making *in-situ* measurements inevitable. The mentioned models can only be verified by deformation experiments at pressure and temperature conditions of the lower mantle.

1.3.3 Goals of the thesis

In-situ experiments under simultaneously high pressure and high temperature are extremely challenging, hence they were mostly limited to room temperature (Wenk et al., 2000a, 2006a; Merkel, 2006; Tommaseo et al., 2006; Merkel et al., 2007). Reaching high temperatures is possible with laser heating, but the temperature gradient, as well as grain growth, makes the analysis of data difficult (Kunz et al., 2007; Miyagi et al., 2013). The aim of this thesis was to develop a new approach for a graphite heated diamond anvil cell in a vacuum chamber using radial x-ray diffraction. The graphite heater should create a good and homogeneous heat distribution in the sample. The generated data were used to quantify a potential change of slip system activities of ferropericlase and to model the fate of subducting slabs. Another goal was the *in-situ* synthesis and deformation of cubic calcium perovskite $CaSiO_3$ at lower mantle pressure of 40 GPa and temperatures about 1200 K. The experiments were complemented by modelling using the Elasto-Viscoplastic Self Consistent (EVPSC) Code to obtain the texture and lattice strain evolution in ferropericlase and calcium perovskite. A further experimental goal at simultaneously high pressure and high temperature was the deformation of bridgmanite and ferropericlase in a two-phases mixture.

Chapter 1
Introduction

Chapter 2
Experimental Methods

In 1959 a new era of high-pressure research was born, when Weir et al. (1959) invented the diamond anvil high-pressure cell (DAC). It was a small high-pressure instrument with two diamond anvils squeezed together with the help of four cubes. A sample could be placed between these anvils and the pressure was created by tightening a lever-arm type screw. A 180° opening made two things possible at the same time:

1. to check the alignment of the anvils while looking through the diamonds and
2. to increase pressure while watching the sample through the diamonds.

The pressure was the highest in the centre and the rim of the diamonds itself served as a gasket. This new technique allowed for sending an x-ray beam through the diamonds to the sample under high pressure, and with a new developed camera it was possible to capture the x- ray diffraction images (Piermarini and Weir, 1962). The pressure was calculated by:

$$P = \frac{F}{A} \tag{2.1}$$

where P is the pressure applied to the sample with the diamond with the force (F) over the area (A) of the culets. The basic principle for each diamond anvil cell is always the same. Two diamonds with its culets must be parallel, flat, and aligned with each other and a force drives the diamonds together to apply a pressure to a sample. Today different diamond anvil cells exist for different applications, e.g. the NBS (New Bureau of Standards) cell was the first diamond anvil cell ever (Weir et al., 1959), the Basset cell (Bassett et al., 1967) for x-ray powder diffraction, microscopy and phase diagram studies together with laser heated samples, the Mao-Bell cell for high pressure up to megabar scale (Mao and Bell, 1978), the Syassen-Holzapfel cell for single-crystal x-ray diffraction (Huber et al., 1977), different optical studies and Raman and Brillouin scattering, or the Merrill-Bassett cell (Merrill and Bassett, 1974), the flattest existing cell used for single x-ray diffraction studies. X-ray diffraction (XRD) enables the detection of phase transition and the identification of crystal structures. Different heating techniques exist, like internal heating with a current flow through a wire (Liu and Bassett, 1975), with electromagnetic

radiation (laser heating) (Ming and Bassett, 1974) or external heating with a resistance heater (Bassett and Takahashi, 1965; Moore et al., 1970; Hazen and Finger, 1981), each facing different challenges. Low temperature techniques exist as well. One possibility is that the sample chamber is cooled down with a cryogenic fluid like liquid nitrogen (down to -195,8 °C) or oxygen (down to -182,97 °C). Another possibility to get even colder temperatures in the DAC is to load the sample chamber with gases like neon, argon, or xenon (Mao and Bell, 1979). Any type of material, powders, or single-crystals can be analysed in a diamond anvil cell and the results used in geosciences or material sciences, for example.

This section describes the experimental method, including preparation of a resistive-heater, the newly developed vacuum chamber with its cooling system and the setup at the beamline. Without the experimental techniques described in chapter 2.2 – 2.6 it would not have been possible to carry out the high-pressure and high-temperature experiments.

2.1 General principles, radial x-ray powder diffraction in the DAC with synchrotron radiation

A lot of diamond anvil cells are used in an axial XRD scattering geometry, which means, that the beam passes through the diamonds to the sample and gets diffracted there. In this thesis, a radial geometry, where the beam passes the sample perpendicular to the compression direction, is used in combination with a resistive-heated diamond anvil cell using synchrotron radiation. Synchrotron radiation is radiation with extremely high intensity, and it can be focused down to a micrometre, so that analysis can be done on small samples The first combination of x-ray powder diffraction and synchrotron radiation was done by Buras et al. (1977).

2.1.1 X-ray diffraction

X-ray diffraction is used to examine the atomic structure of crystals, detection of phase transition, identification of crystals structures or phases, as well as measurement of the unit cell volume. X-rays are scattered by lattice planes whereby the basic principle is based on the Bragg's law (Bragg and Bragg, 1914):

$$n\lambda = 2d_{hkl}sin\theta \tag{2.2}$$

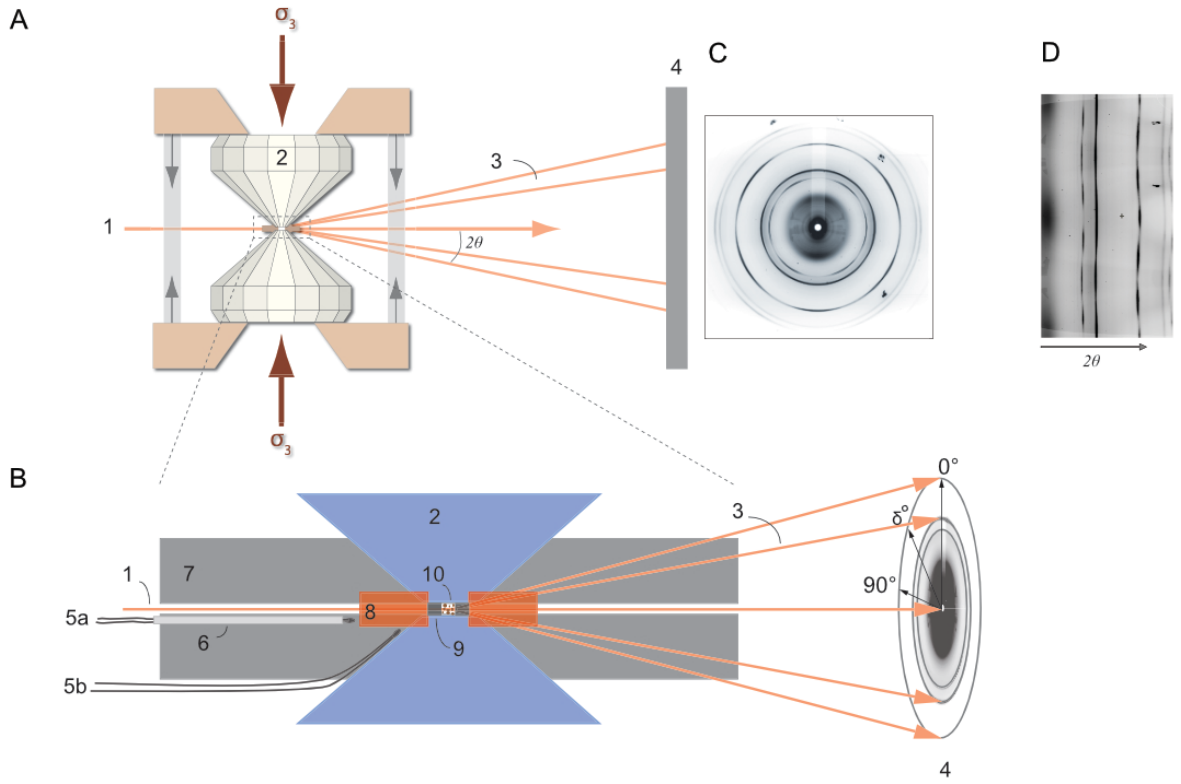

Figure 2.1: Illustration of x-ray diffraction (modified after Immoor et al., 2020 and Liermann et al., 2009. The beam is coming from the left, gets diffracted by the sample (following Bagg's law) and the diffracted beam is detected by the detector and the result is a diffraction image showing Debye rings. Larger dark spots are reflections of the diamonds. (A) large stress along the compression direction; 2θ : diffraction angle; (B) simplified close up sketch of a resistive-heated DAC with best position of the two thermocouples (one next to the culet of the cylinder, the other between both graphite sheets); (C) diffraction image (Debye-Scherrer rings) and (D) unrolled diffraction image of a powder sample of ferropericlase at 1400 K and 65 GPa.
1: incoming x-ray beam; 2: diamond anvil; 3: diffracted beam; 4: detector; 5a: thermocouple between two graphite layers; 5b: thermocouple on the diamond close to the culet; 6: ceramic sleeve; 7: graphite sheet (flexible); 8: Kapton; 9: boron gasket; 10: powder sample.

where n is an integer number mostly set to *1*, λ is the wavelength of the monochromatic x-rays, d is the distance of the lattice planes, hkl are Miller indices and indicate the lattice planes, and θ is the scattering angle. The beam passes through the sample and is reflected on the lattice planes (Figure 2.1). The reflection only occurs when the Bragg law is satisfied, which means only certain specific angles of reflection (Bragg angle) between the incoming x-ray beam and the lattice plane are allowed and constructive interference happens. The diffracted beam is detected by the detector and the result is a diffraction pattern showing Debye rings[1]. Each ring corresponds to one specific lattice plane with different Miller indices. The intensity of the rings depends on the electron distribution around each atom. Since the wavelength is always known and the diffraction

[1]family of cones around the primary beam

angle measured, the lattice spacing (d_{hkl}) can be calculated. If the crystallographic space group of the analysed sample is known as well, it is possible to calculate the unit cell with:

$$\frac{1}{d_{hkl}^2} = \frac{h^2 + k^2 + l^2}{a^2} \tag{2.3}$$

for a cubic system, with a as lattice constant The volume (V) for a cubic system can be calculated with:

$$V = a^3. \tag{2.4}$$

2.1.2 Radial x-ray diffraction

Using angle dispersive synchrotron x-ray diffraction (XRD) in a radial geometry provide the possibility of deformation experiments at simultaneously high pressure and high temperature. Figure 2.1 A shows a simplified drawing of the radial diffraction setup in a diamond anvil cell. The x- ray beam coming from the left is perpendicular to the compression direction of the diamonds, gets diffracted by the sample (following Bragg's law) and the diffracted beam is detected by the detector. The result is a diffraction image showing Debye-Scherrer rings, which are a result of many different orientated lattice planes relative to the compression axis (Wenk et al., 2006a). Experiments on polycrystalline samples in a resistive-heated diamond anvil cell were performed. This setup provides the possibility to study the lattice strains together with the lattice preferred orientation. No pressure-transmitting medium was used to enhance differential stress and texture. The deformation of the crystallites could be observed and the scattering from the lattice planes, which were in different relative orientations to the compression axis, and its change of d-spacing could be measured.

2.2 Assembly of a Mao-Bell type DAC with a graphite heating system

As mentioned above, different techniques exist for achieving high temperatures in a diamond anvil cell as mentioned above. In this thesis, a resistive-heating system was used. A Mao - Bell type diamond anvil cell was used in the experiments, made of a piston and a cylinder part (Figure 2.2 A, B), whereby the piston part slides into the cylinder part which has an opening for the diffracted beam. The setup of the graphite heating system was mostly the same on both parts: first the tungsten carbide seat, where the diamond was glued, then a ceramic plate, which separated the seat from the following flexible graphite sheet. These layers had a carved space for the x-ray beam and had a connection to the molybdenum rods (cylinder part) over a little step at the

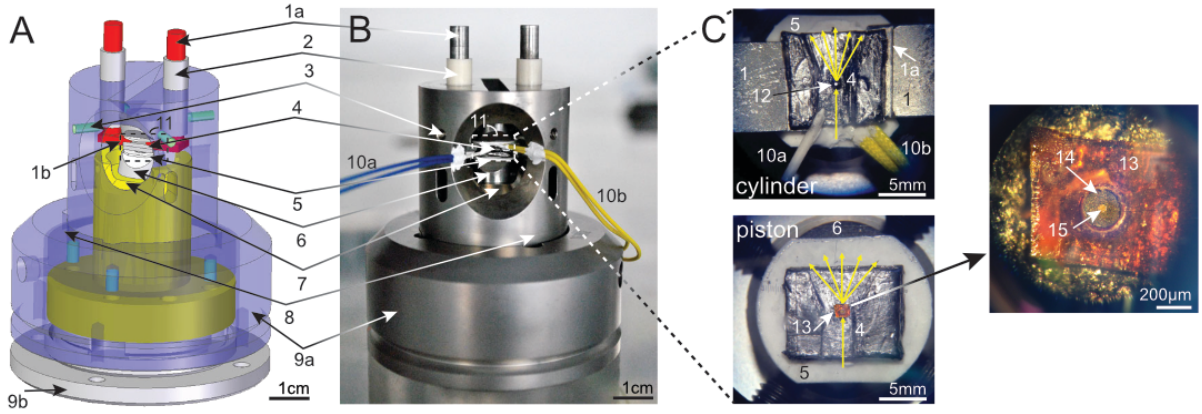

Figure 2.2: (A) 3D CAD graphic and (B) picture of the resistive-heated Mao-Bell type diamond anvil cell (modified after Immoor et al., 2020). 1a: electrical contacts (molybdenum rods); 1b: step at the ends of the electrical contacts; 2: ceramic sleeves; 3: screws for aligning the seat; 4: flexible graphite layer; 5: ceramic plate; 6: tungsten carbide seat; 7: piston; 8: cylinder; 9a: membrane cup; 9b: lid of membrane cup (missing in B); 10a: thermocouple with ceramic sleeve; 10b: thermocouple, and 11: graphite heater. (C) Close up of graphite heater (11). Cylinder part: flexible graphite layer (4) with a carved space for the x-ray and the diffracted beam (yellow arrows) and the culet of the diamond (12) in the middle. With 10a and 10b is the best position of the thermocouples illustrated. Piston part: flexible graphite layer (4) with upper diamond in the middle and a carved space for the x-rays and diffracted beam. Around the culet the Kapton (13), which supports a cubic boron nitride or amorphous boron epoxy gasket (14) with a powder sample in the sample chamber (15).

end of the rods. Two thermocouples were fixed with ceramic glue on the cylinder part: one next to the culet of the diamond, the other one on the graphite piece of the cylinder part. The latter had a protective ceramic sleeve. A closer look between the anvils at the graphite heater (Figure 2.1 B and Figure 2.2 C) shows that the sample was placed in an x- ray transparent amorphous boron epoxy gasket (aBE), held by an orange Kapton ring. The diamonds were brilliant cut gemstones with a small flat face at the tip of the diamond, called culet. They had a (100) orientation and were 16-sided of a type 1a standard design[2]. With a culet diameter of 300 µm, a pressure up to ~70 GPa could be reached, whereas a diamond with a culet diameter of 200 µm could achieve pressures up to ~100 GPa. A gas membrane was used to increase the pressure during the experiment. The molybdenum rods led the current from a power supply through the graphite sheets, inducing heating. During the experiment the temperature was measured with the thermocouples and controlled via the power supply. All parts of the graphite heater needed to be prepared for each experiment and could be used only once. The cylinder, the piston, the molybdenum rods, the membrane cup, and lid were manufactured once and could be used until material failure. Most time an experiment stopped because of diamond break down.

[2] Almax easyLab Inc., Cambridge, Massachusetts, USA, www.almax-easylab.com

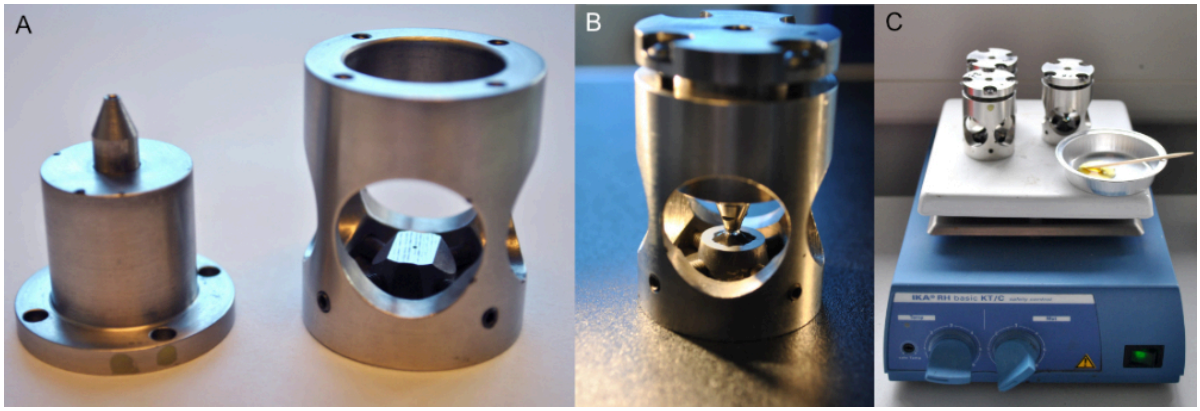

Figure 2.3: Gluing and aligning the diamond on a seat with the help of a jig. (A) upper (left) and lower part with a seat. (B) the glued diamond on the seat in the closed jig. (C) Jigs on a heating plate.

2.2.1 Preparation process of the RH-rXRD-DAC

The preparation process of the resistive-heated-radial-x-ray-diffraction-diamond-anvil-cell (RH-rXRD-DAC) began with gluing the diamonds on tungsten carbide seats. The seats are truncated at two opposite sides that the diffracted x-ray beam had a big opening angle to also collect high-angle peaks. A jig was used for the alignment and the gluing of a diamond on a seat (Figure 2.3 A). The seat had a hole, and the drilling of the hole was straight. It was put in the middle of the lower part of the jig and was fixed with four screws. The diamond was positioned in the centre of the seat and the upper part of the jig was pushed into the lower part so that the tip of the diamond could enter and be held in the tip of the jig. The screws were closed cross-diagonally to close both parts of the device. Afterwards, the jig was turned upside down to centre the diamond while the position of the seat was changed by adjusting the screws. The centre of the culet was in the centre of the hole of the seat. This needed to be double checked from both sides with one optical path of the microscope. After the diamond was aligned, all screws were tightened. For fixing the diamond on the seat, a two-component glue EPO-TEK® 353ND 8oz[3] with a mixture of Part A and Part B was used (ratio 10:1). The mixture was applied around the diamond to the belt using a toothpick (Figure 2.3 B). After ~12 hours on a 50 °C heating plate the glue had hardened and the seat with the diamond could be removed from the jig (Figure 2.3 C).

Two thermocouples were made of a platinum-rhodium wire (Pt-Pt13Rh, R-type) and a glass fibre sleeving for high-temperature applications[4]. Four wires were treated into isolation bands, each about 14 cm. Only one thermocouple got a ceramic sleeve extension with two separate holes for the wires. The ends of both thermocouples were welded together, and the resulting small metal

[3] Epoxy Technology, Billerica, USA, http://www.epotek.com
[4] OMEGA Engeneering Inc., Norwalk, USA, http://www.omega.com

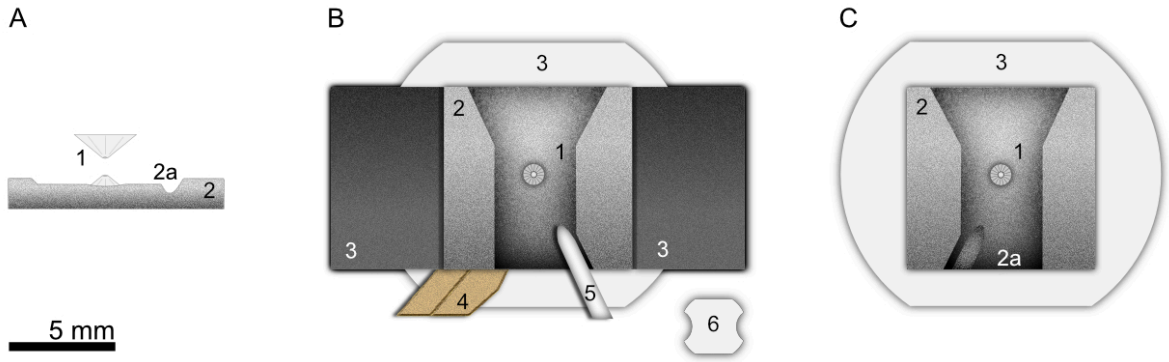

Figure 2.4: Preparing the graphite heater. (A) Frontal view of carved graphite sheet. (B) View on cylinder part with thermocouples. (C) View of piston part. 1: diamond; 2: graphite heater with space for the x-ray beam; 2a: notch for thermocouple; 3: ceramic plate; 4: thermocouple under one graphite sheet, close to the diamond; 5: thermocouple with ceramic sleeve in between the graphite sheets; 6: Reduced representation of 3 to show the drilled semicircles for the cylinder part.

balls were flattened with flat pliers. The welded end of the thermocouple with the ceramic sleeve was plunged into ceramic cement Resbond® 989[5], so that the end was isolated and preventing an electrical short in the graphite heater. A ceramic ring of about 1 cm diameter and two parallel sides was clamped in a vice and two semicircles were milled in the round sides (Figure 2.4 B: 6).

A pair of diamonds with its seats were placed on the piston and cylinder and fastened with four lateral screws. Ceramic sleeves were bonded with Ω Bond 500 liquid[6] in the cylinder part, whereby they were lower than the seats. The flattened sides of the seat were aligned with the opening of the piston and cylinder parts and the slope of the seat of the piston and cylinder were parallel to each other (Figure 2.2 A, B: 5, 6 and Figure 2.5 A: 8, 9). The set screw was used in the piston to prevent the diamonds from colliding. The piston and cylinder could be very loose, and the use of some wax balls between the windings was necessary to prevent collision. The alignment of diamonds was done in several steps. The cylinder on top and the seat of the piston were moved, while watching the tips of the diamonds through the microscope. When the alignment was good the diamond anvil cell was closed a bit more. Alignment was performed until the diamonds touched and neither optical birefringence nor first-order birefringence colours were visible.

The prepared ceramic plate was positioned on the seat and around the diamond of the piston. The plate was fixed with a thin layer of Ω Bond 500 and lay flat on the seat surface with the straight sides aligned parallel to the ramps of the seat (Figure 2.2 C: 5, 6). The base for the graphite heating system was the ceramic cement which created a smooth connection between the diamond and the ceramic plate at the piston part. The short heads of the electrical contacts

[5] Final Advanced Materials, Didenheim, France, http://www.final-materials.com
[6] OMEGA Engineering, Deckenpfronn, Germany, https://www.omega.de/

were glued with Ω Bond 500 in ceramic rolls and touched the ceramic plate (Figure 2.5 A: 4, 8, 10). A membrane cup was attached at the cylinder with a set screw which held the cup during the whole preparation process in place. This is essential because the cup could not be attached after the thermocouples were fixed. A smooth connection between the diamond and the ceramic plate was also made on the cylinder part. At the same time, the flat end of the first thermocouple was fixed next to the diamond tip with Resbond® 989, coming from the left side of the opening. The alumina sleeves served always as insulation from electrical current and heat.

2.2.2 Graphite heating system

Two pieces of the flexible graphite were cut with scissors. For the piston a piece of 9 mm x 7 mm and for the cylinder a piece of 11 mm x 7 mm was cut. The pieces of graphite were pressed on each diamond to create an imprint. These imprints were carved conically with a sharp scalpel so that the diamonds would blend in well with the layers. The graphite pieces were attached to the ceramic bases with some superglue. The graphite in the cylinder touched the steps of the rods to make an electrical connection. In both parts a path was cut respectively: one for the incoming beam and one for the diffracted beam passing through. To prevent diffraction of the graphite and therefore disturbing the diffraction image, the whole graphite had to be planar and without scales. In the graphite of the cylinder a notch was cut at the right side for the second thermocouple with the ceramic sleeve, which was fixed with some tape at the opening of the cylinder (Figure 2.4 A, B). The thermocouples did not block the beam path. The next step was closing the cell carefully so that an imprint of the thermocouple was created in the graphite of the piston (Figure 2.4 C). This imprint was deepened with a scalpel to allow the two flexible graphite sheets to touch each other when the diamond anvil cell was closed. The thermocouples were glued with ceramic glue to the opening of the cylinder part.

Before loading the cell, the resistance was measured with a multimeter between the thermocouples and the rods with a resulting resistance is around some MΩ, between the two rods there was a resulting moderate resistance in the kΩ range, and the maximum resulting resistance between the two thermocouples was ~ 5 Ω.

2.2.3 Loading the DAC

A hole of ~200 µm diameter (d_b) was drilled in a small ~150 µm thick, x-ray transparent piece of Kapton with a drilling machine. This sheet of Kapton needed to fit in the graphite heating system and had a rectangular shape of 1 mm x 2,5 mm and served as holder for the gasket. The

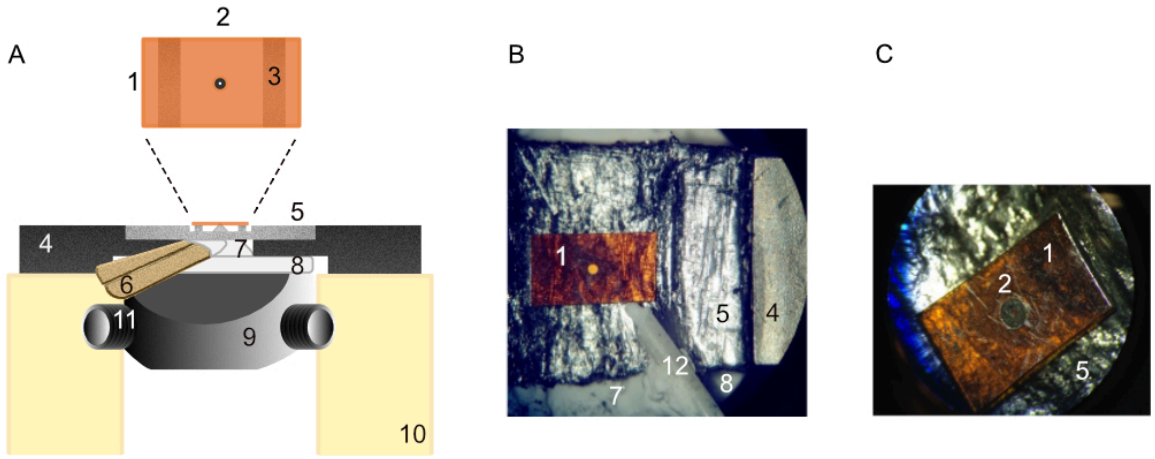

Figure 2.5: Graphite heater with Kapton and thermocouples. A: frontal view of a graphic. 1: Kapton; 2: aBE or cBN gasket; 3: graphite bridge; 4: electrical contacts of the rods; 5: graphite layers; 6: thermocouple next to the culet with glass fiber sleeving; 7: diamond; 8: ceramic plate; 9: tungsten carbide seat; 10: ceramic sleeve; 11: screw. B: top view picture. 12: thermocouple with ceramic sleeve between both graphite sheets. C: picture of close view through a microscope of Kapton with aBE gasket.

gasket with its sample chamber is positioned between the diamond tips and will seal the diamonds. The gaskets used in the described experiments consisted of amorphous boron epoxy aBE (Merkel and Yagi, 2005) or cubic boron nitride cBN, which support the sample up to 135 GPa (Funamori and Sato, 2008; Miyagi et al., 2013). The gaskets diameter was (Merkel and Yagi, 2005):

$$d_b = d_d + 50\ \mu m \tag{2.5}$$

with d_d as diameter of the culet of the diamond, a thickness of ~50 µm with sample chamber of ~80 – 100 µm diameter. The aBE gasket needed lateral support of a Kapton piece because the gasket alone would not hold the strain under these extreme temperature and pressure conditions and would fail (Merkel and Yagi, 2005). Both gaskets are x-ray transparent, are stable at high pressures and high temperatures, and have their own advantages, depending on the application. The cBN gasket is mechanically stable and has good strength at high temperatures and high pressures. It reacts into a glass at high temperatures, without losing the sample support and it can be used for laser heating because it will not interact with the heating laser. However, the diffraction peaks overlap with sample peaks, which made the amorphous boron gasket handier because there are no diffraction peaks. When the Kapton was not stable lying on the diamond it was necessary to build a bridge with small supports of graphite (Figure 2.5 A). The Kapton was placed on the bridge and was fixed with a tiny drop of superglue on the edge. The glue should not be on top of the culet or around the Kapton. When everything was dry, the DAC was closed again to check whether everything was still aligned and in place. The cell was either loaded with sample powder alone or with the sample powder and platinum powder that acted as a pressure

standard. A thin needle was used to add some of the sample into the sample chamber in the gasket. For final closure Molykote®[7] was applied on the outside of the piston to protect the piston and cylinder from sticking together during the high-temperature experiments. All samples were precompressed between 5 – 30 GPa, when the cell was finally closed. The second last step was attaching the gas membrane device around the piston part. The set screw was removed, and the membrane capillary was properly oriented relative to the orientation of the cell in the vacuum chamber later, so that it blocked neither the incoming nor the diffracted x-ray beam. The cap was closed parallel to the cell body with four screws without washers. The final step was connecting the luster terminal to the ends of the thermocouples.

2.3 Vacuum chamber

One of the biggest challenges when heating a diamond anvil cell is the oxidation process. The whole cell is heated and with it the diamonds, the surrounding parts, and the molybdenum rods. Diamonds oxidate in air during heating and above 800 °C the transformation to graphite begins (Evans, 1976; Jayaraman, 1983; Kumar et al., 1996). They become less hard and lose their strength (Liermann et al., 2009; Miyagi et al., 2013).

A vacuum chamber was developed by the sample environment group at PETRA III and implemented at the Extreme Condition Beamline P02.2 at PETRA III, Deutsches Elektronen Synchrotron (DESY) in Hamburg, Germany (Figure 2.6). The chamber is made for deformation experiments with RH-rXRD-DACs at simultaneously high pressure and high temperature to prevent oxidation processes of the used cell, the diamond anvils, the molybdenum rods and the graphite heater (Immoor et al., 2020). Using this chamber, the thermal expansion of the piston during the heating process is reduced and therefore the friction between the cylinder and piston. This leads to a smoother increase in pressure during the experiment. The chamber is connected to a pump which creates a nearly stable vacuum up to 10^{-4} mbar next to the pump. The vacuum around the diamond anvil cell may be a little lower due to connections between the pump and the vacuum chamber. Nevertheless, the vacuum is still good enough to avoid most of the oxidation processes. Furthermore, the base of the vacuum chamber is connected to a water-cooling system. A steel pin at the base is holding the diamond anvil cell and cools it indirectly, while the inside around the sample can be heated. The chamber with all connectors has a size of 412 mm x 185.24 mm x 270.16 mm (length, width, height) and is mostly made of steel and copper. The lid is closed with 16 screws and nuts. It has eight water-cooling inlets and outlets that are connected with

[7] DuPont de Nemours, Inc., Wilmington, USA, https://www.dupont.com

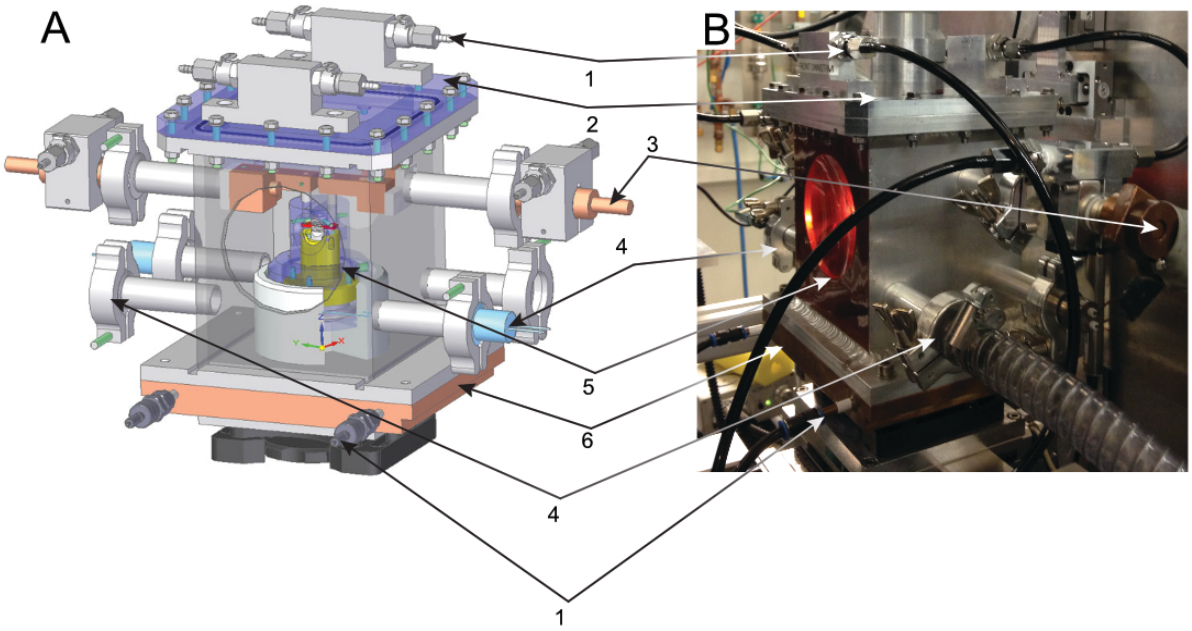

Figure 2.6: 3D CAD – graphic (A) and a picture while running a high-temperature (~1400 K) experiment (B) of the vacuum chamber for resistive-heated diamond anvil cell in and radial x-ray diffraction geometry for synchrotron radiation, with 412 mm x 185.24 mm x 270.16 mm (length, width, height). 1: Water cooling connectors, 2: lid with 16 screws, 3: copper power supply connectors, 4: connection to vacuum pump, 5: big Kapton window (outcoming beam) and 6: copper cooling plate (Immoor et al., 2020).

hoses. There are two Kapton windows (Figure 2.6 no. 5) through which the synchrotron beam can enter and exit the chamber with a 70° opening on the detector side. The power supply connector and the cooling plate are made of copper for a better temperature transfer. The vacuum is pumped through four vacuum pump connections. The setup can be moved in three different directions (x, y, z) and the sample can be observed throughout the experiment with a camera placed above the cell.

2.4 Setup at the beamline

The diamond anvil cell was positioned in the vacuum chamber (Figure 2.7). The side for the incoming beam path of the diamond anvil cell was aligned with the small Kapton window and the other side for the diffracted beam with the large Kapton window of the chamber. The thermocouples were brought into line towards the incoming synchrotron beam so that they could not block the beam path and were connected to the plugs of the chamber. The cell was fixed with a set screw in the bottom of the chamber (Figure 2.7 B no. 8). The heating rods were connected to the cell and the resistance was measured between the power rods of about the value of the graphite heater in moderate kΩ. The resistance between the power rods and the rest of the chamber and cell should be in the MΩ range. The gas membrane device was connected to the pump

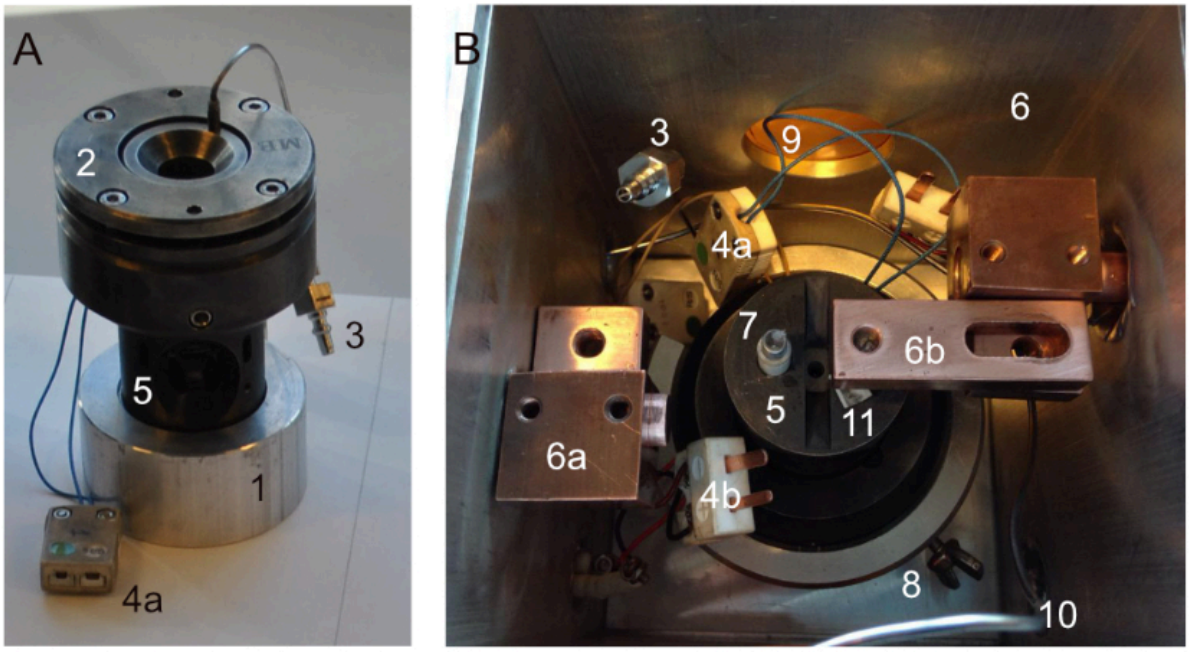

Figure 2.7: A: Completely prepared DAC on a holder (1) with membrane and piston inside the membrane cup (2), its connection (3) and with the thermocouple connectors (4a). B: DAC in the vacuum chamber (6). 4b: vacuum chamber connectors to thermocouples; 5: cylinder; 6a, b: copper piece for fixing and connecting power supply with electrical contacts (7) of the DAC; 8: set screw for fixing the DAC in the vacuum chamber; 9: small Kapton window for incoming x-ray beam; 10: connecting gas membrane pipe of the vacuum chamber; 11: broken part of ceramic sleeve of one electrical contact.

for creating the vacuum. The lid was placed on the housing of the chamber and fastened with 16 screws, tightening these only gradually in several passes. The water hoses were connected and the chamber with the three spheres below the kinematic plate was placed on the beamline. After fixing the vacuum chamber on the stage, the microscope was moved down and the cell with the sample was aligned. Afterwards the water-cooling connections were coupled and turned on. The following steps were plugging-in the membrane, hooking-up the thermocouples and membrane with the pumping station. The vacuum was switched on. When a stable vacuum of 10^{-4} mbar was reached, the power cables were connected to the ultra-stable DC power supply (Liermann et al., 2015), and the rings were attached so tightly to the cable that nothing could move during the experiments and moving the chamber.

After mounting the vacuum chamber on the general-purpose station at the Extreme Condition Beamline, all instruments were controlled remotely in the control room. X-ray energies of 25 or 43 keV were used and the beam was focused to about 7.5 – 8 (h) by 2 – 3 (v) μm^2. Diffraction images were collected with a XRD 1621 flat panel detector from Perkin Elmer[8] (Liermann et al., 2009; Merkel et al., 2013; Miyagi et al., 2013). A camera transmits the values of the *in-situ* vacuum gauge in the chamber to a monitor in the control room. During the experiment the

[8] PerkinElmer, Inc., Walluf, Germany, https://www.perkinelmer.com

chamber provides a stable vacuum of 10^{-4} mbar. The temperature was changed by an analogue I/O signal from 0 V to 10 V and is connected to the DC power supply Type 6674A from Agilent Technology[9] which operates simultaneously and was adjusted from 0 W to 1800 W (0 – 8 V and 0 – 220 A) (Liermann et al., 2015). It is operated by a general-purpose interface bus (GPIB) and by a thermocouple recording system, with a Keithley 3706A[10] with a cold junction correction for R-type thermocouples. Increasing and decreasing pressure was done by a gas membrane device which was regulated by APD 200 from Sanchez Technology[11], a gas membrane control system (Liermann et al., 2009; Merkel et al., 2013; Miyagi et al., 2013). Depending on the goal of the experiment there were different procedures to increase temperature and pressure. In some, the temperature was increased over several hours so that system of the sample could equilibrate, after the target temperature was reached, the temperature was kept constant. In others, temperature and pressure were increased at the same time. To get a good overview of the texture and strain evolution the collection of diffraction images were collected in many regular pressure steps.

2.5 Starting material of the experiments

Ferropericlase, $CaSiO_3$, enstatite and tantalum carbide were used as powder samples in the diamond anvil cell experiments. The starting materials needed to be prepared before they could be loaded in the cell.

The ferropericlase composition $Mg_{0.8}Fe_{0.2}$ was synthesized from the oxides MgO and Fe_2O_3 at high pressure and high temperature in the piston cylinder press at the Bavarian Research Institute of Bayreuth (BGI). MgO and Fe_2O_3 were stoichiometrically mixed with a ratio of 0.8 and 0.2. The mixture reacted in a gas-mixing furnace at 1250°C at an oxygen fugacity 2 log units below the fayalite-magnetite oxygen buffer to $Mg_{0.8}Fe_{0.2}$ (Marquardt and Miyagi, 2015). $Mg_{0.8}Fe_{0.2}$ ferropericlase was grounded into fine powder.

$CaSiO_3$ calcium perovskite was synthesized during the high-pressure and high-temperature experiments in the diamond anvil cell (Immoor et al., (n.d.); Uchida et al., 2009). It is not possible to quench it at ambient conditions. The starting material for the cubic phase was a finely-ground wollastonite $CaSiO_3$ powder and platinum was added as a pressure marker for the experiments.

- $CaSiO_3$ calcium perovskite was synthesized during the high-pressure and high-temperature experiments in the diamond anvil cell (Immoor et al., (n.d.); Uchida et al., 2009). It is not possible to quench it under ambient conditions. The starting material for the cubic

[9] Agilent, Santa Clara, USA, https://www.agilent.com
[10] TEKTRONIX, INC., Beaverton, USA, https://www.tek.com
[11] SANCHEZ TECHNOLOGIES, VIARMES, France, https://www.corelab.com

phase was a finely-ground wollastonite $CaSiO_3$ powder and platinum was added as a pressure marker for the experiments.

- To analyse the assembly of $MgSiO_3$ bridgmanite and ferropericlase a starting material of enstatite glass powder mixed with ferropericlase powder was used.
- The starting material of studying tantalum carbide was a fine powder of $TaC_{0.99}$ and an added a tiny gold foil to estimate the pressure during and after the experiments. This was an extra experiment which evolved during the thesis to show the possible scope of experiments with this novel technique.

2.6 Data analysis

The experimental high-pressure and high-temperature radial x-ray powder diffraction pattern were fitted with the software Material Analysing Using Diffraction (MAUD) (Lutterotti et al., 1997, 2014; Wenk et al., 2014) to extract texture, (Figure 2.8 C), cell parameters, phase proportion and lattice strains. Intensity variations along the rings represent texture variations. A result of the effect of differential stress is the development of lattice strains, visible as elliptical distortion of the Debye rings. The experimental derived results were further simulated with the Elastic-Viscoplastic Self-Consistent (EVPSC) code (Wang et al., 2010). The code is an extension of the Elasto-plastic self-consistent (EPSC) code (Turner and Tomé, 1994) and the Viscoplastic self-consistent (VPSC) code (Lebensohn and Tomé, 1994). The crystallographic preferred orientation can be modelled, and the evaluation of texture observed during different pressure steps. By combining the measured data with EVPSC slip system activities were extracted.

2.6.1 MAUD

A detailed analysis of the collected diffraction images was carried out using the program MAUD, which minimizes the difference between a calculated profile and the observed data profile with the least squares technique, in which the entire peak profile was used (Rietveld, 1969; Lutterotti et al., 1997, 2014; Wenk et al., 2014). The analysing process was followed by the instructions of Lutterotti et al., 2014 and Wenk et al., 2014. The program refines parameters e.g., background,

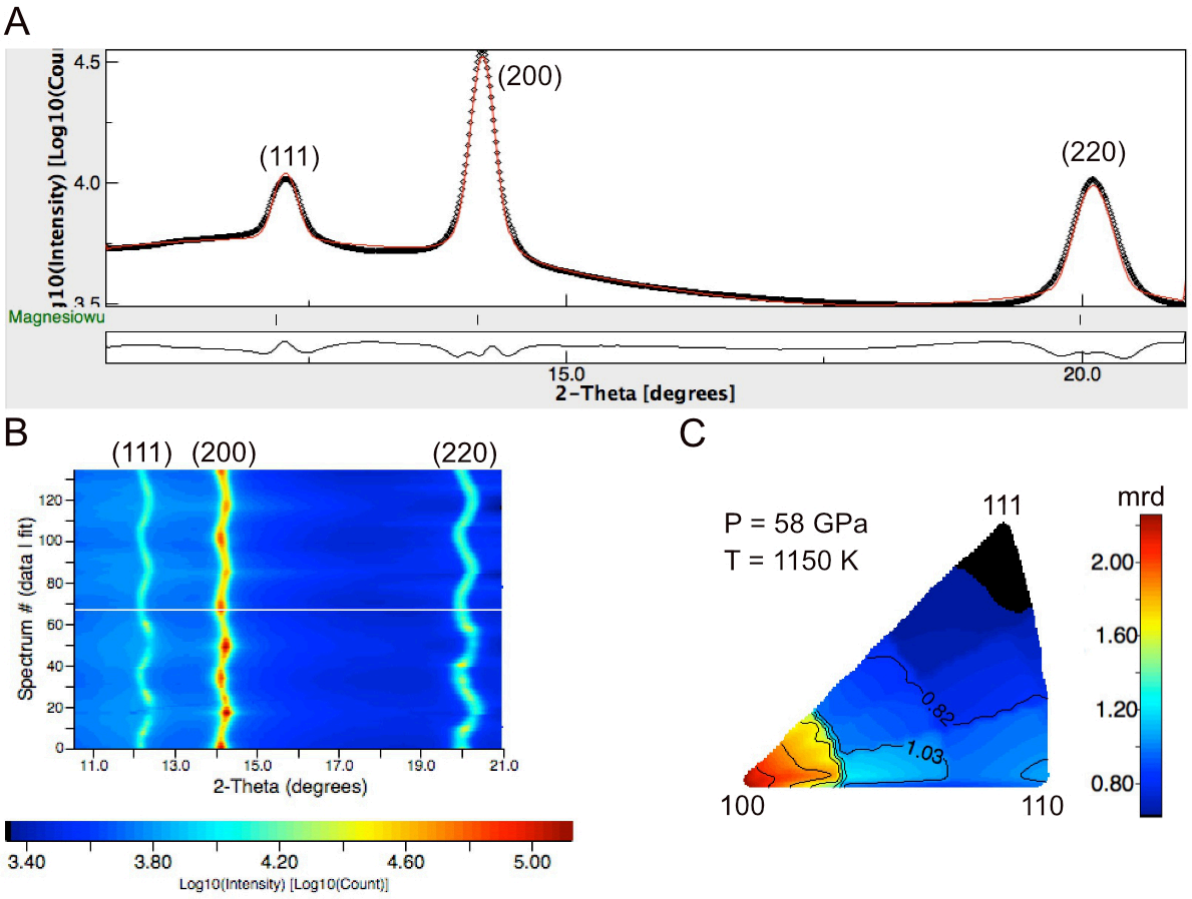

Figure 2.8: MAUD results of a ferropericlase powder sample at 1150 K and 58 GPa. A: Diffraction pattern with labelled lattice planes. B: Unrolled diffraction spectrum showing differential strain (as curvature of the diffraction rings) and texture (as intensity variations along the rings) of the experimental results (lower half) along with the best fit model (upper half) with the labelled lattice planes. On the y-axis are the diffraction rings integrated into 72 spectra, each spanning 5° and on the x-axis is the diffraction angle 2θ. C: Inverse pole figure (IPF) along the compression direction shows a 100 maximum. Mrd: multiples of random distribution.

using a polynomial function with usually ~12 iterations, peak shape, like full width at half maximum (FWHM) parameters (Caglioti et al., 1958), sample position, scale factors, cell length, crystal size, microstrain and Q-values. From the average of the measured lattice strains *Q(hkl)*, the deviatoric stress t was determined as (Singh et al., 1998):

$$t = 6 < Q(hkl) > G \tag{2.6}$$

where G is the high-pressure shear modulus of the analysed phase.

Figure 2.8 A shows diffraction pattern of a polycrystalline sample of ferropericlase at pressures of 58 GPa and temperatures of 1150 K with the lattice planes of (111), (200) and (220) at specific 2θ angles. The crystallographic preferred orientation or texture is visible as intensity variations along the diffraction rings. The differential lattice strains are visible as a curvature of the diffraction rings, shown in the unrolled diffraction image in Figure 2.8 B. To fit lattice strains,

the model of Singh et al., 1998 for nonhydrostatic pressure is used (named "radial diffraction in the DAC"):

$$d_m(hkl,\psi) = d_p(hkl)[1 + (1 - cos^2\psi)Q(hkl)] \quad (2.7)$$

With $Q(hkl)$ as reciprocal lattice point coordinates, ψ as angle between the diffraction plane normal and the maximum stress direction, $d_m(hkl,\psi)$ as measured d-spacing for the (hkl) line diffraction at the angle ψ and $d_p(hkl)$ as hydrostatic d-spacing of the (hkl) line, which was calculated from the hydrostatic lattice parameter. Texture was fitted with the E-WIMV model, which allows an incomplete and arbitrary pole figure coverage and is comparable to the WIMV model of Matthies and Vinel, 1982. Figure 2.8 C shows an inverse pole figure with a maximum at (100), indicating substantial texture.

2.6.2 EVPSC: elastic viscoplastic self-consistent modelling

The elastic viscoplastic self-consistent modelling was used to compare the experimental results to models and to extract slip system activities as well as texture evolution and lattice strains (Figure 2.9). The input parameters were single-crystal elastic moduli together with their pressure dependence as the critical resolved shear stresses (CRSS) (τ) and their pressure dependence ($d\tau/dP$), the hardening behaviour of the slip ($d2\tau/dP2$) and a stress exponent (n) (Table 2.1). The analysis steps described in Merkel et al., 2009 were followed. It can be chosen between different grain-interaction models like affine, secant or tangent.

Figure 2.9 shows the experimental derived lattice strains as a function of pressure and two different modelling results. To model these results the parameters in the code must be changed until the model fits the experimental data.

Table 2.1: Input parameters for EVPSC for different slip systems at 1400 K (Immoor et al., 2018).

slip system	τ_0 (GPa)	$d\tau/dP$	$d^2\tau/dP^2$ (GPa-1)	n
{110}< 1$\bar{1}$0>	1.0	0.01	-0.0001	5
{100}< 011>	2.2	0.04	-0.0004	5
{111}< 1$\bar{1}$0>	50	0	0	5

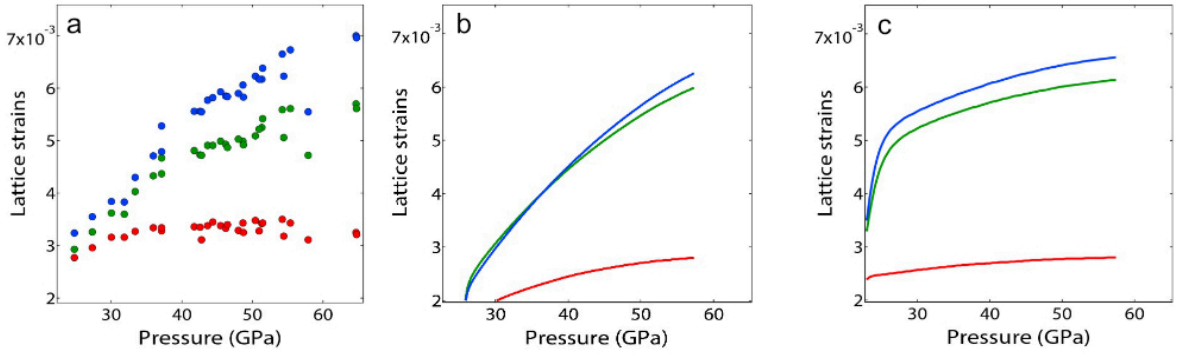

Figure 2.9: Lattice strains as a function of pressure (GPa) at 1400 K. a: experimental derived results. b: EVPSC modelling results using the secant model with 20% axial strain at the highest pressure. c: EVPSC modelling results using the secant model with 16% axial strain. Red: Q200, green: Q220, blue: Q111 (modified after Supplementary Data of Immoor et al., 2018).

2.6.3 Further programs used

For some data Fit2d was used slicing the diffraction images and to import the results into MAUD, where they were further analysed. The orientation distribution function (ODF) was exported to the software program BEARTEX (Wenk et al., 1998) to plot the IPF.

Chapter 2
Experimental Methods

Chapter 3
Synopsis

This chapter is a summary of the following chapters 5 – 7 in this thesis, which include the published and accepted papers.

Chapter 5 gives a brief outlook about the possibilities of the newly developed water-cooled vacuum chamber which is used to host the graphite-heated DAC for radial x-ray diffraction experiments under high pressure and high temperature. Four successful experiments with different sample material were carried out.

The following chapter 6 presents the results of successful experiments on ferropericlase. An attempt is made to constrain the source of the observed seismic anisotropy in Earth's lowermost mantle. One possibility is the change of texture in ferropericlase during a subduction process in a slab. It is discussed how the development of crystallographic preferred orientation of ferropericlase could contribute to the observed anisotropy in the lower mantle. During the experiment temperatures up to 1400 K and pressures up to 65 GPa were reached, and a change of dominant slip system with pressure is observed in the high-temperature experiments. The combination of our results with a geodynamic model shows strong shear wave anisotropy resulting from crystallographic preferred orientation of deformed ferropericlase.

The last part of this chapter discusses the deformation behaviour of calcium perovskite in the lower mantle. Under lower mantle conditions the phase is cubic, and our results show that that cubic calcium perovskite exhibits very low strength at high temperature. It is weaker than bridgmanite and ferropericlase. This behaviour might affect the behaviour of slab movement by separating the oceanic crust from the underlying mantle. The crust could accumulate in the uppermost mantle, or it could continue to sink down to the core-mantle boundary.

3.1 Summary of chapter 5: An improved setup for radial diffraction experiments at high pressures and high temperatures in a resistive graphite-heated diamond anvil cell

This paper introduces the new developed vacuum chamber used for graphite-heated radial x- ray diffraction experiments in a Mao-Bell diamond anvil cell at simultaneously high pressure and high temperature. For now, 1900 K is currently the highest temperature that is reachable with this method. As possible applications for this new approach, the results of four different materials are presented: ferropericlase, calcium perovskite, a mixture of ferropericlase and bridgmanite, and tantalum carbide. In general, it is important for many applications in geosciences, in material sciences and in industrial production how deformation processes of materials are influenced by pressure and temperature. The limiting factor in former experiments has been increasing temperature because of oxidation processes in the diamond anvil cell and problems with pressure control due to the thermal expansion of the pressure apparatus. Nevertheless, the diamond anvil cell is the most promising tool to create high pressures and together with resistance heating to generate high temperatures that are equally distributed in the sample chamber. To stop oxidation processes a vacuum chamber with a water-cooled system has been developed. The vacuum can be reduced to 5x 10^{-3} mbar. The piston part of the diamond anvil cell is indirectly cooled and reduces friction between the piston and cylinder part. Higher pressures can now be reached with this new setup at Extreme Conditions Beamline (ECB) P02.2 at PETRA III, DESY (Hamburg, Germany). A powder sample is loaded in a Mao-Bell type diamond anvil cell and diffraction images are collected with a Perkin Elmer detector in radial scattering geometry and further analysed with different kinds of data analysing software. A detailed description of the vacuum chamber, the preparation process of the diamond anvil cell, the setup at the beamline and the data processing can be found in chapter 2.

In Earth's lower mantle ferropericlase is from a rheological point of view, weaker than bridgmanite, and it has a strong elastic anisotropy in the lower mantle. Both properties suggest that ferropericlase may have a big influence on the anisotropy, and may able to explain shear wave splitting observed in the lower mantle (Marquardt et al., 2009). We studied the deformation behaviour of fine ground powder of $Mg_{0.8}Fe_{0.2}O$ loaded in the above-mentioned setup. Four different runs under different pressure and temperature conditions were performed and analysed. The observed texture evolution under increasing pressure and temperature in our experiments documented a change in slip system in ferropericlase at lower mantle conditions. This experiment and the results are described and analysed in detail in chapter 3.2 and chapter 7.

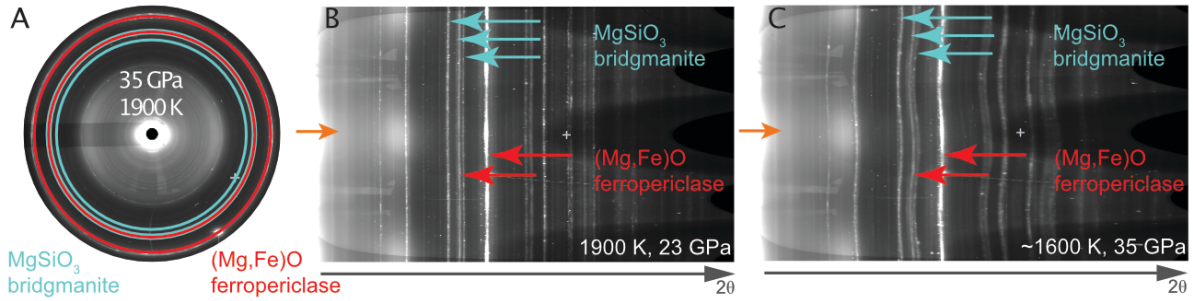

Figure 3.1: In-situ synthesis of bridgmanite (green) in a two-phase assemblage together with ferropericlase (red). In the unrolled x-ray diffraction image, the orange arrows indicate the compression direction. A: diffraction pattern at 30 GPa and 1900 K of ferropericlase and bridgmanite. B: unrolled diffraction image at 18 GPa and 1900 K of ferropericlase and bridgmanite. C: unrolled diffraction image at 30 GPa and 1600 K of ferropericlase and bridgmanite showing the curved rings after pressure increase. Modified after Immoor et al., 2020.

The second experiment focused on the in-situ synthesis and deformation of cubic calcium perovskite ($CaSiO_3$) at conditions of the lower mantle. In a pyrolytic mantle the cubic phase is the third most abundant mineral in the transition zone and the lower mantle and forms up to 25 vol.% in a subducted slab of converted basaltic crust (Frost, 2008). The influence on the rheology of the lithospheric slab is poorly understood and shear wave splitting at lower mantle conditions resulting from calcium perovskite has been proposed by the model of Kawai & Tsuchiya (2015). A strong texture development might also have an impact on seismic anisotropy in the shallow lower mantle and transition zone (Caracas et al., 2005; Jung and Oganov, 2005; Adams and Oganov, 2006). At lower mantle conditions $CaSiO_3$ forms a cubic structure, under ambient conditions the structure is unstable and therefore impossible to quench. Wollastonite was loaded as starting material and the cubic phase was synthesized and analysed *in-situ* under high-pressure and high-temperature conditions. Platinum powder was added for pressure determination. Several successful runs were performed up to 1150 K and pressures up to 45 GPa. The results are presented separately in chapter 3.3 and chapter 7.

The composition of the lower mantle is a multi-phase assemblage. Regarding the lower mantle, a two-phase assemblage of ferropericlase and bridgmanite is more realistic than considering only one phase. Both minerals have different plastic strengths and viscosities (Yamazaki and Karato, 2001b; Marquardt and Miyagi, 2015; Girard et al., 2016), i.e. a huge contrast in rheological strength. For this reason, the deformation behaviour of the single-phases is likely different from that of the two-phase assemblage (Karato, 1981; Handy, 1994; Takeda, 1998b; Merkel, 2002; Thielmann et al., 2020). Some multiphase deformation experiments have been done with $CaGeO_3$ (perovskite) and MgO aggregates, and neighborite ($NaMgF_3$) and halite (NaCl), as lower mantle analogues and with ferropericlase and bridgmanite, but only at limited pressure and temperature conditions of the lower mantle (Wang et al., 2013; Girard et al., 2016; Kaercher et al.,

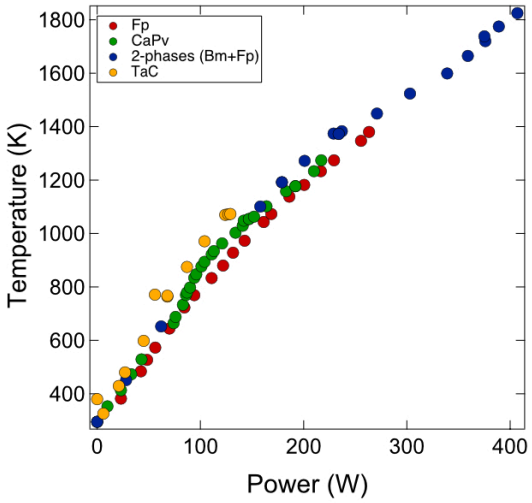

Figure 3.2: Temperature to power dependence in experiments on ferropericlase (red), calcium perovskite (green) bridgmanite and ferropericlase (blue) and tantalum carbide (yellow).

2016). The starting material in this study was a powder mixture of enstatite glass and ferropericlase. Bridgmanite was synthetized *in-situ* under high pressure and temperatures of 1900 K (Figure 3.1 A, B) showing the typical triplet of diffraction rings. Bridgmanite was deformed together with ferropericlase at pressures of ~35 GPa and temperatures of 1600 K, which can be seen as a nice curvature of the diffraction rings (Figure 3.1 C).

We also performed experiments on tantalum carbide $TaC_{0.99}$, an ultra-high temperature ceramic. As all carbides it is mostly used in industrial applications because the thermal and mechanical stability is enormous. Carbides have been well studied experimentally and computationally, except from experiments at simultaneous high pressure and high temperature under deviatoric stress (Speziale et al., 2019). Two successful diamond anvil cell experiments were performed with $TaC_{0.99}$ polycrystalline sample as starting material. A thin Au foil was added for pressure calculation (Fei et al., 2007a). The pressure-volume-temperature equation of state (EOS) was constrained under non-hydrostatic conditions by obtaining the unit-cell parameters from the diffraction data (Speziale et al., 2019). In the first run, the pressure in the sample chamber was increased to 2 GPa and heated to 673 K, then diffraction images were collected while the pressure was continuously increased from 2 – 33 GPa at a constant temperature of 673 K. The second run was carried out at an isotherm of 1073 K with a starting pressure of ~2 GPa and a final pressure of ~38 GPa. The results are used to estimate strength and identify the activity of slip systems in tantalum carbide.

As demonstrated in this thesis, a new combination of a water-cooled vacuum chamber with a radial diffraction setup used with graphite-heated Mao-Bell diamond anvil cell and synchrotron radiation has been successfully tested under simultaneously high pressure and high temperature.

Chapter 3
Synopsis

The biggest challenge to overcome was increasing pressure at high temperatures in the Mao-Bell diamond anvil cell. The great advantage of the vacuum chamber and the indirectly water-cooled piston part enabled successful experiments to increase pressure up to 1400 K. Above these temperatures up to 1900 K reaching higher pressures was impossible. At temperatures higher 1400 K the diamond anvil cell jammed a couples of times, which led to pressure jumps and often to the end of the experiment. The gaskets were not able to buffer these fast increases and broke and therefore the diamonds too. The reason for this could be thermal expansion of the piston and cylinder part of the cell during the high temperatures. Although the piston was already cooled, this does not seem to be enough. The friction was too strong so that the two parts got stuck and then suddenly came loose again due to a further increase in pressure. This needs more development. Another challenge was the thermocouples measurement, which was good as long as the thermocouple under the graphite heater was close to the tip of the diamond. Sometimes it happened, that the distance was too far and the temperature difference between the two thermocouples was large (up to 400 K). The higher temperature reading was the information of the thermocouple between the graphite sheets and the lower temperature belonged to the one next to the tip of the diamond. Nevertheless, a good temperature to power dependence was reproducible in all experiments (Figure 3.2).

3.2 Summary of chapter 6: Evidence for {100}<011> slip in ferropericlase in Earth's lower mantle from high-pressure/high-temperature experiments

Seismic anisotropy is widely believed to be produced by the crystallographic preferred orientation of elastically anisotropic minerals (Merkel et al., 2007; Miyagi et al., 2010; Nowacki et al., 2011; Romanowicz and Wenk, 2017). Ferropericlase as a major mantle phase has different possible slip systems and their activity might change during pressure and temperature increase. To figure out which slip system is active and how it will contribute to seismic anisotropy observations in the lowermost part of the mantle and the D"-region is the main subject of this manuscript.

Post-perovskite, the most abundant mineral in the colder parts of the lowermost mantle, is the main candidate explaining seismic anisotropy (Miyagi et al., 2010; Walker et al., 2011; Wenk et al., 2011; Nowacki et al., 2013). It was suggested that shear wave splitting resulted from the deformed post-perovskite and the resulting crystallographic preferred orientations. The studies included 2D and 3D flow field modelling results and focused on regions around the core-mantle-boundary. The results of the dominant slip-systems of post-perovskite, however, are still under discussion. In a pyrolytic lower mantle ferropericlase is the second most abundant mineral. There have not yet been any deformation experiments on this phase under the pressure and temperature conditions of the lower mantle. Ferropericlase is an excellent alternative candidate for explaining shear wave splitting, as the elastic anisotropy is significantly larger as compared to post-perovskite or bridgmanite (Marquardt et al., 2009). It is a rheological weak mineral (Yamazaki et al., 2009; Marquardt and Miyagi, 2015; Girard et al., 2016) and the elastic anisotropy increases with depth (Lin et al., 2013). The slip system activities of ferropericlase are sensitive to pressure, temperature and possibly strain rate. Possible changes of slip systems have to be considered when modelling the expected crystallographic preferred orientation through deformation processes (Amodeo et al., 2012; Cordier et al., 2012). It is still unclear which slip systems in ferropericlase are operating in the lower mantle regime. Modelling results for dislocation creep at mantle pressures suggested the slip systems {100}<011> and {110}<1$\bar{1}$0>, but so far, this prediction has not be proven experimentally (Merkel, 2002; Lin et al., 2009, 2017; Cordier et al., 2012; Girard et al., 2012; Marquardt and Miyagi, 2015). An experimental study with the Paterson deformation apparatus at high temperature but low pressures presented {100}<011> as dominant slip system (Stretton et al., 2001). However, none of the derived experimental results have been obtained at lower mantle pressure and high temperatures.

The results of this resistive heated diamond anvil cell study are obtained at simultaneously high pressure and high temperature. A polycrystalline mixture of $(Mg_{0.8}Fe_{0.2})O$ was loaded into a Mao-Bell type diamond anvil cell and precompressed, using a diamond culet size of 200 µm or

300 µm. The experimental setup described in chapter 2.2 and chapter 2.3 was used to collect diffraction images from the centre of the sample chamber each for 30 seconds and every 1 – 5 GPa to monitor the texture and strain evolution of the sample. The sample was heated slowly over several hours to a target temperature to give the system the chance to equilibrate. Afterwards, pressure was increased remotely with a gas membrane device and was calculated with parameters published in (Stixrude and Lithgow-Bertelloni, 2011) from the unit cell volume of platinum. Three different runs at 800 K, 1150 K and 1400 K were carried out. The results are compiled in Table 2.1 together with the 300 K results of Marquardt and Miyagi (2015).

The raw data were analysed using the program Material Analysing Using Diffraction (MAUD) following the instructions described in more detail in chapter 2.6.1 (Lutterotti et al., 1997). Modelling the experimental derived results , in particular the pressure evolution of texture and lattice strains was done after the method of Merkel et al. (2009) with the Elasto-Plastic Self-Consistent code (Wang et al., 2010; Lin et al., 2017). The experimental derived lattice strains (Figure 2.9 a) were modelled with the EVPSC code (Figure 2.9 c) using the secant model with 16 % axial strain. Pressure and strain increase simultaneous during the experiments and leaded together to hardening of the sample, whereby it is impossible to separate their relative effects. Achieving different strains for the same pressure is not possible in radial XRD diamond anvil cell experiments. The solution so far is to use the same formalism and to use the same parameters for strain hardening and pressure strengthening, because they have the same effect in the modelling results. This combination of both effects to one are mentioned as pressure strengthening parameters. For calculating of the slip systems, a stress component of $n=5$ was used for all possible three slip systems. A summary of input parameters is shown in Table 2.1. The slip system {111} $<1\bar{1}0>$ was suppressed by setting the initial values of the CRSS to 50.

Figure 3.3 represents the experimental inverse pole figures (IPF) results of ferropericlase with a strong temperature and pressure dependence in four different temperature runs. A different deformation behaviour between the low- and high-temperature runs operate. The IPF of the 300 K, 800 K and 1150 K run at lower temperatures and lower pressures show a strong 100 maximum which increases with pressure. The {110} $<1\bar{1}0>$ slip system is active during these temperature and pressure conditions. In addition, at high temperature and high pressure a second maximum at 110 appeared as a shoulder in the 800 K, 1150 K and 1400 K run. This is a strong sign for increased activity of {100} <011> slip system. From the observed texture evolution, it is possible to conclude that there is a change in slip system from {110} $<1\bar{1}0>$ to a system where both slip systems, {110} $<1\bar{1}0>$ and {100} <011>, are equal.

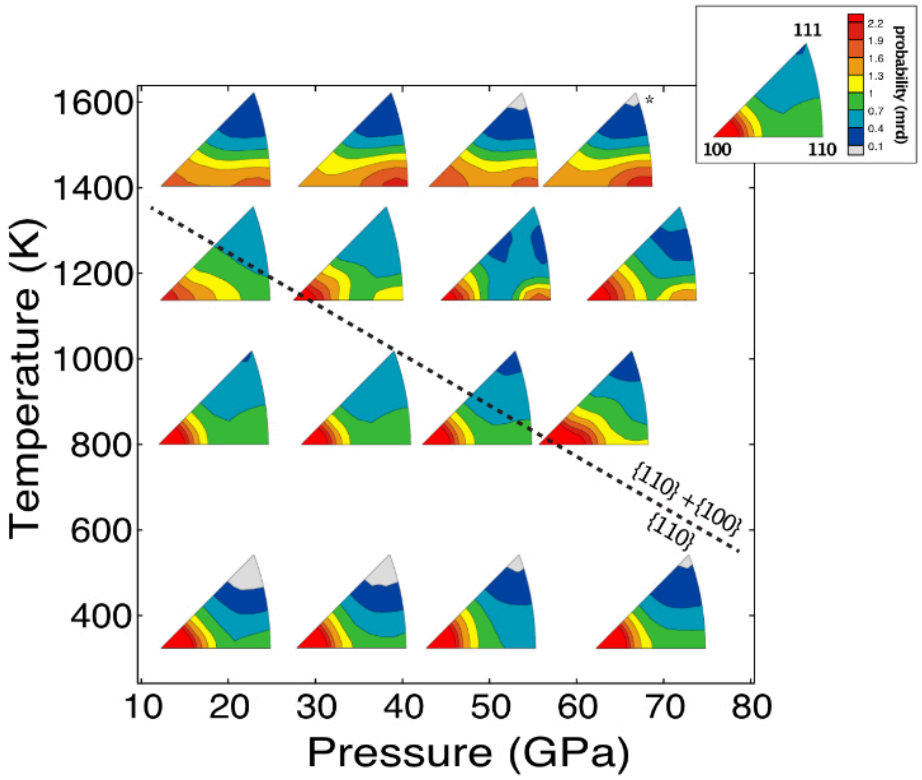

Figure 3.3: Pressure evolution of ferropericlase with the 300 K results of (Marquardt and Miyagi, 2015). The lower right corners of the IPFs are placed at the corresponding P/T-conditions. The dashed line is intended for illustration only and highlights the transition from dominant slip on {110} to a regime where slip on {110} and {100} are equally important as judged from the IPF appearances. The inset shows the axes and color scale of the IPF.

We were able to simulate our experimental results with extraction of the slip systems using the EVPSC modelling (Figure 3.4). Figure 3.4 A shows the activity of the slip system {110} and {100} at 300 K and 1400 K of a given pressure. At 300 K {110} slip plane is fully active and there is no activity of the slip plane {100}. In contrast, at 1400 K a change in slip system could be modelled. At 1400 K {110} slip is less active than at 300 K and {100} slip becomes more active with rising pressure and temperature. This activity of {100} <011> slip system leads to a shift of intensity maximum to 110 in the IPF (Figure 3.4). During the modelling, the focus was on order and magnitude of the Q- factors to get the right CRSS, while also matching the observed texture (Figure 2.9).

If we transfer our results to the lowermost mantle, this means that the dominant, active slip system of ferropericlase changes gradually, and a different texture develops with increasing pressure and temperature. Together with large elastic anisotropy of ferropericlase in the lower mantle (Marquardt et al., 2009), the change of slip system activities could help explaining the observed seismic anisotropy in the lowermost mantle. Strong deformation and therefore pronounced seismic anisotropy is observed at the edges of the Large Low Shear Velocity Provinces (LLSVP) (Cottaar and Romanowicz, 2013; Lynner and Long, 2014; Garnero et al., 2016).

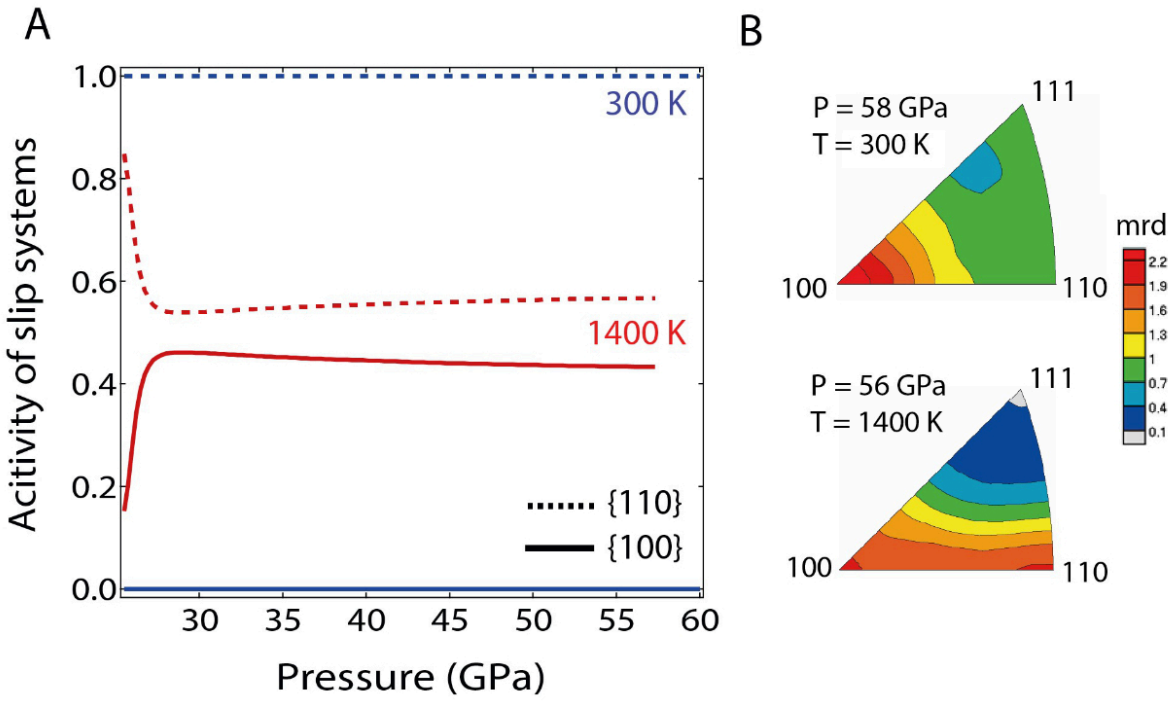

Figure 3.4: EVPSC modelling results of experimental generated data. A: Activity of slip systems vs. Pressure (GPa). Showing the modelling results of the experiments at 1400 K (red) and 300 K (blue) with the pressure temperature dependence of slip system activities. B: Modelled inverse pole figures at 300 K and 58 GPa (top) and 1400 K and 56 GPa (bottom). Mrd: multiples of random distribution.

We used a 2D geodynamic large-scale model to show seismic anisotropy development in the mantle and the D"-layer (McNamara and Zhong, 2005; Merkel et al., 2007; Miyagi et al., 2010). We made different assumptions in this calculation, as the subducting slab has a random orientation distribution, dislocations movement can only absorb 10 % of the total strain accumulation by the strain tracer, which also documents temperature, the ratio of slip systems strengths (CRSS) of {110} <1$\bar{1}$0> and {100} <011> is 10:1, the slip {111} is blocked and no hardening is implied. The domination of the {100} <011> slip system lead to 99 % strain accommodation on this slip. The calculation of elastic properties was done over orientation distribution of the subducting material with the geometric mean (Matthies and Humbert, 1993) and we used the average of elastic coefficients of MgO from single-crystals (Karki et al., 1999). The model shows seismic shear wave splitting from ferropericlase at three positions along a slab in the lowermost mantle: (1) the downwelling, (2) reaching the core mantle boundary at the D"-layer where lateral deformation was assumed the whole way along the boundary before, (3) the deformed part starts upwelling at the margin of a Large Low Shear Velocity Province (LLSVP).

Seismic waves traveling along the slab can travel fast as horizontal polarized shear waves (VSH) or slow as vertical polarized shear waves (VSV). The dominant slip in ferropericlase {100} produces a VSH > VSV through the whole streamline, with a maximum in upwelling areas. The intensity of splitting depends strongly on the direction of the ray path. This effect can be

reinforced by the contribution of post-perovskite, because it may generate a VSH > VSV as well (Miyagi et al., 2010; Wu et al., 2017).

The deformed material is always a multi-phase-assemblage and to get a final solution for the source of observed seismic anisotropy more experimental studies are needed, including at least two-phase deformation results. Nevertheless, these deformation results of ferropericlase show strong evidence for a change in slip system at conditions at the mid-lower mantle and shows that ferropericlase can be a major contributor to seismic anisotropy with its {100}<110> slip system.

3.3 Summary of chapter 7: Weak Cubic $CaSiO_3$ Perovskite in Earth's Mantle

Calcium perovskite $CaSiO_3$ is the third major lower mantle mineral after bridgmanite and ferropericlase (Figure 1.1). The phase forms up to 25 vol.% in a subducted basaltic crust and up to 10 vol.% in a pyrolytic mantle, forming from majoritic garnet at depths of ~550 km (Irifune and Klemme, 2007; Hirose et al., 2017). The perovskite structure is at room temperature tetragonal and at high temperatures and high pressures cubic. In the lower mantle, calcium perovskite is expected to have a cubic structure (Komabayashi et al., 2007; Sun et al., 2016; Gréaux et al., 2019; Thomson et al., 2019) which is not quenchable. Results from tetragonal calcium perovskite are available at room temperature and high pressure and suggest that the plastic strength is high (Shieh et al., 2004; Miyagi et al., 2009). In our study, we measured the high-temperature plastic strength of cubic calcium perovskite. We found that cubic calcium perovskite is a weak phase showing a low viscosity and low plastic strength as compared to the other mantle minerals bridgmanite and ferropericlase. This could impact the dynamic behaviour of subducting slabs, in particular the oceanic crust, in the mantle, where it might either accumulate between the upper and lower mantle, or it will make its way to the core-mantle boundary.

We performed high-pressure and high-temperature experiments on calcium perovskite using the technique explained in chapter 2, 3.1 and 5 (Immoor et al., 2020). For the measurements with the RH-rXRD-DAC we used a fine grounded mixture of wollastonite and a small amount of platinum for pressure determination as starting material. We were able to synthesize the cubic variant at 1150 K and pressures of the mantle. During pressure increase and deformation of the cubic phase, x-ray diffraction images were taken in radial diffraction geometry. The generated diffraction images were analysed with MAUD (see chapter 2.6.1) for fitting lattice strain *Q(hkl)*. We observed a texture grow in the IPFs and together with modelled IPFs using the Visco-Plastic Self-Consistent (VPSC) code (Lebensohn and Tomé, 1993) we were able to prove that plastic deformation occurred in the sample. The approximate plastic strength of the sample is derived from the measured lattice strains (Merkel, 2002). In Figure 3.5 a the strength of tetragonal calcium perovskite, ferropericlase and bridgmanite at ambient conditions (Merkel et al., 2003; Miyagi et al., 2009; Marquardt and Miyagi, 2015) is compared. Figure 3.5 b shows high-temperature strength results of our accomplished experiments of cubic calcium perovskite in comparison with ferropericlase and bridgmanite at 1150 K (Girard et al., 2016; Immoor et al., 2018; Couper et al., 2020). The analysed phase is clearly the weakest mineral at high temperatures because of the really low high-temperature plastic strength, which is even lower than a reported strength of

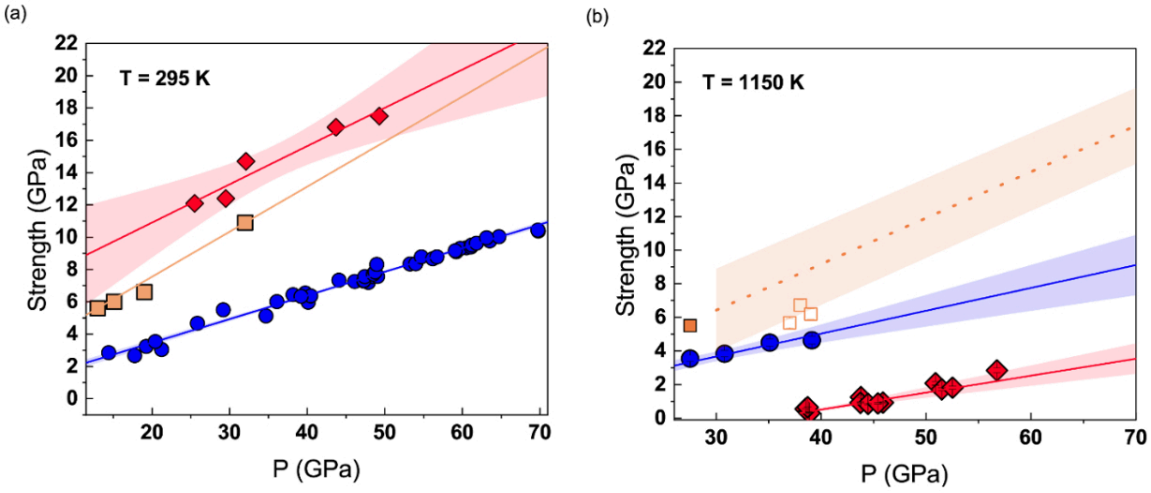

Figure 3.5: Strength of major lower mantle phases at high pressures. (a) strength values measured at room temperature by previous works. Red: tetragonal $CaSiO_3$ perovskite (Miyagi et al., 2009); orange: $Mg_{0.9}Fe_{0.1}SiO_3$ bridgmanite (Merkel et al., 2003); blue: $(Mg_{0.8}Fe_{0.2})O$ ferropericlase (Marquardt and Miyagi, 2015). (b) Here-derived high-temperature strength of cubic $CaSiO_3$ perovskite at lower mantle pressures (red solid diamonds) compared to the strength of $(Mg_{0.8}Fe_{0.2})O$ measured at 1150 K (blue solid circles) (Immoor et al., 2018) and the stress measured on bridgmanite deformed as part of a multi-phase assemblage at 1000 K at comparably low strains, likely representing a lower bound to the high-temperature strength of bridgmanite (Couper et al., 2020) (open squares). The solid orange square denotes the strength of bridgmanite at 2750 K, taken from Girard et al., 2016 (their run "gamma 25"). Best-fit lines are shown along with their 95 % confidence range. Given the limited amount of data on the high-temperature strength reported for bridgmanite, the strength of bridgmanite at 1150 K was derived from the data measured for bridgmanite at 295 K (Merkel et al., 2003) by applying two different temperature corrections represented by the shaded region (see Methods). Even though we acknowledge that this procedure is uncertain, the overlap of our derived range with the data collected on two-phase samples (squares) suggest that it provides a reasonable estimate.

bridgmanite at 2750 K and 27.5 GPa (Girard et al., 2016). Furthermore, the strong difference in strength between the tetragonal and the cubic perovskite phase is remarkable, even if it was expected to decrease with increasing temperature. With the already existing and our derived strength results, we have estimated the viscosity contrast between the individual phases with the equation (1.2) together with the identity

$$\eta = \frac{\sigma}{2\dot{\varepsilon}} \tag{3.1}$$

with η as viscosity, σ as stress and $\dot{\varepsilon}$ as strain. For a better comparison, we used the same stress component and assumed, that the strain rates in all experiments are the same. We calculated the viscosity of a load bearing framework (LBF) scenario where the initial deformation of the hard mineral phase takes place with an equal strain rate in the compared minerals. Progressed deformation was calculated assuming an interconnected weak layer (IWL) regime of the weak mineral phase with uniform stress. In both scenarios calcium perovskite is the weakest phase compared to ferropericlase and bridgmanite, often by several orders of magnitude, especially with a regime in which the IWL dominates, which corresponds to large strain regions in the mantle. In a

subducting slab, the hard garnet phase transforms into the weak cubic calcium perovskite. In the beginning of this process, a LBF regime with a constant strain rate exist. The formation of cubic calcium perovskite will lead to a weakening of the subducted crust and partitioning of strain in the weak perovskite will happen. This could lead to a formation of an IWL network during the deformation process. As a result, the viscosity contrast of the mineral phases might increase which lead to an even stronger partitioning of strain and the weakening would be reinforced. The strength of this development depends on the viscosity contrast between the weak phase and the stronger ones and the volume fractions. Our results show a high contrast between the three phases bridgmanite, ferropericlase and calcium perovskite in the slab and a high-volume fraction of calcium perovskite exists.

In concrete terms it means that at a depth of 550 km strain starts to partition in cubic calcium perovskite weakening the crust. As a result the subducted crust will be squeezed between hard mantle rocks and can be easily separated by shear forces (Van Keken et al., 1996). At a depth of 660 – 720 km, the density of the surrounding mantle will be higher than the subducting basaltic crust. This ratio changes at depth deeper than 720 km after the complete transformation of garnet into cubic calcium perovskite (Hirose et al., 1999, 2005). Considering that the buoyancy contrast depends on depth, two scenarios are possible and could explain different seismic observations. One is the accumulation of crust around 660 km depths (Ballmer et al., 2015). The other the sinking of the slab to the core-mantle boundary as an “upside-down plume” and accumulation in the LLSVPs under Africa and the Pacific ocean (Garnero et al., 2016; Thomson et al., 2019; Jones et al., 2020).

3.4 Conclusions

This thesis reports the development of the new water-cooled vacuum chamber specially designed for radial diffraction experiments at simultaneously high pressure and high temperature. With this approach, we were able to solve problems related to high temperatures. We were able to both reduce the oxidation processes of the diamond anvil cells and ensure the uniform distribution of heat in the sample with a graphite heater.

We investigated the deformation behaviour of two important lower mantle minerals ferropericlase and cubic calcium perovskite. The experimental results together with EVPSC modelling help to understand the fate of subduction slabs and might explain seismic observables in different regions of the mantle.

Ferropericlase deformation results show that a change in the slip system occurs with increasing temperature and pressure, which could explain the seismic shear wave splitting in the lower mantle. After the successful synthesis of cubic calcium perovskite and its deformation, the modelling data indicate that the phase has a low viscosity and that it is the weakest minerals phase at high temperature and high pressure compared to the other mantle minerals because of its low plastic strength.

In addition, bridgmanite was synthesized and deformed together with ferropericlase. Further studies need to be performed on this two-phase mixture to see how the strength of each phase develops and whether these results have any implications for our findings and conclusions to date.

It should be noted that tantalum carbide ($TaC_{0.99}$) as an industrially used material was not part of this thesis. $TaC_{0.99}$ was investigated in the first experiments to show that the new experimental setup covers a wide range of application areas and cannot only be used for geological materials and questions.

References

Adams, D. J. & Oganov, A. R. (2006). Ab initio molecular dynamics study of CaSi O3 perovskite at P-T conditions of Earth's lower mantle. *Physical Review B - Condensed Matter and Materials Physics* **73**, 1–8.

Amodeo, J., Carrez, P. & Cordier, P. (2012). Modelling the effect of pressure on the critical shear stress of MgO single crystals. *Philosophical Magazine*. Taylor & Francis Group **92**, 1523–1541.

Amodeo, J., Dancette, S. & Delannay, L. (2016). Atomistically-informed crystal plasticity in MgO polycrystals under pressure. *International Journal of Plasticity*. Elsevier Ltd **82**, 177–191.

Ballmer, M. D., Schmerr, N. C., Nakagawa, T. & Ritsema, J. (2015). Earth Sc Iences: Compositional mantle layering revealed by slab stagnation at ~1000-km depth. *Science Advances* **1**, 1–9.

Bassett, W. A. & Takahashi, T. (1965). Silver iodide polymorphs. *American Mineralogist* **50**, 1576–1594.

Bassett, W. A., Takahashi, T. & Stook, P. W. (1967). X-ray diffraction and optical observations on crystalline solids up to 300 kbar. *Review of Scientific Instruments* **38**.

Bragg, W. L. & Bragg, W. H. (1914). The analysis of crystals by the X-ray spectrometer. *Proceedings of the Royal Society of London. Series A, Containing Papers of a Mathematical and Physical Character* **89**, 468–489.

Buras, B., Olsen, J. S., Gerward, L., Will, G. & Hinze, E. (1977). X-ray energy-dispersive diffractometry using synchrotron radiation. *Journal of Applied Crystallography* **10**, 431–438.

Caglioti, G., Paoletti, A. & Ricci, F. P. (1958). Choice of collimators for a crystal spectrometer for neutron diffraction. *Nuclear Instruments* **3**, 223–228.

Caracas, R., Wentzcovitch, R., Price, G. D. & Brodholt, J. (2005). CaSiO3 perovskite at lower mantle pressures. *Geophysical Research Letters* **32**, 1–5.

Carrez, P., Ferré, D. & Cordier, P. (2009). Peierls-Nabarro modelling of dislocations in MgO from ambient pressure to 100 GPa. *Modelling and Simulation in Materials Science and Engineering* **17**.

Clauser, C. (2009). Heat transport processes in the earth's crust. *Surveys in Geophysics* **30**, 163–191.

Conrad, C. P., Behn, M. D. & Silver, P. G. (2007). Global mantle flow and the development of seismic anisotropy: Differences between the oceanic and continental upper mantle. *Journal of Geophysical Research: Solid Earth* **112**, 1–17.

Copley, S. M. & Pask, J. A. (1965). Plastic Deformation of MgO Single Crystals up to 1600°C. *Journal of the American Ceramic Society* **48**, 139–146.

Cordier, P., Amodeo, J. & Carrez, P. (2012). Modelling the rheology of MgO under Earth's mantle pressure, temperature and strain rates. *Nature*. Nature Publishing Group **481**, 177–180.

Cottaar, S., Li, M., McNamara, A. K., Romanowicz, B. & Wenk, H. R. (2014). Synthetic seismic anisotropy models within a slab impinging on the core-mantle boundary. *Geophysical Journal International* **199**.

Cottaar, S. & Romanowicz, B. (2013). Observations of changing anisotropy across the southern margin of the African LLSVP. *Geophysical Journal International* **195**, 1184–1195.

Couper, S., Speziale, S., Marquardt, H., Liermann, H. P. & Miyagi, L. (2020). Does Heterogeneous Strain Act as a Control on Seismic Anisotropy in Earth's Lower Mantle? *Frontiers in Earth Science* **8**.

Creasy, N., Long, M. D. & Ford, H. A. (2017). Deformation in the lowermost mantle beneath Australia from observations and models of seismic anisotropy. *Journal of Geophysical Research: Solid Earth* **122**, 5243–5267.

Davies, G. F. (1999). *Dynamic Earth*. Cambridge University Press.

de Wit, R. W. L. & Trampert, J. (2015). Robust constraints on average radial lower mantle anisotropy and consequences for composition and texture. *Earth and Planetary Science Letters* **429**.

Dobson, D. P., Miyajima, N., Nestola, F., Alvaro, M., Casati, N., Liebske, C., Wood, I. G. & Walker, A. M. (2013). Strong inheritance of texture between perovskite and post-perovskite in the D″ layer. *Nature Geoscience* **6**.

Dziewonski, A. M. & Anderson, D. L. (1981). Preliminary reference Earth model. *Physics of the Earth and Planetary Interiors* **25**.

Evans, T. (1976). Diamonds. *Contemporary Physics*. Taylor & Francis **17**, 45–70.

Fei, Y., Ricolleau, A., Frank, M., Mibe, K., Shen, G. & Prakapenka, V. (2007a). High-Pressure Geoscience Special Feature: Toward an internally consistent pressure scale. *Proceedings of the National Academy of Sciences*.

Fei, Y., Ricolleau, A., Frank, M., Mibe, K., Shen, G. & Prakapenka, V. (2007b). Toward an internally consistent pressure scale. *Proceedings of the National Academy of Sciences* **104**, 9182–9186.

Ferré, D., Carrez, P. & Cordier, P. (2009a). Peierls dislocation modelling in perovskite (CaTiO3): Comparison with tausonite (SrTiO3) and MgSiO3 perovskite. *Physics and Chemistry of Minerals* **36**.

Ferré, D., Cordier, P. & Carrez, P. (2009b). Dislocation modeling in calcium silicate perovskite based on the Peierls-Nabarro model. *American Mineralogist* **94**.

Frost, D. (2008). The Upper Mantle and Transition Zone. *Elements* **4**, 171–176.

Frost, H. J. & Ashby, M. F. (1982). Deformation-mechanism maps: The plasticity and creep of metals and ceramics. *Oxford, Pergamon Press* 175.

Fukao, Y. & Obayashi, M. (2013). Subducted slabs stagnant above, penetrating through, and trapped below the 660 km discontinuity. *Journal of Geophysical Research: Solid Earth* **118**, 5920–5938.

Funamori, N. & Sato, T. (2008). A cubic boron nitride gasket for diamond-anvil experiments. *Review of Scientific Instruments* **79**, 053903.

Garnero, E. J. (2004). Variable Azimuthal Anisotropy in Earth's Lowermost Mantle. *Science* **306**, 259–261.

Garnero, E. J., McNamara, A. K. & Shim, S.-H. (2016). Continent-sized anomalous zones with low seismic velocity at the base of Earth's mantle. *Nature Geoscience*. Nature Publishing Group **9**, 481–489.

Girard, J., Amulule, G., Farla, R., Mohiuddin, A. & Karato, S. (2016). Shear deformation of bridgmanite and magnesiowüstite aggregates at lower mantle conditions. *Science* **351**, 144–147.

Girard, J., Chen, J. & Raterron, P. (2012). Deformation of periclase single crystals at high pressure and temperature: Quantification of the effect of pressure on slip-system activities. *Journal of Applied Physics*.

Goryaeva, A. M., Carrez, P. & Cordier, P. (2015). Modeling defects and plasticity in MgSiO3 post-perovskite: Part 2—screw and edge [100] dislocations. *Physics and Chemistry of Minerals* **42**.

Gréaux, S., Irifune, T., Higo, Y., Tange, Y., Arimoto, T., Liu, Z. & Yamada, A. (2019). Sound velocity of CaSiO 3 perovskite suggests the presence of basaltic crust in the Earth's lower mantle. *Nature* **565**, 218–221.

Hammersley, A. P., Svensson, S. O., Hanfland, M., Fitch, A. N. & Häusermann, D. (1996). Two-dimensional detector software: From real detector to idealised image or two-theta scan. *High Pressure Research* **14**.

Handy, M. R. (1994). Flow laws for rocks containing two non-linear viscous phases: A phenomenological approach. *Journal of Structural Geology* **16**, 287–301.

Hazen, R. M. & Finger, L. W. (1981). High-temperature diamond-anvil pressure cell for single-crystal studies. *Review of Scientific Instruments* **52**, 75–79.

Hirose, K., Fei, Y., Ma, Y. & Mao, H. K. (1999). The fate of subducted basaltic crust in the Earth's lower mantle. *Nature* **397**.

Hirose, K., Sinmyo, R. & Hernlund, J. (2017). Perovskite in Earth's deep interior. *Science*.

Hirose, K., Takafuji, N., Sata, N. & Ohishi, Y. (2005). Phase transition and density of subducted MORB crust in the lower mantle. *Earth and Planetary Science Letters* **237**.

Hirth, J. P. & Lothe, J. (1968). *Theory of dislocations*. New York: McGraw-Hill.

Hofmann, A. (1997). Mantle geochemistry: the message from oceanic volcanism. *Nature* **385**, 219–229.

Huber, G., Syassen, K. & Holzapfel, W. B. (1977). Pressure dependence of 4f levels in europium pentaphosphate up to 400 kbar. *Physical Review B* **15**.

Hunt, S. A. & Dobson, D. P. (2017). Note: Modified anvil design for improved reliability in DT-Cup experiments. *Review of Scientific Instruments* **88**, 126106.

Hunt, S. A., Whitaker, M. L., Bailey, E., Mariani, E., Stan, C. V. & Dobson, D. P. (2019). An Experimental Investigation of the Relative Strength of the Silica Polymorphs Quartz, Coesite, and Stishovite. *Geochemistry, Geophysics, Geosystems* **20**.

Immoor, J., Marquardt, H., Miyagi, L., Lin, F., Speziale, S., Merkel, S., Buchen, J., Kurnosov, A. & Liermann, H. P. (2018). Evidence for {100}<011> slip in ferropericlase in Earth's lower mantle from high-pressure/high-temperature experiments. *Earth and Planetary Science Letters*. Elsevier B.V. **489**, 251–257.

Immoor, J., Marquardt, H., Miyagi, L., Speziale, S., Merkel, S., Schwark, I., Ehnes, A. & Liermann, H. (2020). An improved setup for radial diffraction experiments at high pressures and high temperatures in a resistive graphite-heated diamond anvil cell An improved setup for radial diffraction experiments at high pressures and high temperatures in a resistive grap. *Review of Scientific Instruments*. AIP Publishing, LLC **045121**, 045121-1-045121–7.

Immoor, J., Miyagi, L., Liermann, H.-P., Speziale, S., Schulze, K., Buchen, J., Kurnosov, A. & Marquardt, H. ((n.d.)). Weak Cubic CaSiO3 Perovskite in Earth's Mantle. *Nature*.

Irifune, T. & Klemme, S. (2007). Mineralogy of the Earth - Phase Transitions and Mineralogy of the Lower Mantle. *Treatise on Geophysics*.

Irifune, T. & Tsuchiya, T. (2015). Phase Transitions and Mineralogy of the Lower Mantle. *Treatise on Geophysics: Second Edition*.

Jayaraman, A. (1983). Diamond anvil cell and high-pressure physical investigation. *Reviews of Modern Physics* **55**, 65–108.

Jones, T. D., Maguire, R. R., van Keken, P. E., Ritsema, J. & Koelemeijer, P. (2020). Subducted oceanic crust as the origin of seismically slow lower-mantle structures. *Progress in Earth and Planetary Science* **7**.

Jung, D. Y. & Oganov, A. R. (2005). Ab initio study of the high-pressure behavior of CaSiO3 perovskite. *Physics and Chemistry of Minerals* **32**, 146–153.

Kaercher, P., Miyagi, L., Kanitpanyacharoen, W., Zepeda-Alarcon, E., Wang, Y., De Carlo, F. & Wenk, H.-R. (2016). Two-phase deformation of lower mantle mineral analogs. *Earth and Planetary Science Letters*. Elsevier B.V. **456**, 134–145.

Karato & Li (1992). Diffusion creep in perovskite: implications for the rheology of the lower mantle. *Science* **255**, 1238–1240.

Karato, S. (1981). Rheology of the lower mantle. *Physics of the Earth and Planetary Interiors* **24**, 1–14.

Karato, S. (1988). The role of recrystallization in the preferred orientation of olivine. *Physics of the Earth and Planetary Interiors* **51**, 107–122.

Karato, S. (1998). Some remarks on the origin of seismic anisotropy in the D" layer. *Earth Planets and Space* 1019–1028.

Karato, S. & Wu, P. (1993). Rheology of the Upper Mantle: A Synthesis. *Science* **260**, 771–778.

Karato, S., Zhang, S. & Wenk, H.-R. (1995). Superplasticity in Earth's Lower Mantle: Evidence from Seismic Anisotropy and Rock Physics. *Science* **270**, 458–461.

Karki, B. B., Wentzcovitch, R. M., De Gironcoli, S. & Baroni, S. (1999). First-principles determination of elastic anisotropy and wave velocities of MgO at lower mantle conditions. *Science* **286**.

Kavner, A., Sinogeikin, S. V., Jeanloz, R. & Bass, J. D. (2000). Equation of state and strength of natural majorite. *Journal of Geophysical Research: Solid Earth* **105**.

Kawai, K. & Tsuchiya, T. (2015). Small shear modulus of cubic CaSiO3 perovskite. *Geophysical Research Letters* **42**, 2718–2726.

Kawazoe, T., Nishiyama, N., Nishihara, Y., Irifune, T., Suetsugu, D., Bina, C., Inoue, T., Wiens, D. & Jellinek, M. (2010). Deformation experiment at P-T conditions of the mantle transition zone using D-DIA apparatus. *Physics of the Earth and Planetary Interiors* **183**, 190–195.

Kawazoe, T., Ohuchi, T., Nishihara, Y., Nishiyama, N., Fujino, K. & Irifune, T. (2013). Seismic anisotropy in the mantle transition zone induced by shear deformation of wadsleyite. *Physics of the Earth and Planetary Interiors* **216**, 91–98.

Kendall, J.-M. & Silver, P. G. (1996). Constraints from seismic anisotropy on the nature of the lowermost mantle. *Nature*, 409–412.

Kohlstedt, D. L. (2007). *Properties of Rocks and Minerals - Constitutive Equations, Rheological Behavior, and Viscosity of Rocks*. *Treatise on Geophysics*. Elsevier B.V.

Komabayashi, T., Hirose, K., Sata, N., Ohishi, Y. & Dubrovinsky, L. S. (2007). Phase transition in CaSiO3 perovskite. *Earth and Planetary Science Letters* **260**, 564–569.

Kondo, T., Ohtani, E., Hirao, N., Yagi, T. & Kikegawa, T. (2004). Phase transitions of (Mg,Fe)O at megabar pressures. *Physics of the Earth and Planetary Interiors* **143**, 201–213.

Kumar, S., Ravindranathan, P., Dewan, H. S. & Roy, R. (1996). Survival of diamond at 2200°C in hydrogen. *Diamond and Related Materials* **5**.

Kunz, M., Caldwell, W. a, Miyagi, L. & Wenk, H.-R. (2007). In situ laser heating and radial synchrotron x-ray diffraction in a diamond anvil cell. *The Review of scientific instruments* **78**, 063907.

Kurashina, T., Hirose, K., Ono, S., Sata, N. & Ohishi, Y. (2004). Phase transition in Al-bearing CaSiO3 perovskite: Implications for seismic discontinuities in the lower mantle. *Physics of the Earth and Planetary Interiors* **145**.

Lay, T., Williams, Q. & Garnero, E. J. (1998). The core–mantle boundary layer and deep Earth dynamics. *Nature* **392**, 461–468.

Lebensohn, R. A. & Tomé, C. N. (1993). A self-consistent anisotropic approach for the simulation of plastic deformation and texture development of polycrystals: Application to zirconium alloys. *Acta Metallurgica Et Materialia* **41**.

Lebensohn, R. A. & Tomé, C. N. (1994). A self-consistent viscoplastic model: prediction of rolling textures of anisotropic polycrystals. *Materials Science and Engineering A* **175**, 71–82.

Li, C., Van Der Hilst, R. D., Engdahl, E. R. & Burdick, S. (2008). A new global model for P wave speed variations in Earth's mantle. *Geochemistry, Geophysics, Geosystems* **9**.

Liermann, H.-P., Merkel, S., Miyagi, L., Wenk, H.-R., Shen, G., Cynn, H. & Evans, W. J. (2009). Experimental method for in situ determination of material textures at simultaneous high pressure and high temperature by means of radial diffraction in the diamond anvil cell. *The Review of scientific instruments* **80**, 104501.

Liermann, H. P. *et al.* (2015). The Extreme Conditions Beamline P02.2 and the Extreme Conditions Science Infrastructure at PETRA III. *Journal of synchrotron radiation* **22**, 908–24.

Lin, F., Hilairet, N., Raterron, P., Addad, A., Immoor, J., Marquardt, H., Tomé, C. N., Miyagi, L. & Merkel, S. (2017). Elasto-viscoplastic self consistent modeling of the ambient temperature plastic behavior of periclase deformed up to 5.4 GPa. *Journal of Applied Physics* **122**.

Lin, F., Speziale, S., Mao, Z., Marquardt, H. & Science, G. (2013). Effects of the electronic spin transitions of iron in lower--mantle minerals: implications for deep--mantle geophysics and geochemistry. 244–275.

Lin, J.-F., Wenk, H.-R., Voltolini, M., Speziale, S., Shu, J. & Duffy, T. S. (2009). Deformation of lower-mantle ferropericlase (Mg,Fe)O across the electronic spin transition. *Physics and Chemistry of Minerals* **36**, 585–592.

Liu, L.-G. & Bassett, W. A. (1975). The melting of iron up to 200 kbar. *Journal of Geophysical Research (1896-1977)* **80**, 3777–3782.

Liu, Z., Park, J. & Karato, S. I. (2016). Seismological detection of low-velocity anomalies surrounding the mantle transition zone in Japan subduction zone. *Geophysical Research Letters* **43**.

Lutterotti, L., Matthies, S., Wenk, H.-R., Schultz, A. S. & Richardson, J. W. (1997). Combined texture and structure analysis of deformed limestone from time-of-flight neutron diffraction spectra. *Journal of Applied Physics*. AIP Publishing **81**, 594.

Lutterotti, L., Vasin, R. & Wenk, H.-R. (2014). Rietveld texture analysis from synchrotron diffraction images. I. Calibration and basic analysis. *Powder Diffraction* **29**, 76–84.

Lynner, C. & Long, M. D. (2014). Lowermost mantle anisotropy and deformation along the boundary of the African LLSVP. *Geophysical Research Letters* **41**, 3447–3454.

Mao, H. K. & Bell, P. M. (1978). High-pressure physics: Sustained static generation of 1.36 to 1.72 megabars. *Science* **200**.

Mao, H. K. & Bell, P. M. (1979). *Mao, H. K., and P. M. Bell. "Design of the diamond-window, high-pressure apparatus for cryogenic experiments.* Carnegie Inst. Washington Year Book 7.

Marquardt, H. & Miyagi, L. (2015). Slab stagnation in the shallow lower mantle linked to an increase in mantle viscosity. *Nature Geoscience* **8**, 311–314.

Marquardt, H., Speziale, S., Reichmann, H. J., Frost, D. J., Schilling, F. R. & Garnero, E. J. (2009). Elastic shear anisotropy of ferropericlase in Earth's lower mantle. *Science* **324**, 224–226.

Marquardt, H. & Thomson, A. R. (2020). Experimental elasticity of Earth's deep mantle. *Nature Reviews Earth & Environment* **1**, 455–469.

Matthies, S. & Humbert, M. (1993). The Realization of the Concept of a Geometric Mean for Calculating Physical Constants of Polycrystalline Materials. *physica status solidi (b)* **177**.

Matthies, S. & Vinel, G. W. (1982). On the Reproduction of the Orientation Distribution Function of Texturized Samples from Reduced Pole Figures Using the Conception of a Conditional Ghost Correction. *physica status solidi (b)* **112**.

McNamara, A. K., van Keken, P. E. & Karato, S.-I. (2002). Development of anisotropic structure in the Earth's lower mantle by solid-state convection. *Nature*. Macmillian Magazines Ltd. **416**, 310–4.

McNamara, A. K. & Zhong, S. (2005). Thermochemical structures beneath Africa and the Pacific Ocean. *Nature* **437**.

Merkel, S. (2002). Deformation of polycrystalline MgO at pressures of the lower mantle. *Journal of Geophysical Research* **107**, 2271.

Merkel, S. (2006). X-ray diffraction evaluation of stress in high pressure deformation experiments. *Journal of physics. Condensed matter : an Institute of Physics journal* **18**, S949-62.

Merkel, S., Liermann, H.-P., Miyagi, L. & Wenk, H.-R. (2013). In situ radial X-ray diffraction study of texture and stress during phase transformations in bcc-, fcc- and hcp-iron up to 36GPa and 1000K. *Acta Materialia* **61**, 5144–5151.

Merkel, S., McNamara, A. K., Kubo, A., Speziale, S., Miyagi, L., Meng, Y., Duffy, T. S. & Wenk, H. R. (2007). Deformation of (Mg,Fe)SiO3 post-perovskite and D″ anisotropy. *Science* **316**, 1729–1732.

Merkel, S., Tomé, C. & Wenk, H.-R. (2009). Modeling analysis of the influence of plasticity on high pressure deformation of hcp-Co. *Physical Review B* **79**, 064110.

Merkel, S., Wenk, H. R., Badro, J., Montagnac, G., Gillet, P., Mao, H. K. & Hemley, R. J. (2003). Deformation of (Mg0.9,Fe0.1)SiO3 Perovskite aggregates up to 32 GPa. *Earth and Planetary Science Letters* **209**, 351–360.

Merkel, S. & Yagi, T. (2005). X-ray transparent gasket for diamond anvil cell high pressure experiments. *Review of Scientific Instruments* **76**, 046109.

Merrill, L. & Bassett, W. A. (1974). Miniature diamond anvil pressure cell for single crystal x-ray diffraction studies. *Review of Scientific Instruments* **45**.

Ming, L. & Bassett, W. A. (1974). Laser heating in the diamond anvil press up to 2000°C sustained and 3000°C pulsed at pressures up to 260 kilobars. *Review of Scientific Instruments* **45**, 1115–1118.

Miyagi, L., Kanitpanyacharoen, W., Kaercher, P., Lee, K. K. M. & Wenk, H. R. (2010). Slip systems in MgSiO3 post-perovskite: Implications for D″ anisotropy. *Science*.

Miyagi, L., Kanitpanyacharoen, W., Raju, S. V., Kaercher, P., Knight, J., MacDowell, A., Wenk, H. R., Williams, Q. & Alarcon, E. Z. (2013). Combined resistive and laser heating technique for in situ radial X-ray diffraction in the diamond anvil cell at high pressure and temperature. *Review of Scientific Instruments* **84**, 025118.

Miyagi, L., Merkel, S., Yagi, T., Sata, N., Ohishi, Y. & Wenk, H. R. (2009). Diamond anvil cell deformation of CaSiO3 perovskite up to 49 GPa. *Physics of the Earth and Planetary Interiors* **174**, 159–164.

Miyagi, L. & Wenk, H.-R. (2016). Texture development and slip systems in bridgmanite and bridgmanite + ferropericlase aggregates. *Physics and Chemistry of Minerals*. Springer Berlin Heidelberg.

Moore, M. J., Sorensen, D. B. & Devries, R. C. (1970). A simple heating device for diamond anvil high pressure cells. *Review of Scientific Instruments*.

Morra, G., Yuen, D. A., Boschi, L., Chatelain, P., Koumoutsakos, P. & Tackley, P. J. (2010). The fate of the slabs interacting with a density/viscosity hill in the mid-mantle. *Physics of the Earth and Planetary Interiors*. Elsevier B.V. **180**, 271–282.

Muir, J. M. R. & Brodholt, J. P. (2018). Water distribution in the lower mantle: Implications for hydrolytic weakening. *Earth and Planetary Science Letters* **484**.

Murakami, M., Hirose, K., Kawamura, K., Sata, N. & Ohishi, Y. (2004). Post-Perovskite Phase Transition in MgSiO3. *Science* **304**.

Nestola, F. *et al.* (2018). CaSiO3 perovskite in diamond indicates the recycling of oceanic crust into the lower mantle. *Nature* **555**.

Nowacki, A., Walker, A. M., Wookey, J. & Kendall, J. M. (2013). Evaluating post-perovskite as a cause of D" anisotropy in regions of palaeosubduction. *Geophysical Journal International* **192**, 1085–1090.

Nowacki, A., Wookey, J. & Kendall, J. M. (2011). New advances in using seismic anisotropy, mineral physics and geodynamics to understand deformation in the lowermost mantle. *Journal of Geodynamics* **52**, 205–228.

O'Nions, R. K. & Tolstikhin, I. N. (1996). Limits on the mass flux between lower and upper mantle and stability of layering. *Earth and Planetary Science Letters* **139**, 213–222.

Ono, S., Ito, E. & Katsura, T. (2001). Mineralogy of subducted basaltic crust (MORB) from 25 to 37 GPa, and chemical heterogeneity of the lower mantle. *Earth and Planetary Science Letters* **190**.

Panning, M. (2004). Inferences on Flow at the Base of Earth's Mantle Based on Seismic Anisotropy. *Science* **303**, 351–353.

Paterson, M. S. & Weaver, C. W. (1970). Deformation of Polycrystalline Under Pressure. *Journal of the American Ceramic Society* **53**, 463–471.

Perrillat, J. P., Ricolleau, A., Daniel, I., Fiquet, G., Mezouar, M., Guignot, N. & Cardon, H. (2006). Phase transformations of subducted basaltic crust in the upmost lower mantle. *Physics of the Earth and Planetary Interiors* **157**.

Piermarini, G. J. & Weir, C. E. (1962). A diamond cell for x-ray diffraction studies at high pressures. *Journal of Research of the National Bureau of Standards Section A: Physics and Chemistry* **66A**.

Rietveld, H. M. (1969). A profile refinement method for nuclear and magnetic structures. *Journal of Applied Crystallography*. International Union of Crystallography **2**, 65–71.

Ringwood, A. E. (1991). Phase transformations and their bearing on the constitution and dynamics of the mantle. *Geochimica et Cosmochimica Acta* **55**, 2083–2110.

Romanowicz, B. & Wenk, H. R. (2017). Anisotropy in the deep Earth. *Physics of the Earth and Planetary Interiors*. Elsevier B.V. **269**, 58–90.

Saikia, A., Frost, D. J. & Rubie, D. C. (2008). Splitting of the 520-kilometer seismic discontinuity and chemical heterogeneity in the mantle. *Science* **319**.

Shieh, S. R., Duffy, T. S. & Shen, G. (2004). Elasticity and strength of calcium silicate perovskite at lower mantle pressures. *Physics of the Earth and Planetary Interiors* **143**.

Shim, S.-H., Duffy, T. S. & Shen, G. (2001). The post-spinel transformation in Mg2SiO4 and its relation to the 660-km seismic discontinuity. *Nature* **411**, 571–574.

Shim, S.-H., Jeanloz, R. & Duffy, T. S. (2002). Tetragonal structure of CaSiO 3 perovskite above 20 GPa. *Geophysical Research Letters* **29**, 19.

Singh, A. K., Balasingh, C., Mao, H. K., Hemley, R. J. & Shu, J. (1998). Analysis of lattice strains measured under nonhydrostatic pressure. *Journal of Applied Physics* **83**, 7567–7575.

Speziale, S., Immoor, J., Ermakov, A., Merkel, S., Marquardt, H. & Liermann, H. P. (2019). The equation of state of TaC0.99 by X-ray diffraction in radial scattering geometry to 32 GPa and 1073 K. *Journal of Applied Physics*. AIP Publishing LLC **126**, 0–12.

Srinivasan, M. & Stoebe, T. G. (1974). Temperature dependence of yielding and work-hardening rates in magnesium oxide single crystals. *Journal of Materials Science* **9**, 121–128.

Stixrude, L. & Lithgow-Bertelloni, C. (2011). Thermodynamics of mantle minerals - II. Phase equilibria. *Geophysical Journal International* **184**.

Stixrude, L., Lithgow-Bertelloni, C., Kiefer, B. & Fumagalli, P. (2007). Phase stability and shear softening in CaSi O3 perovskite at high pressure. *Physical Review B* **75**, 024108.

Stretton, I., Heidelbach, F., Mackwell, S. & Langenhorst, F. (2001). Dislocation creep of magnesiowüstite (Mg0.8Fe0.2O). *Earth and Planetary Science Letters* **194**, 229–240.

Sun, N., Mao, Z., Yan, S., Wu, X., Prakapenka, V. B. & Lin, J. F. (2016). Confirming a pyrolitic lower mantle using self-consistent pressure scales and new constraints on CaSiO3 perovskite. *Journal of Geophysical Research: Solid Earth* **121**.

Tackley, P. J. (2000). Mantle Convection and Plate Tectonics: Toward an Integrated Physical and Chemical Theory. *Science* **288**, 2002–2007.

Takeda, Y.-T. (1998a). Flow in rocks modelled as multiphase continua: application to polymineralic rocks. *Journal of Structural Geology* **20**, 1569–1578.

Takeda, Y. T. (1998b). Flow in rocks modelled as multiphase continua: Application to polymineralic rocks. *Journal of Structural Geology* **20**, 1569–1578.

Thielmann, M., Golabek, G. J. & Marquardt, H. (2020). Ferropericlase Control of Lower Mantle Rheology: Impact of Phase Morphology. *Geochemistry, Geophysics, Geosystems* **21**.

Thomson, A. R., Crichton, W. A., Brodholt, J. P., Wood, I. G., Siersch, N. C., Muir, J. M. R., Dobson, D. P. & Hunt, S. A. (2019). Seismic velocities of CaSiO3 perovskite can explain LLSVPs in Earth's lower mantle. *Nature*. Springer US **572**, 643–647.

Tommaseo, C. E., Devine, J., Merkel, S., Speziale, S. & Wenk, H. R. (2006). Texture development and elastic stresses in magnesiowustite at high pressure. *Physics and Chemistry of Minerals* **33**, 84–97.

Tsuchiya, T. (2011). Elasticity of subducted basaltic crust at the lower mantle pressures: Insights on the nature of deep mantle heterogeneity. *Physics of the Earth and Planetary Interiors* **188**.

Tsujino, N., Nishihara, Y., Yamazaki, D., Seto, Y., Higo, Y. & Takahashi, E. (2016). Mantle dynamics inferred from the crystallographic preferred orientation of bridgmanite. *Nature* **539**, 81–84.

Uchida, T. *et al.* (2009). Non-cubic crystal symmetry of CaSiO3 perovskite up to 18 GPa and 1600 K. *Earth and Planetary Science Letters* **282**, 268–274.

van der Hilst, R. D., Widiyantoro, S. & Engdahl, E. R. (1997). Evidence for deep mantle circulation from global tomography. *Nature*, 578–584.

Van Keken, P. E., Karato, S. & Yuen, D. A. (1996). Rheological control of oceanic crust separation in the transition zone. *Geophysical Research Letters* **23**.

Walker, A. M., Dobson, D. P., Wookey, J., Nowacki, A. & Forte, A. M. (2018). The anisotropic signal of topotaxy during phase transitions in D″. *Physics of the Earth and Planetary Interiors* **276**.

Walker, A. M., Forte, A. M., Wookey, J., Nowacki, A. & Kendall, J. M. (2011). Elastic anisotropy of D″ predicted from global models of mantle flow. *Geochemistry, Geophysics, Geosystems* **12**.

Walte, N. P., Heidelbach, F., Miyajima, N., Frost, D. J., Rubie, D. C. & Dobson, D. P. (2009). Transformation textures in post-perovskite: Understanding mantle flow in the D' layer of the earth. *Geophysical Research Letters* **36**, 3–7.

Walter, M. J., Kohn, S. C., Araujo, D., Bulanova, G. P., Smith, C. B., Gaillou, E., Wang, J., Steele, A. & Shirey, S. B. (2011). Deep Mantle Cycling of Oceanic Crust: Evidence from Diamonds and Their Mineral Inclusions. *Science* **334**, 54–57.

Wang, H., Wu, P. D., Tomé, C. N. & Huang, Y. (2010). A finite strain elastic-viscoplastic self-consistent model for polycrystalline materials. *Journal of the Mechanics and Physics of Solids* **58**, 594–612.

Wang, Y., Durham, W. B., Getting, I. C. & Weidner, D. J. (2003). The deformation-DIA: A new apparatus for high temperature triaxial deformation to pressures up to 15 GPa. *Review of Scientific Instruments* **74**, 3002–3011.

Wang, Y., Hilairet, N., Nishiyama, N., Yahata, N., Tsuchiya, T., Morard, G. & Fiquet, G. (2013). High-pressure, high-temperature deformation of CaGeO 3 (perovskite)?MgO aggregates: Implications for multiphase rheology of the lower mantle. *Geochemistry, Geophysics, Geosystems* **14**, 3389–3408.

Weaver, C. W. & Paterson, M. S. (1969). Deformation of Cube-Oriented MgO Crystals Under Pressure. *Journal of the American Ceramic Society* **52**, 293–302.

Weir, C. E., Lippincott, E. R., Van Valkenburg, A. & Bunting, E. N. (1959). Infrared studies in the 1- to 15-micron region to 30,000 atmospheres. *Journal of Research of the National Bureau of Standards Section A: Physics and Chemistry* **63A**, 55.

Wenk, H.-R., Baumgardner, J. R., Lebensohn, R. A. & Tomé, C. N. (2000a). A convection model to explain anisotropy of the inner core. *Journal of Geophysical Research: Solid Earth* **105**, 5663–5677.

Wenk, H.-R., Lonardelli, I., Merkel, S., Miyagi, L., Pehl, J., Speziale, S. & Tommaseo, C. E. (2006a). Deformation textures produced in diamond anvil experiments, analysed in radial diffraction geometry. *Journal of Physics: Condensed Matter* **18**, S933–S947.

Wenk, H.-R., Lutterotti, L., Kaercher, P., Kanitpanyacharoen, W., Miyagi, L. & Vasin, R. (2014). Rietveld texture analysis from synchrotron diffraction images. II. Complex multiphase materials and diamond anvil cell experiments. *Powder Diffraction* **29**, 220–232.

Wenk, H. R., Baumgardner, J. R., Lebensohn, R. A. & Tomé, C. N. (2000b). A convection model to explain anisotropy of the inner core. *Journal of Geophysical Research: Solid Earth* **105**, 5663–5677.

Wenk, H. R., Cottaar, S., Tomé, C. N., McNamara, A. & Romanowicz, B. (2011). Deformation in the lowermost mantle: From polycrystal plasticity to seismic anisotropy. *Earth and Planetary Science Letters*. Elsevier B.V. **306**, 33–45.

Wenk, H. R., Matthies, S., Donovan, J. & Chateigner, D. (1998). BEARTEX: a Windows-based program system for quantitative texture analysis. *Journal of Applied Crystallography*. International Union of Crystallography **31**, 262–269.

Wenk, H. R., Speziale, S., McNamara, A. K. & Garnero, E. J. (2006b). Modeling lower mantle anisotropy development in a subducting slab. *Earth and Planetary Science Letters* **245**, 302–314.

Wentzcovitch, R. M., Karki, B. B., Cococcioni, M. & De Gironcoli, S. (2004). Thermoelastic Properties of MgSiO3-Perovskite: Insights on the Nature of the Earth's Lower Mantle. *Physical Review Letters* **92**.

Wu, X., Lin, J. F., Kaercher, P., Mao, Z., Liu, J., Wenk, H. R. & Prakapenka, V. B. (2017). Seismic anisotropy of the D″ layer induced by (001) deformation of post-perovskite. *Nature Communications* **8**.

Yamazaki, D. (2002). Fabric development in (Mg, Fe) O during large strain, shear deformation: implications for seismic anisotropy in Earth's lower mantle. *Physics of the Earth and Planetary Interiors* **131**, 251–267.

Yamazaki, D. & Karato, S.-I. (2001a). High-pressure rotational deformation apparatus to 15 GPa. *Review of Scientific Instruments* **72**, 4207.

Yamazaki, D. & Karato, S. (2001b). Some mineral physics constraints on the rheology and geothermal structure of Earth's lower mantle. *American Mineralogist* **86**, 385–391.

Yamazaki, D., Lee, K. & Karato, S. (1999). Deformation experiments on MnTiO3+ MnO as an analogue of lower mantle materials. *Eos Trans. AGU*.

Yamazaki, D., Yoshino, T., Matsuzaki, T., Katsura, T. & Yoneda, A. (2009). Texture of (Mg,Fe)SiO3 perovskite and ferro-periclase aggregate: Implications for rheology of the lower mantle. *Physics of the Earth and Planetary Interiors* **174**.

References

Chapter 4
List of papers and author contributions

Chapters 5, 6 and 7 are word to word reprints of the manuscript as they were by the time this thesis was submitted. Changes due to review process can occur for the last manuscript.

The first paper *An improved setup for radial diffraction experiments at high pressures and high temperatures in a resistive graphite-heated diamond anvil cell* by J. Immoor, H. Marquardt, L. Miyagi, S. Speziale, S. Merkel, I. Schwark, A. Ehnes, and H.- P. Liermann is published in REVIEW OF SCIENTIFIC INSTRUMENTS, 2020, VOL 045121, NO. 91, p. 045121-1 – 045121 -7, DOI: 10.1063/1.5143293.
This project was proposed by H. Marquardt and H.P. Liermann. H.-P. Liermann designed the water-cooled vacuum chamber together with I. Schwark and A. Ehnes. J. Immoor prepared all diamond anvil cells including the graphite-heaters. J. Immoor processed and analysed the presented diffraction data. J. Immoor and H. Marquardt wrote the manuscript, L. Miyagi, S. Speziale, S. Merkel and H.P. Liermann commented on it.

The second paper *Evidence for {100}<011> slip in ferropericlase in Earth's lower mantle from high-pressure/high-temperature experiments* by J. Immoor, H. Marquardt, L. Miyagi, F. Lin, S. Speziale, S. Merkel, J. Buchen, A. Kurnosov and H.-P. Liermann is published in EARTH AND PLANETARY SCIENCE LETTERS, 2018, VOL. 489, p. 251 – 257,
DOI: https://doi.org/10.1016/j.epsl.2018.02.045.
This project was proposed by H. Marquardt. J. Immoor prepared all diamond anvil cells including the graphite-heaters. J. Immoor performed the experiments. S. Speziale, J. Buchen and A. Kurnosov supported the experiments. J. Immoor processed and analysed the presented diffraction data. L. Miyagi, F. Lin and S. Merkel modelled the experimental data supported by J. Immoor. H. Marquardt and J. Immoor wrote the manuscript, L. Miyagi, F. Lin, S. Speziale, S. Merkel, J. Buchen, A. Kurnosov and H.-P. Liermann commented on it.

Chapter 4
List of papers and author contributions

The third paper *Weak Cubic $CaSiO_3$ Perovskite in Earth's Mantle* by J. Immoor, L. Miyagi, H.- P. Liermann, S. Speziale, K. Schulze, J. Buchen, A. Kurnosov and H. Marquardt was resubmitted after revision to NATURE on December 10th, 2021 and is currently under review. H. Marquardt, H.-P. Liermann, L. Miyagi, S. Speziale designed the research. J. Immoor prepared the experiments. All author contributed to the Synchrotron experiments. J. Immoor and L. Miyagi analysed the data. H. Marquardt performed the modelling. H. Marquardt wrote the initial draft of the manuscript. All authors contributed to the final writing of the manuscript.

Chapter 5

An improved setup for radial diffraction experiments at high pressures and high temperatures in a resistive graphite-heated diamond anvil cell

J. IMMOOR[1], H. MARQUARDT[2], L. MIYAGI[3], S. SPEZIALE,[4] S. MERKEL[5], I. SCHWARK[6], A. EHNES[6], and H.- P. LIERMANN[6]

[1]Bayerisches Geoinstitut BGI, University of Bayreuth, 95440 Bayreuth, Germany
[2]Department of Earth Sciences, University of Oxford, Oxford OX1 3AN, United Kingdom
[3]University of Utah, 115 So. 1460 E., Salt Lake City, Utah UT84112-0111, USA
[4]German Research Center for Geosciences GFZ, 14473 Potsdam, Germany
[5]Univ. Lille, CNRS, INRAE, Centrale Lille, UMR 8207 - UMET - Unité Matériaux et Transformations, F-59000 Lille, France
[6]Photon Sciences, Deutsches Elektronen-Synchrotron (DESY), 22607 Hamburg, Germany Corresponding author: Julia.immoor@uni-bayreuth.de

This chapter has been published and reproduced from Rev. Sci. Instrum. **91**, 045121 (2020). https://doi.org/10.1063/1.5143293 with the permission of AIP Publishing.
Submitted: 22 December 2019 • Accepted: 07 April 2020 • Published Online: 28 April 2020

Abstract

We present an improved setup for the experimental study of deformation of solids at simultaneous high pressures and temperatures by radial x-ray diffraction. This technique employs a graphite resistive heated Mao–Bell type diamond anvil cell for radial x-ray diffraction in combination with a water-cooled vacuum chamber. The new chamber has been developed by the sample environment group at PETRA III and implemented at the Extreme Conditions Beamline P02.2 at PETRA III, DESY (Hamburg, Germany). We discuss applications of the new setup to study

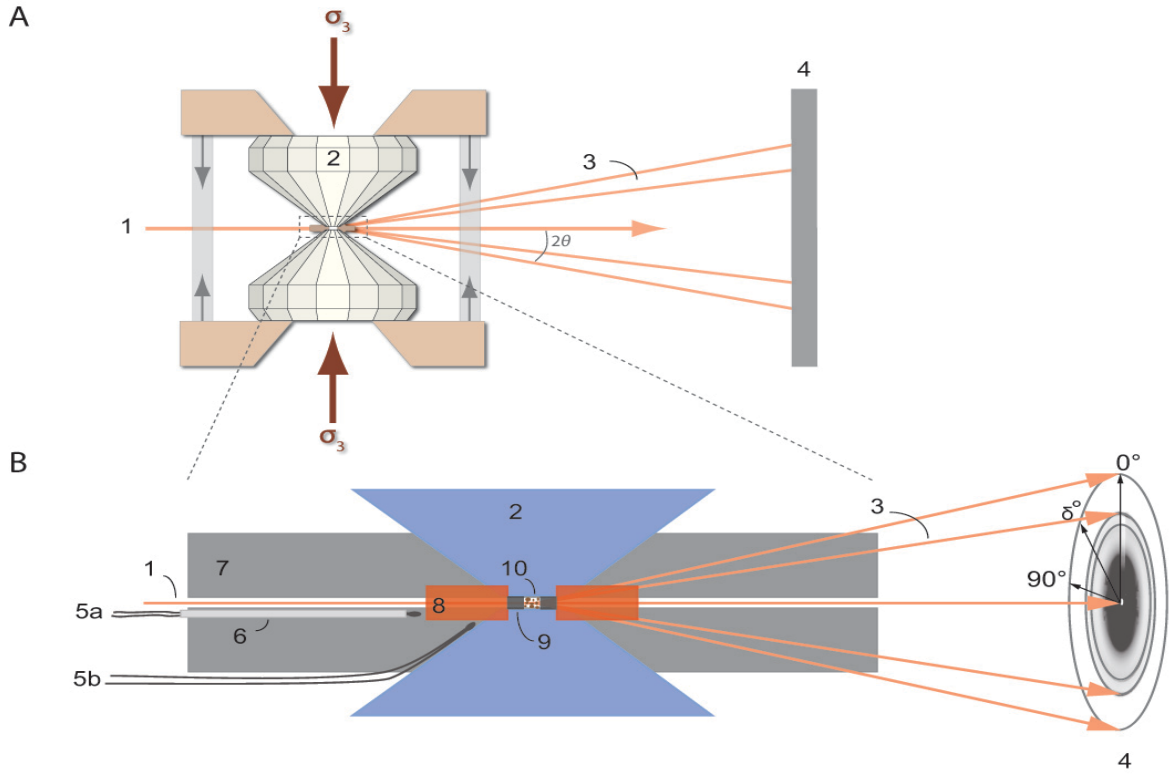

Figure 5.1: (a) Angle-dispersive high-pressure radial x-ray diffraction in a DAC (modified after Liermann et al., 2009), σ3: stress along compression direction, 2θ: diffraction angle, 1: incoming x-ray beam, 2: diamond anvil, 3: diffraction beam, and 4: area detector. (b) Magnification of the diamond anvil-culets showing the position for the two thermocouples (5a: between both graphite heaters and 5b: on the diamond anvil next to the culet). 6: ceramic sleeve, 7: flexible graphite sheet, 8: Kapton, 9: boron gasket, and 10: sample.

deformation of a variety of materials, including ferropericlase, calcium perovskite, bridgmanite, and tantalum carbide, at high-pressure/temperature.

5.1 Introduction

Understanding the physical and rheological properties of materials at simultaneous high pressures and temperatures is of key importance in Earth science as well as materials sciences. The rheological properties of Earth's mantle materials, for example, govern large-scale mantle convection (Karato and Wu, 1993; Kohlstedt, 2007; Girard et al., 2016; Tsujino et al., 2016). In addition, Crystallographic Preferred Orientation (CPO) caused by the alignment of mantle minerals during deformation leads to seismic anisotropy, providing a means to link seismic observations to the mantle flow (Karato, 1988; Karato et al., 1995; Tackley, 2000; Yamazaki and Karato, 2001b; Conrad et al., 2007; Nowacki et al., 2013; Creasy et al., 2017; Romanowicz and Wenk, 2017; Immoor et al., 2018). Several techniques have been developed in the past to study the rheology of materials under high pressure and temperature, but achievable pressures are mostly

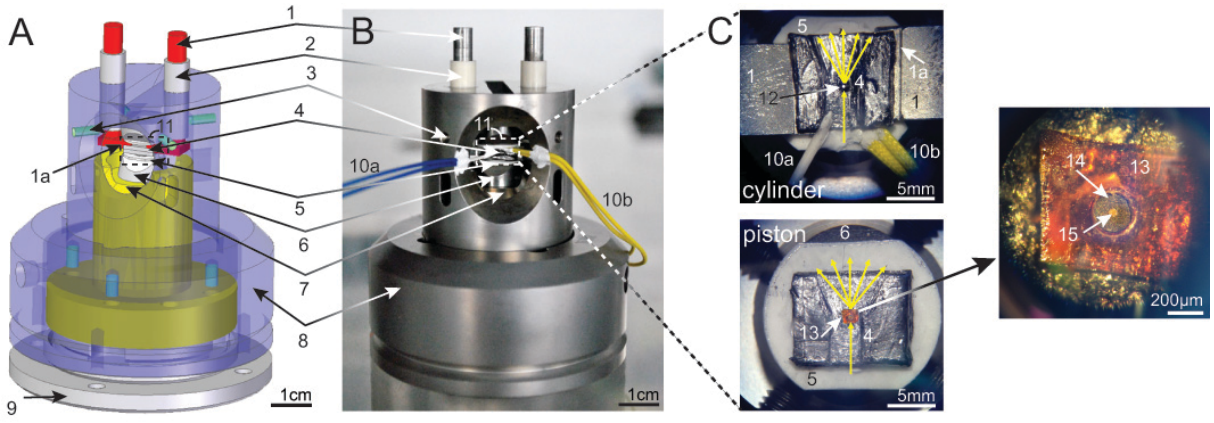

Figure 5.2: Experimental setup of a resistive-heated DAC (modified after Immoor et al., 2018). (a) 3D CAD model and (b) photograph of the resistive-heated DAC used for the experiments. 1: molybdenum rods (electrical contacts), 1a: strip with step at the end of the molybdenum rod, 2: ceramic sleeves, 3: screws, 4: graphite sheet, 5: ceramic plate, 6: tungsten carbide seat, 7: piston, 8: cylinder, 9: membrane cup (missing in B), 10a: thermocouple with ceramic sleeve, 10b: thermocouple, and 11: graphite-heater. (c) Close-up view of 11. Cylinder: 12—culet of a diamond and 4—flexible graphite sheet with carved space for the x-ray beam. The inset shows the lower diamond pressed into the graphite heater and illustrates the positions of the thermocouples. Piston: 13—Kapton, which supports a cubic boron nitride gasket or amorphous boron epoxy gasket (14) with powder sample in the sample chamber (15).

limited to those typical of the crust and upper mantle (Yamazaki and Karato, 2001a; Wang et al., 2003; Kawazoe et al., 2010, 2013; Girard et al., 2016; Hunt and Dobson, 2017).

Deformation experiments at deep lower mantle pressures are almost exclusively performed in diamond-anvil cells in combination with synchrotron-based *in-situ* x-ray diffraction in a radial geometry [Figure 5.1(a) and 5.1 (b)]. By employing the radial diffraction geometry, lattice strains and deviatoric stress as well as evolution of CPO can be derived from the analysis of *in-situ* diffraction images. Radial x-ray diffraction in DACs has been widely employed in Earth science as well as materials sciences, but high-pressure experiments have been mostly limited to room temperature (Wenk et al., 2000b, 2006a; Merkel, 2006; Tommaseo et al., 2006; Merkel et al., 2007; Miyagi et al., 2009; Marquardt and Miyagi, 2015). Early high-temperatures studies employed a laser-heated diamond anvil cell (DAC), but data analysis and interpretation is challenging due to temperature gradients in the sample (Kunz et al., 2007; Miyagi et al., 2013). Liermann et al. (2009) developed a resistive-heated DAC, which was tested up to 36 GPa and 1100 K while performing *in-situ* radial x-ray diffraction. The use of a resistive-heating setup reduces temperature gradients and provides more homogeneous heating of the entire sample chamber.

Here, we present a modified resistive-heated-radial-x-ray-diffraction-diamond-anvil-cell (RH- rXRD-DAC) [Figure 5.2 (a) and 5.2 (b)] and report on its performance during *in-situ* radial x-ray diffraction experiments at simultaneous high pressure and high temperature on several

polycrystalline samples. The main improvement as compared to the setup described by Liermann et al. (2009) is the development and implementation of a water-cooled vacuum chamber [Figure 5.3 (a) and 5.3 (b)] that also enables cooling of the piston of the Mao–Bell type DAC. This modification decreases heating and thermal expansion of the piston of the DAC but allows the cylinder to heat up, thus reducing friction between the piston and the cylinder during compression at high temperatures. The use of a vacuum chamber prevents the oxidation of the cell, the molybdenum rods, and the diamonds at very high temperatures. We discuss applications of the improved setup for studying the deformation behaviour of major materials expected in Earth's lower mantle as well as tantalum carbide.

5.2 Experimental method

In radial x-ray diffraction experiments, the incoming x-ray beam is oriented perpendicular to the compression direction, i.e., the axis of the diamond anvils [Figure 5.1 (a) and 5.1 (c): 1]. This setup provides the possibility to study the lattice strains, resulting from the effect of differential stress, together with the CPO of powder samples (Wenk *et al.*, 2006a). A pressure-transmitting medium is not used. This enhances the development of differential stress and texture. In order for x rays to reach the sample chamber in the radial diffraction geometry, x-ray transparent gaskets are required. Here, we used either x-ray transparent amorphous boron epoxy + kapton (Merkel and Yagi, 2005) or cubic boron nitride (cBN) epoxy (Miyagi et al., 2013) (10:1 Epotech 353ND) + kapton gaskets [Figure 5.1: 8 and 5.1: 9; Figure 5.2 (c): 13 and 14] to reach high pressures (Funamori and Sato, 2008). The culet sizes of the employed diamonds were 200 µm or 300 µm [Figure 5.2 (c): 12]. The setup of the graphite heater is similar on the piston and cylinder side of the DAC [Figure 5.2 (c)]. Diamonds are glued on tungsten carbide seats that are truncated at the side to increase the opening angle for diffracted x rays (Figure 5.2: 5). The seats are insulated from graphite by a ceramic ring (Figure 5.2: 4) fixed to the seat with OMEGABOND 500 liquid. The gaps between the ceramic plates and the diamonds are filled with ceramic glue (Resbond 989). The heads of the molybdenum rods end in horizontal strips with a small step at the end. A piece of graphite foil connects the molybdenum rods [Figure 5.2 (a): 1a, Figure 5.2 (b): 11, and Figure 5.2 (c): 1a] and serves as the heating element surrounding the diamond-anvils. A space is carved in the graphite foil to prevent diffraction of graphite contaminating the diffraction image. Two thermocouples (R- type) are attached to the cylinder side. One thermocouple is placed close to the tip of the diamond on the upstream side of the DAC and to the side of the path of the incident x-ray beam [Figure 5.2 (c): 10a]. The second thermocouple is positioned on the graphite sheet, likewise upstream, and to the side of the incident x-ray beam

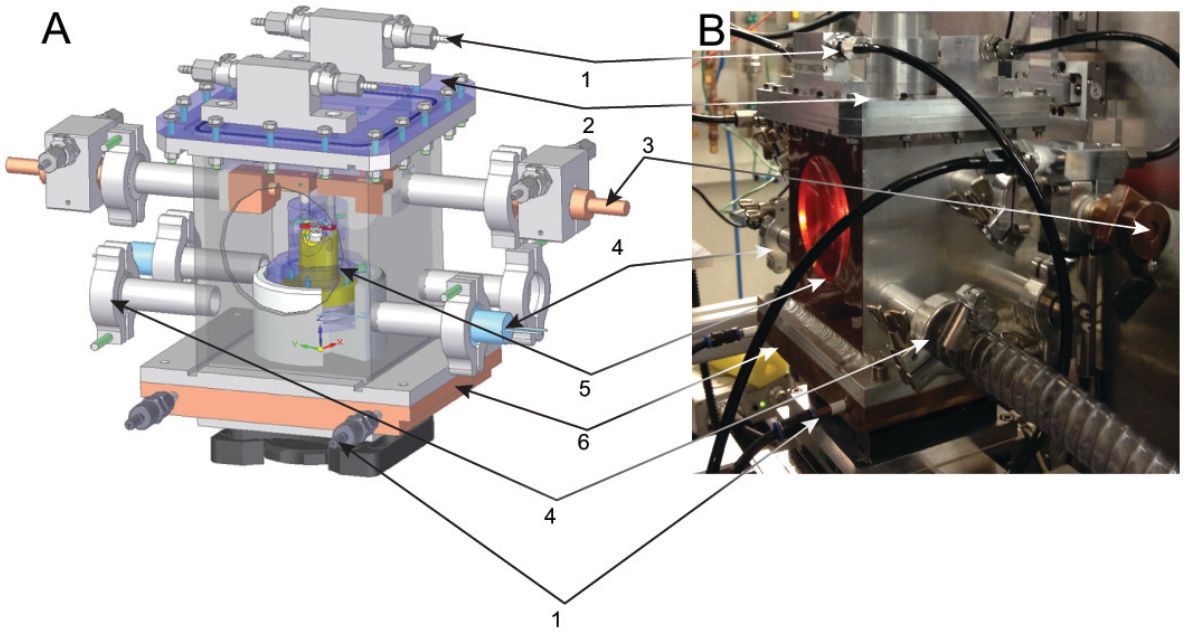

Figure 5.3: (a) 3D CAD model of the vacuum chamber. (b) Photograph of the vacuum chamber while performing a high-temperature experiment (~1400 K). 1: water cooling inlet/outlet, 2: lid with screws, 3: power supply connector, 4: vacuum pump connection, 5: Kapton window, and 6: copper cooling plate.

[Figure 5.12 (c): 10b]. When the cell is closed, the second thermocouple rests between the graphite sheets of the piston and the cylinder.

During the experiment, the temperature of the sample can be increased/decreased by varying an analog I/O signal from 0 V to 10 V using the beamline control system. This proportionally adjusts the power of the DC power supply from 0 W to 1800 W (0–8 V and 0–220 A) (Liermann et al., 2015). Pressure is changed remotely using a gas membrane device that is operated by using the membrane pressure controller APD200 from Sanchez Technology (Liermann et al., 2009; Merkel et al., 2013; Miyagi et al., 2013).

For high-pressure and high-temperature experiments, the RH- rXRD-DAC is placed in a newly designed water-cooled vacuum chamber that serves to both cool the DAC and prevent oxidation of the DAC, the molybdenum electrodes, the diamond anvils, and the graphite heater [Figure 5.3 (a) and 5.3 (b)]. The piston of the DAC is indirectly cooled through a steel pin that is connected to the base of the vacuum chamber, which is water-cooled. The differential cooling between the piston and the cylinder reduces the friction between the two parts of the DAC and enables a smoother pressure increase as compared to the previous experimental setup (Liermann et al., 2009; Miyagi et al., 2013). During the experiment, the vacuum in the chamber can be as good as 5 x 10^{-3} mbar. Note that, due to connections between the pump and the cell chamber,

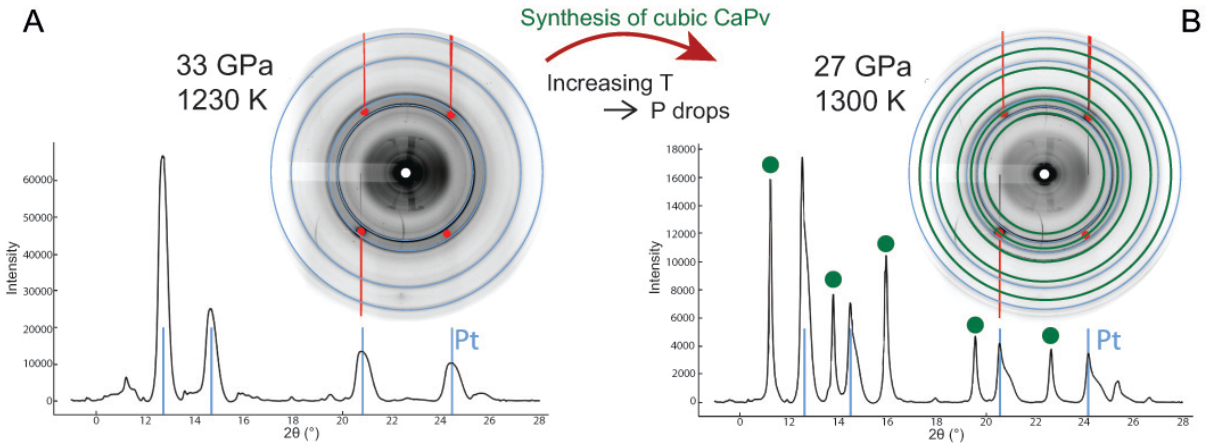

Figure 5.4: Synthesis of cubic calcium perovskite. The pressure was calculated from the stronger Pt peak. (a) X-ray diffraction image at 33 GPa and 1230 K shows rings of Pt (blue), which are used to estimate the pressure during the experiment and diamond single-crystal diffraction spots (red). The corresponding integrated diffraction pattern is shown below with blue line indicating Pt peaks. (b) X-ray diffraction image at 27 GPa and 1300 K with Debye rings of Pt (blue), Debye rings of calcium perovskite (green), and diamond diffraction spots (red). At the bottom, integrated diffraction pattern with blue lines indicating Pt peaks and green dots indicating calcium perovskite peaks. In both panel (a) and (b), the diffraction lines of diamond are masked in the integration and are absent in the diffraction patterns.

vacuum levels around the diamond anvil cells may not be as efficient. Nevertheless, the achieved vacuum is sufficient to perform experiments with minimal oxidation of the heating elements.

5.3 Results and discussion

The new setup has been tested during different experimental campaigns at the Extreme Conditions Beamline (ECB) P02.2 at PETRA III, DESY (Hamburg, Germany). Diffraction images were collected with a XRD 1621 flat panel detector from Perkin Elmer. In the following, we will describe some selected experiments in order to illustrate the capability of the new setup for Earth and materials science research. We report on the deformation of polycrystalline samples of ferropericlase [$(Mg_{0.8}Fe_{0.2})O$], the *in-situ* synthesis and deformation of cubic Ca-Pv ($CaSiO_3$), experiments performed on a two-phase mixture of bridgmanite ($MgSiO_3$) and ferropericlase, synthesized from a mixture of enstatite glass + ferropericlase in the resistive-heated DAC, and the high-temperature compression of tantalum carbide ($TaC_{0.99}$), an ultra-high temperature ceramic material.

5.4 *In-situ* deformation of ferropericlase

Ferropericlase is the second most abundant mineral in Earth's lower mantle. It may play a key role in mantle dynamics since it is rheologically weaker than bridgmanite, the dominant lower

mantle phase. Furthermore, it shows a pronounced elastic anisotropy, making it one of the candidates to explain seismic shear wave polarization anisotropy in the lower mantle (Marquardt et al., 2009). However, previous deformation studies at pressures of the lower mantle were limited to room temperature due to experimental complexity (Merkel, 2002; Tommaseo et al., 2006; Wenk et al., 2006a; Lin et al., 2009; Miyagi et al., 2009; Marquardt and Miyagi, 2015). In the work of Immoor et al., we used the described setup to measure the deformation of ferropericlase to 62 GPa at 1400 K and to higher pressures but at lower temperature. In our 1400 K run, the pressure of the sample was increased up to 40 GPa at room temperature and, afterward, heated up to 1400 K. During heating, the pressure of the sample dropped to below 20 GPa. We increased the pressure again and reached 62 GPa when diamond failure stopped the experiment. During compression, we collected high quality diffraction images of ferropericlase. Based on these results, we were able to monitor the evolution of CPO in ferropericlase and confirm a change in the slip system activity at high temperature, as predicted by computations (Immoor et al., 2018).

5.5 *In-situ* synthesis and deformation of cubic $CaSiO_3$

$CaSiO_3$ perovskite is expected to be an important mineral in Earth's transition zone and lower mantle, where it is the third most abundant phase for a pyrolitic mantle composition (Frost, 2008). In a deeply subducted oceanic slab, $CaSiO_3$ perovskite may account for up to 25 Vol. % of the transformed basaltic crust (Irifune and Tsuchiya, 2015) and will affect the bulk rheological properties of the lithospheric slab. According to a recent computational study (Kawai and Tsuchiya, 2015), the shear wave anisotropy of $CaSiO_3$ perovskite is about 15 % – 30 % at conditions of the lower mantle. A strong CPO of $CaSiO_3$ perovskite may, therefore, contribute to seismic anisotropy observations, in particular, in the shallow lower mantle or lowermost transition zone, where the elastic anisotropy is strongest. A previous $CaSiO_3$ perovskite study has been limited to 49 GPa under ambient conditions (Miyagi et al., 2009). At these conditions, however, $CaSiO_3$ perovskite forms a pseudo cubic structure, and the exact nature of the distortion is still under debate (Shim et al., 2002; Caracas et al., 2005; Jung and Oganov, 2005; Adams and Oganov, 2006), whereas at temperatures typical for the lower mantle, the structure is cubic (Pm3m) (Caracas et al., 2005; Jung and Oganov, 2005; Adams and Oganov, 2006; Komabayashi et al., 2007) and may show a different rheological behavior. $CaSiO_3$ perovskite can be experimentally synthesized from $CaSiO_3$ wollastonite at pressures of about 20 GPa and temperatures of about 1300 K (Uchida et al., 2009) but is not quenchable under ambient conditions. This implies that studies of the physical properties of $CaSiO_3$ perovskite need to be performed *in-situ* and in the same pressure device where it has been synthesized.

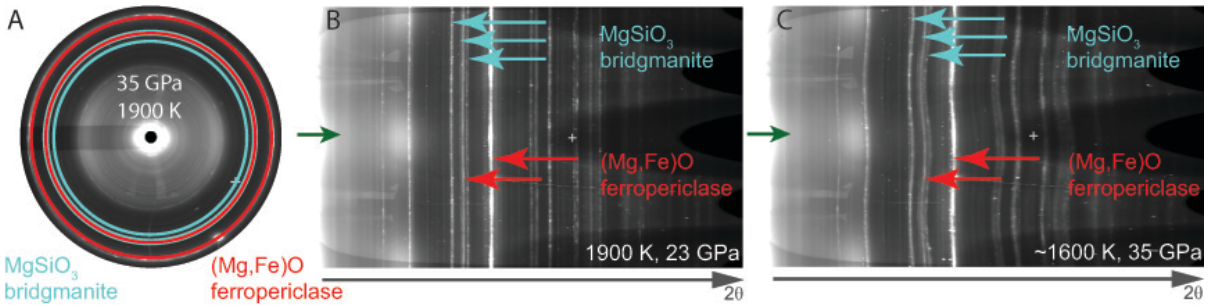

Figure 5.5: Synthesis of bridgmanite (blue) + ferropericlase (red). Dark green arrows indicate the compression direction in the unrolled radial x-ray diffraction image. (a) Diffraction rings of bridgmanite and ferropericlase at 35 GPa and 1900 K. (b) Unrolled image with the straight unrolled diffraction rings of bridgmanite and ferropericlase at 23 GPa and 1900 K. (c) The unrolled diffraction image shows the curved diffraction rings of bridgmanite and ferropericlase after a pressure increase up to 35 GPa at ~1600 K. Ferropericlase was used as the pressure calibrant.

Using the improved RH-rXRD-DAC, we were able to synthesize $CaSiO_3$ perovskite and performed several successful deformation experiments reaching temperatures of up to 1500 K at pressures of 45 GPa. The starting material was amorphous $CaSiO_3$ mixed with platinum powder as the pressure standard. Figure 5.4 shows two diffraction images collected during a compression experiment that reached a final pressure of 40 GPa at 1300 K. Cubic $CaSiO_3$ perovskite was synthesized after increasing the temperature to 1300 K at which point the pressure dropped from 33 GPa to 27 GPa as a result of the phase transition [Figure 5.4 (b)]. The collected diffraction patterns show smooth diffraction rings, indicating a relatively small and homogeneous grain size of the synthesized cubic $CaSiO_3$ perovskite. The large pressure drop at the transition also caused strain heterogeneity in Pt finely mixed with the sample [see Pt peaks asymmetry in Figure 5.4 (b)].

5.6 Synthesis of bridgmanite and ferropericlase

The deformation behavior of multiphase rock assemblies might substantially differ from the behavior of single-phase assemblies, particularly if the phases show large differences in rheological properties (Karato, 1981; Handy, 1994; Takeda, 1998b; Merkel, 2002; Thielmann et al., 2020). The lower mantle can be modeled as a two-phase mixture of bridgmanite and ferropericlase, two phases that show large differences in plastic strength and viscosity (Yamazaki and Karato, 2001b; Marquardt and Miyagi, 2015; Girard et al., 2016). Because of this large contrast in rheological strength, it is difficult to predict mantle properties, including viscosity and seismic anisotropy, from single-phase measurements. There have been few deformation experiments on analogues (Wang et al., 2013; Kaercher et al., 2016), as well as on a true two-phase lower mantle mixture, at pressures and temperature of the very top of the lower mantle using a rational Drickamer

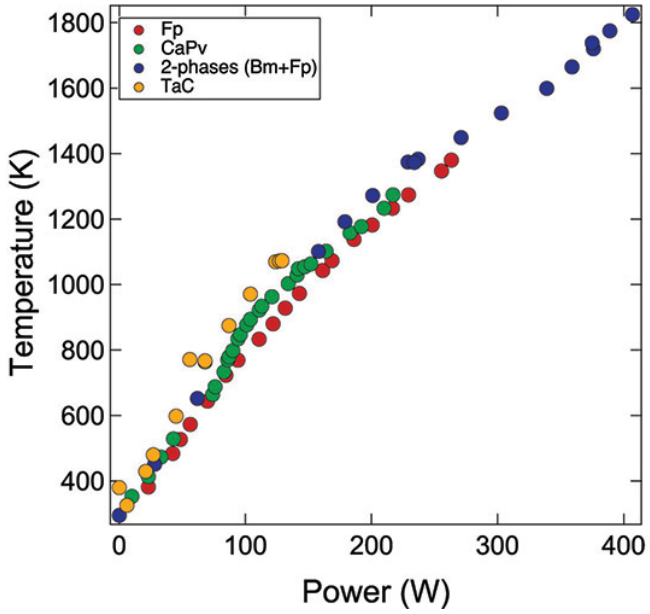

Figure 5.6: Power–temperature curves of different experiments. Symbols: Fp is ferropericlase, CaPv is calcium perovskite, Bm is bridgmanite, and TaC is tantalum carbide.

apparatus (Girard et al., 2016). Here, we used the improved RH-rXRD-DAC to synthesize a bridgmanite and ferropericlase assembly [Figure 5.5 (a) and 5.4 (b)] from an enstatite glass powder mixed with ferropericlase and applied deviatoric stress to the two-phase mixture at high temperatures [Figure 5.5 (c)]. In one successful run, we first increased the pressure to 58 GPa and the temperature to 1600 K. Afterward, the pressure in the sample decreased while increasing the temperature continuously to 1900 K. A peak splitting of ferropericlase was observed, likely as a result of pressure gradients in the sample chamber, followed by the appearance of the typical diffraction ring triplet of the new phase bridgmanite. Bridgmanite grew, while the pressure continued to decrease when the thermocouples stopped working. During a subsequent decrease in voltage and, therefore, presumably in temperature (based on power–temperature relation; see Figure 5.6), the pressure in the sample chamber increased again to 35 GPa, leading to deformation of the sample [Figure 5.5 (c)].

5.7 Compression of tantalum carbide ($TaC_{0.99}$)

Carbides are characterized by high mechanical and thermal stability and play an important role in industrial applications, where they are used, for example, as coatings for abrasive tools. Many experimental and computational studies have been conducted on tantalum carbide (see Ref. Speziale et al., 2019). However, no experiments have been performed to study the behaviour of this phase under simultaneous high pressure, high temperature, and deviatoric stress. We

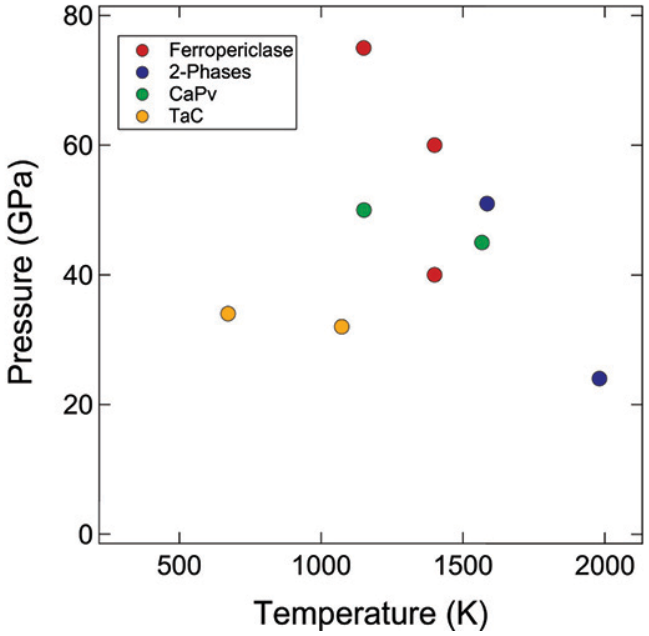

Figure 5. 7: Maximum pressure–temperature conditions reached in experiments on ferropericlase (red), 2-phases [enstatite (bridgmanite) + ferropericlase] (blue), calcium perovskite CaPv (green), and tantalum carbide TaC (yellow) in different experimental runs.

performed two successful experimental deformation runs on tantalum carbide ($TaC_{0.99}$) and constrained the pressure–volume–temperature equation of state (EOS) (Speziale et al., 2019). The starting material was $TaC_{0.99}$ powder, and the pressure was determined by a thin piece of Au foil (less than 5 µm) using a published EOS (Fei et al., 2007b). In the first run, we started heating when the pressure reached 2 GPa, increased the temperature to 673 K, and measured x-ray diffraction up to a final pressure of 33 GPa along the 673 K isotherm (Fei et al., 2007b). In the second run, we increased the temperature at a pressure of ~2 GPa up to 1073 K, and we collected x-ray diffraction images up to a final pressure of 38 GPa along an isothermal path. The data collected under non- hydrostatic conditions were used to constrain the quasi-hydrostatic high temperature EOS by extracting the hydrostatic unit-cell parameter from the x- ray diffraction data (Speziale et al., 2019). In addition, these data will be used in a future study to determine the strength and activity of the slip systems of $TaC_{0.99}$at simultaneous high pressure and temperature.

5.8 Challenges and solutions

In several experimental runs, the DAC jammed during high-temperature experiments, leading to discrete pressure jumps as opposed to smooth increases of pressure. Because of their brittleness, the ceramic gaskets were not able to buffer these pressure jumps, resulting in the failure of the

diamond anvils. The reason for our difficulties to smoothly increase pressure at very high temperatures could be the expansion of both the piston and the cylinder of the Mao–Bell DAC, leading to increased friction between both parts. However, at moderately high temperatures, up to 1400 K, the differential cooling was effective such that a smooth pressure increase is generally possible. For higher temperature experiments, the indirect piston cooling is still insufficient and needs to be improved in order to reduce the thermal expansion of the piston and thus the friction.

Using the water-cooled vacuum chamber, temperatures up to 1900 K have been reached in the RH-rXRD-DAC, but no pressure increase was possible. Generally, both thermocouples recorded stable temperatures during the experiments, with a reproducible dependence of temperature on power (Figure 5.6).

In a few runs, the difference in temperature reading between the two thermocouples was very large (the maximum difference observed was 400 K). In these cases, higher temperature values were recorded by the thermocouple situated between the graphite sheets. Large differences in temperature reading usually occurred when one of the thermocouples, i.e., the one at the tip of the diamond was placed too far from the culet of the diamond.

5.9 Conclusions

We have presented an improved experimental setup for radial x-ray diffraction measurements based on a graphite-heated Mao–Bell type diamond-anvil cell contained in a water-cooled vacuum chamber. The setup is available for users at the Extreme Conditions Beamline P02.2 at DESY, Hamburg, and allows for reaching temperatures of up to 1900 K at high pressures (Figure 5.7).

Temperature and pressure in the diamond-anvil cell are controlled remotely during the experiment. Several successful experimental studies were performed by using the improved setup on a variety of Earth materials (ferropericlase, calcium perovskite, and a two-phase bridgmanite–ferropericlase mixture) and tantalum carbide in order to show the capabilities of the resistive-heated-radial-x-ray-diffraction-diamond-anvil-cell. A major priority is currently the search for a better gasket material that combines large mechanical strength and high-temperature stability.

ACKNOWLEDGMENTS

This research was supported through the German Science Foundation (Grant Nos. MA4534/3-1 and MA4534/4-1). H.M. acknowledges support from the Bavarian Academy of Sciences. L.M. acknowledges support from the U.S. Department of Energy, National Nuclear Security

Administration, through the Capital- DOE Alliance Center (Grant No. DE-NA0003858) and NSF (Grant Nos. EAR-1344579 and EAR-1654687). S.M. acknowledges support from the Institut Universitaire de France and the program PNP of CNRS/INSU. We acknowledge DESY (Hamburg, Germany), a member of the Helmholtz Association HGF, for the provision of experimental facilities. Part of this research were supported by the Extreme Conditions Science Infrastructure (ECSI) at PETRA III, and we would like to thank K. Glazyrin for assistance in using Beam- line P02.2. Part of the research leading to this result was supported by the project CALIPSO plus under the Grant Agreement No. 730872 from the EU Framework Programme for Research and Innovation HORIZON 2020.

References

Adams, D. J. & Oganov, A. R. (2006). Ab initio molecular dynamics study of CaSi O3 perovskite at P-T conditions of Earth's lower mantle. *Physical Review B - Condensed Matter and Materials Physics* **73**, 1–8.

Caracas, R., Wentzcovitch, R., Price, G. D. & Brodholt, J. (2005). CaSiO3 perovskite at lower mantle pressures. *Geophysical Research Letters* **32**, 1–5.

Conrad, C. P., Behn, M. D. & Silver, P. G. (2007). Global mantle flow and the development of seismic anisotropy: Differences between the oceanic and continental upper mantle. *Journal of Geophysical Research: Solid Earth* **112**, 1–17.

Creasy, N., Long, M. D. & Ford, H. A. (2017). Deformation in the lowermost mantle beneath Australia from observations and models of seismic anisotropy. *Journal of Geophysical Research: Solid Earth* **122**, 5243–5267.

Fei, Y., Ricolleau, A., Frank, M., Mibe, K., Shen, G. & Prakapenka, V. (2007). Toward an internally consistent pressure scale. *Proceedings of the National Academy of Sciences* **104**, 9182–9186.

Funamori, N. & Sato, T. (2008). A cubic boron nitride gasket for diamond-anvil experiments. *Review of Scientific Instruments* **79**, 053903.

Girard, J., Amulule, G., Farla, R., Mohiuddin, A. & Karato, S. (2016). Shear deformation of bridgmanite and magnesiowüstite aggregates at lower mantle conditions. *Science* **351**, 144–147.

Handy, M. R. (1994). Flow laws for rocks containing two non-linear viscous phases: A phenomenological approach. *Journal of Structural Geology* **16**, 287–301.

Hunt, S. A. & Dobson, D. P. (2017). Note: Modified anvil design for improved reliability in DT-Cup experiments. *Review of Scientific Instruments* **88**, 126106.

Immoor, J., Marquardt, H., Miyagi, L., Lin, F., Speziale, S., Merkel, S., Buchen, J., Kurnosov, A. & Liermann, H. P. (2018). Evidence for {100}<011> slip in ferropericlase in Earth's lower mantle from high-pressure/high-temperature experiments. *Earth and Planetary Science Letters*. Elsevier B.V. **489**, 251–257.

Jung, D. Y. & Oganov, A. R. (2005). Ab initio study of the high-pressure behavior of CaSiO3 perovskite. *Physics and Chemistry of Minerals* **32**, 146–153.

Kaercher, P., Miyagi, L., Kanitpanyacharoen, W., Zepeda-Alarcon, E., Wang, Y., De Carlo, F. & Wenk, H.-R. (2016). Two-phase deformation of lower mantle mineral analogs. *Earth and Planetary Science Letters*. Elsevier B.V. **456**, 134–145.

Karato, S. (1981). Rheology of the lower mantle. *Physics of the Earth and Planetary Interiors* **24**, 1–14.

Karato, S. (1988). The role of recrystallization in the preferred orientation of olivine. *Physics of the Earth and Planetary Interiors* **51**, 107–122.

Karato, S. & Wu, P. (1993). Rheology of the Upper Mantle: A Synthesis. *Science* **260**, 771–778.

Karato, S., Zhang, S. & Wenk, H.-R. (1995). Superplasticity in Earth's Lower Mantle: Evidence from Seismic Anisotropy and Rock Physics. *Science* **270**, 458–461.

Kawazoe, T., Nishiyama, N., Nishihara, Y., Irifune, T., Suetsugu, D., Bina, C., Inoue, T., Wiens, D. & Jellinek, M. (2010). Deformation experiment at P-T conditions of the mantle transition zone using D-DIA apparatus. *Physics of the Earth and Planetary Interiors* **183**, 190–195.

Kawazoe, T., Ohuchi, T., Nishihara, Y., Nishiyama, N., Fujino, K. & Irifune, T. (2013). Seismic anisotropy in the mantle transition zone induced by shear deformation of wadsleyite. *Physics of the Earth and Planetary Interiors* **216**, 91–98.

Kohlstedt, D. L. (2007). *Properties of Rocks and Minerals - Constitutive Equations, Rheological Behavior, and Viscosity of Rocks*. *Treatise on Geophysics*. Elsevier B.V.

Komabayashi, T., Hirose, K., Sata, N., Ohishi, Y. & Dubrovinsky, L. S. (2007). Phase transition in CaSiO3 perovskite. *Earth and Planetary Science Letters* **260**, 564–569.

Kunz, M., Caldwell, W. a, Miyagi, L. & Wenk, H.-R. (2007). In situ laser heating and radial synchrotron x-ray diffraction in a diamond anvil cell. *The Review of scientific instruments* **78**, 063907.

Liermann, H.-P., Merkel, S., Miyagi, L., Wenk, H.-R., Shen, G., Cynn, H. & Evans, W. J. (2009). Experimental method for in situ determination of material textures at simultaneous high pressure and high temperature by means of radial diffraction in the diamond anvil cell. *The Review of scientific instruments* **80**, 104501.

Liermann, H. P. *et al.* (2015). The Extreme Conditions Beamline P02.2 and the Extreme Conditions Science Infrastructure at PETRA III. *Journal of synchrotron radiation* **22**, 908–24.

Lin, J.-F., Wenk, H.-R., Voltolini, M., Speziale, S., Shu, J. & Duffy, T. S. (2009). Deformation of lower-mantle ferropericlase (Mg,Fe)O across the electronic spin transition. *Physics and Chemistry of Minerals* **36**, 585–592.

Marquardt, H. & Miyagi, L. (2015). Slab stagnation in the shallow lower mantle linked to an increase in mantle viscosity. *Nature Geoscience* **8**, 311–314.

Marquardt, H., Speziale, S., Reichmann, H. J., Frost, D. J., Schilling, F. R. & Garnero, E. J. (2009). Elastic shear anisotropy of ferropericlase in Earth's lower mantle. *Science* **324**, 224–226.

Merkel, S. (2002). Deformation of polycrystalline MgO at pressures of the lower mantle. *Journal of Geophysical Research* **107**, 2271.

Merkel, S. (2006). X-ray diffraction evaluation of stress in high pressure deformation experiments. *Journal of physics. Condensed matter : an Institute of Physics journal* **18**, S949-62.

Merkel, S., Liermann, H.-P., Miyagi, L. & Wenk, H.-R. (2013). In situ radial X-ray diffraction study of texture and stress during phase transformations in bcc-, fcc- and hcp-iron up to 36GPa and 1000K. *Acta Materialia* **61**, 5144–5151.

Merkel, S., McNamara, A. K., Kubo, A., Speziale, S., Miyagi, L., Meng, Y., Duffy, T. S. & Wenk, H. R. (2007). Deformation of (Mg,Fe)SiO3 post-perovskite and D″ anisotropy. *Science* **316**, 1729–1732.

Merkel, S. & Yagi, T. (2005). X-ray transparent gasket for diamond anvil cell high pressure experiments. *Review of Scientific Instruments* **76**, 046109.

Miyagi, L., Kanitpanyacharoen, W., Raju, S. V., Kaercher, P., Knight, J., MacDowell, A., Wenk, H. R., Williams, Q. & Alarcon, E. Z. (2013). Combined resistive and laser heating technique for in situ radial X-ray diffraction in the diamond anvil cell at high pressure and temperature. *Review of Scientific Instruments* **84**, 025118.

Miyagi, L., Merkel, S., Yagi, T., Sata, N., Ohishi, Y. & Wenk, H. R. (2009). Diamond anvil cell deformation of CaSiO3 perovskite up to 49 GPa. *Physics of the Earth and Planetary Interiors* **174**, 159–164.

Nowacki, A., Walker, A. M., Wookey, J. & Kendall, J. M. (2013). Evaluating post-perovskite as a cause of D" anisotropy in regions of palaeosubduction. *Geophysical Journal International* **192**, 1085–1090.

Romanowicz, B. & Wenk, H. R. (2017). Anisotropy in the deep Earth. *Physics of the Earth and Planetary Interiors*. Elsevier B.V. **269**, 58–90.

Shim, S.-H., Jeanloz, R. & Duffy, T. S. (2002). Tetragonal structure of CaSiO 3 perovskite above 20 GPa. *Geophysical Research Letters* **29**, 19.

Speziale, S., Immoor, J., Ermakov, A., Merkel, S., Marquardt, H. & Liermann, H. P. (2019). The equation of state of TaC0.99 by X-ray diffraction in radial scattering geometry to 32 GPa and 1073 K. *Journal of Applied Physics*. AIP Publishing LLC **126**, 0–12.

Tackley, P. J. (2000). Mantle Convection and Plate Tectonics: Toward an Integrated Physical and Chemical Theory. *Science* **288**, 2002–2007.

Takeda, Y. T. (1998). Flow in rocks modelled as multiphase continua: Application to polymineralic rocks. *Journal of Structural Geology* **20**, 1569–1578.

Thielmann, M., Golabek, G. J. & Marquardt, H. (2020). Ferropericlase Control of Lower Mantle Rheology: Impact of Phase Morphology. *Geochemistry, Geophysics, Geosystems* **21**.

Tommaseo, C. E., Devine, J., Merkel, S., Speziale, S. & Wenk, H. R. (2006). Texture development and elastic stresses in magnesiowustite at high pressure. *Physics and Chemistry of Minerals* **33**, 84–97.

Tsujino, N., Nishihara, Y., Yamazaki, D., Seto, Y., Higo, Y. & Takahashi, E. (2016). Mantle dynamics inferred from the crystallographic preferred orientation of bridgmanite. *Nature* **539**, 81–84.

Uchida, T. *et al.* (2009). Non-cubic crystal symmetry of CaSiO3 perovskite up to 18 GPa and 1600 K. *Earth and Planetary Science Letters* **282**, 268–274.

Wang, Y., Durham, W. B., Getting, I. C. & Weidner, D. J. (2003). The deformation-DIA: A new apparatus for high temperature triaxial deformation to pressures up to 15 GPa. *Review of Scientific Instruments* **74**, 3002–3011.

Wang, Y., Hilairet, N., Nishiyama, N., Yahata, N., Tsuchiya, T., Morard, G. & Fiquet, G. (2013). High-pressure, high-temperature deformation of CaGeO 3 (perovskite)?MgO aggregates: Implications for multiphase rheology of the lower mantle. *Geochemistry, Geophysics, Geosystems* **14**, 3389–3408.

Wenk, H.-R., Lonardelli, I., Merkel, S., Miyagi, L., Pehl, J., Speziale, S. & Tommaseo, C. E. (2006). Deformation textures produced in diamond anvil experiments, analysed in radial diffraction geometry. *Journal of Physics: Condensed Matter* **18**, S933–S947.

Wenk, H. R., Baumgardner, J. R., Lebensohn, R. A. & Tomé, C. N. (2000). A convection model to explain anisotropy of the inner core. *Journal of Geophysical Research: Solid Earth* **105**, 5663–5677.

Yamazaki, D. & Karato, S.-I. (2001a). High-pressure rotational deformation apparatus to 15 GPa. *Review of Scientific Instruments* **72**, 4207.

Yamazaki, D. & Karato, S. (2001b). Some mineral physics constraints on the rheology and geothermal structure of Earth's lower mantle. *American Mineralogist* **86**, 385–391.

Chapter 5
An improved setup for radial diffraction experiments at high pressures and high temperatures in a resistive graphite-heated diamond anvil cell

Chapter 6

Evidence for {100}<011> slip in ferropericlase in Earth's lower mantle from high-pressure/high-temperature experiments

J. IMMOOR[a], H. MARQUARDT[a,*], L. MIYAGI[b], F. LIN[b], S. SPEZIALE[c], S. MERKEL[d], J. BUCHEN[a], A. Kurnosov[a], and H.- P. LIERMANN[e]

[a] *Bayerisches Geoinstitut BGI, University of Bayreuth, 95440 Bayreuth, Germany*
[b] *University of Utah, 115 So. 1460 E., Salt Lake City, UT 84112-0111, USA*
[c] *German Research Center for Geosciences GFZ, 14473 Potsdam, Germany*
[d] *Univ. Lille, CNRS, INRA, ENSCL, UMR 8207 – UMET – Unité Matériaux et Transformations, F- 59000 Lille, France*
[e] *Deutsches Elektronen-Synchrotron (DESY), 22607 Hamburg, Germany*

**Corresponding author.*
E-mail address: Hauke.Marquardt@uni-bayreuth.de (H. Marquardt).

Article history:
Received 24 November 2017
Received in revised form 19 February 2018 Accepted 28 February 2018
Available online 12 March 2018 Editor: J. Brodholt

Keywords:
ferropericlase
rheology
lower mantle
seismic anisotropy
large low shear velocity provinces

This chapter has been published as:
Immoor et al. (2018) EARTH AND PLANETARY SCIENCE LETTERS, **489**, 251 – 257.
https://doi.org/10.1016/j.epsl.2018.02.045

Chapter 6
Evidence for {100}<011> slip in ferropericlase in Earth's lower mantle from high-pressure/high-temperature experiments

Abstract

Seismic anisotropy in Earth's lowermost mantle, resulting from Crystallographic Preferred Orientation (CPO) of elastically anisotropic minerals, is among the most promising observables to map mantle flow patterns. A quantitative interpretation, however, is hampered by the limited understanding of CPO development in lower mantle minerals at simultaneously high pressures and temperatures. Here, we experimentally determine CPO formation in ferropericlase, one of the elastically most anisotropic deep mantle phases, at pressures of the lower mantle and temperatures of up to 1400 K using a novel experimental setup. Our data reveal a significant contribution of slip on {100} to ferropericlase CPO in the deep lower mantle, contradicting previous inferences based on experimental work at lower mantle pressures but room temperature. We use our results along with a geodynamic model to show that deformed ferropericlase produces strong shear wave anisotropy in the lowermost mantle, where horizontally polarized shear waves are faster than vertically polarized shear waves, consistent with seismic observations. We find that ferropericlase alone can produce the observed seismic shear wave splitting in D" in regions of downwelling, which may be further enhanced by post-perovskite. Our model further shows that the interplay between ferropericlase (causing VSH > VSV) and bridgmanite (causing VSV > VSH) CPO can produce a more complex anisotropy patterns as observed in regions of upwelling at the margin of the African Large Low Shear Velocity Province.

6.1 Introduction

Seismic shear wave splitting is a key observable in the D" region at the base of the mantle. Anisotropy is observed both in regions where slabs might impinge on the core - mantle boundary (CMB) (Lay et al., 1998; Garnero, 2004; Panning, 2004) and adjacent to ultra-low velocity zones at the margins of the African Large Low Shear Wave Velocity Province (LLSVP) (Cottaar and Romanowicz, 2013; Lynner and Long, 2014). These seismic observations are among the most promising features to map mantle flow patterns and link them to surface processes, provided that the underlying principles are understood (Romanowicz and Wenk, 2017). It is usually assumed that seismic anisotropy is the expression of Crystallographic Preferred Orientation (CPO) of elastically anisotropic lower mantle minerals as a result of deformation by dislocation creep (Merkel et al., 2007; Miyagi et al., 2010; Nowacki et al., 2011; Romanowicz and Wenk, 2017).

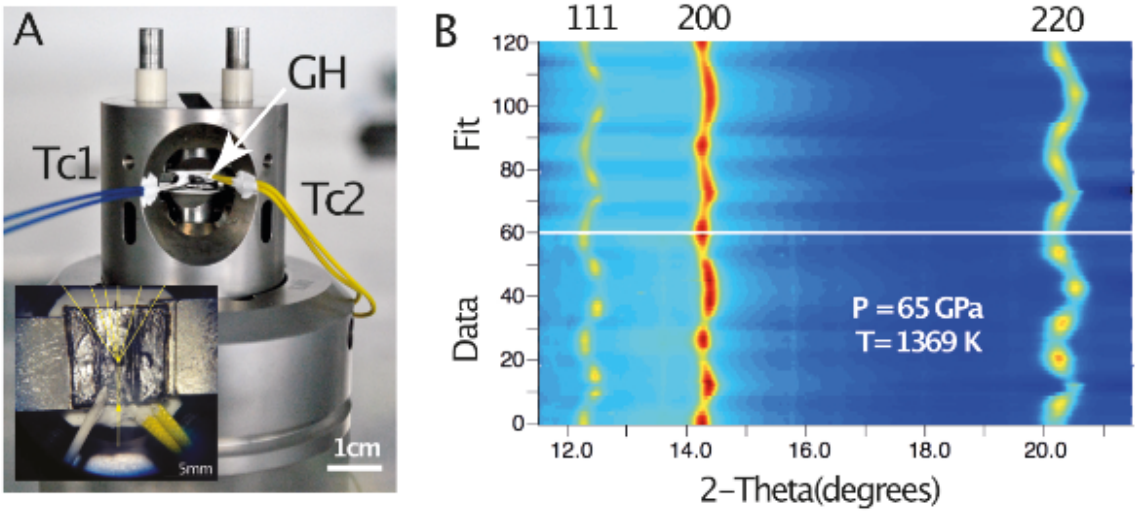

Figure 6.1: Experimental setup and results. (A) Photograph of the resistive-heated DAC used in this study. GH: Graphite-heater; Tc: Thermocouple. Inset shows the lower diamond pressed into the graphite-heater and illustrates the positions of the thermocouples. (B) Diffraction data collected at simultaneous high-P/T (65 GPa, 1369 K, bottom) along with the best-fit model (top). The intensity variations along the unrolled diffraction rings are caused by ferropericlase lattice preferred orientation, the curvature is a measure of elastic lattice strains.

Several past studies combined mineral-physics derived information on the elastic anisotropy as well as the CPO-formation in lower mantle phases with both 2D (Wenk et al., 2006b, 2011) and 3D (Walker et al., 2011; Cottaar et al., 2014) flow field models in attempts to explain lowermost mantle seismic anisotropy in regions where slabs might reach the core–mantle-boundary region, with review articles by Nowacki et al. (2011), Romanowicz and Wenk (2017). Most of these previous works have focused on predicting seismic shear wave splitting that could result from CPO of post-perovskite, the most abundant phase in colder regions of the lowermost mantle. While these studies generally conclude that post-perovskite could explain seismic anisotropy in the D" layer (Miyagi et al., 2010; Walker et al., 2011; Wenk et al., 2011; Nowacki et al., 2013), the results are still inconclusive as they strongly depend on the debated dominant slip systems operating in post-perovskite at lowermost mantle conditions (Walker et al., 2011; Wenk et al., 2011) and may further be affected by transformation textures (Miyagi et al., 2010; Dobson et al., 2013; Walker et al., 2018).

Much less attention has been focused on the possibility of CPO of (Mg,Fe)O ferropericlase, the second most abundant mineral in a pyrolitic lower mantle, as the cause of seismic anisotropy. Ferropericlase is characterized by significant elastic anisotropy that steadily increases with depth and is further enhanced by the iron spin crossover (Lin et al., 2013) in the mid-lower mantle (Marquardt et al., 2009). In the Earth's lowermost mantle, the elastic anisotropy of ferropericlase

is significantly larger as compared to bridgmanite or post-perovskite (Marquardt et al., 2009). This marked elastic anisotropy combined with its rheological weakness (Yamazaki et al., 2009; Marquardt and Miyagi, 2015; Girard et al., 2016) makes ferropericlase a strong candidate phase to generate seismic anisotropy in the lower mantle. The extent to which the intrinsic anisotropy of ferropericlase contributes to seismic anisotropy observed in the lowermost mantle depends on the way ferropericlase crystals orient in the flow field of the mantle. CPO development is controlled by deformation geometry and the relative activities of various available plastic deformation modes. In ferropericlase these appear to be highly sensitive to pressure, temperature (Amodeo et al., 2012) and possibly strain rate (Cordier et al., 2012). Previous work has shown that dislocation creep in (Mg,Fe)O at mantle pressures takes place by slip along <110> directions on either the {100} or the {110} planes, i.e. the slip systems {100}<011> and {110}<1$\bar{1}$0> (Merkel, 2002; Lin et al., 2009, 2017; Cordier et al., 2012; Girard et al., 2012; Marquardt and Miyagi, 2015). The effects of lower mantle pressure and temperature conditions on the relative contribution of these two slip systems is experimentally unconstrained, hampering any reliable modeling of the contribution of ferropericlase to lower mantle seismic anisotropy. In particular, it was suggested that only slip on {100} is consistent with the seismic record in the D″ layer in the lowermost mantle (Karato, 1998), but room-pressure diamond- anvil cell work by synchrotron radial X-ray diffraction (rXRD) on polycrystalline MgO and (Mg,Fe)O concluded that slip on {110} is dominant to pressures of almost 100 GPa (Merkel, 2002; Lin et al., 2009). A more recent rXRD study pointed out the possibility that slip system activities might change with pressure at 300 K (based on a subtle decrease of the observed texture maximum), but could not provide evidence from CPO analysis (Marquardt and Miyagi, 2015). In contrast to diamond-anvil cell work, experimental work on polycrystalline (Mg,Fe)O at high-temperatures, but low pressures, reported {100}<011> to be the dominant slip system (Stretton et al., 2001). Experimental work carried out on MgO single-crystals at temperatures between 1200 and 1473 K proposed a change of slip system activities with pressure, where {110}<1$\bar{1}$0> slip dominates at low pressures, but slip on {100} becomes favorable at pressures beyond the ones achieved in the experiment (Girard et al., 2012). Early theoretical work provided contradictory predictions, indicating either preferred slip on {110} up to at least 100 GPa (Carrez et al., 2009), or a change of dominant slip system with pressure (Karato, 1998). Most recent modeling results of the critical resolved shear stresses (CRSS) in single-crystal MgO suggest dominant {100}<011> slip at pressures above 40–60 GPa both at 300 K and high temperatures (Amodeo et al., 2012, 2016; Cordier et al., 2012). Here, we experimentally determine slip system activities in polycrystalline $(Mg_{0.8}Fe_{0.2})O$ ferropericlase at pressures of the lower mantle and temperatures of up to about 1400 K using rXRD experiments in a resistive-heated DAC. We combine our findings with a

previous geodynamic model to evaluate the contribution of ferropericlase CPO to the observed seismic anisotropy in the lowermost mantle.

6.2 Methods

In this work, we conducted experimental measurements of ferropericlase deformation in the graphite resistive-heated DAC. The experimental approach is outlined in section 6.2.1. The following section 6.2.2 introduces the subsequent modeling that has been performed to (a) extract slip system activities from the experimental data (EVPSC, section 6.2.2.1) and (b) combine these with results of a previous geodynamic model to estimate the possible contribution of ferropericlase to seismic anisotropy in the lower mantle (section 6.2.2.2).

6.2.1 Experimental procedure

6.2.1.1 Samples

The starting materials were finely-ground powders of $(Mg_{0.8}Fe_{0.2})O$ made from stoichiometric mixtures of reagent grade MgO and Fe_2O_3 reacted in a gas-mixing furnace at 1250 °C at an oxygen fugacity 2 log units below the fayalite–magnetite oxygen buffer. The powdered sample was loaded into the pressure chamber of a Mao–Bell-type Diamond-anvil cell (DAC).

6.2.1.2 Graphite-heated diamond-anvil cell (DAC)

Customised Mao–Bell-type DACs were used in our experiments employing diamond anvils with culet sizes of 200 µm and 300 µm (Figure 6.1). X-ray transparent gaskets with a hole of 80 µm diameter made of either amorphous boron epoxy or cubic boron nitride were employed. The gaskets were held in place by a piece of Kapton. A resistive-heater that surrounds the diamond tips was made of two thin flexible graphite layers that are in tight contact with the diamond anvils. To allow X-rays to pass through the heater, a beampath was carved into the graphite sheets (Liermann et al., 2009). Temperature was monitored by two type-R thermocouples (see Figure 6.1). The entire DAC was positioned inside a vacuum chamber designed at the Extreme Condition Beamline (ECB, P02.2) at PETRA III of the Deutsches Elektronensynchrotron (DESY) (Liermann et al., 2015). A vacuum of better then 10^{-4} mbar was maintained during heating to avoid oxidation of the cell and diamonds. The outside of the vacuum chamber was kept at low temperatures by a water-cooling system (Liermann et al., 2015).

Table 6.1: Summary of experimental run conditions.

Name of experimental run	Tc1	Pre-compression	Pressure after heating	Peak pressure
300 K	Ambient (Marquardt and Miyagi, 2015)	–	–	96 GPa
800 K	823 K	5 GPa	4 GPa	67 GPa
1150 K	1136 K	3 GPa	6 GPa	74 GPa
1400 K	1369 K	37 GPa	21 GPa	65 GPa

6.2.1.3 Synchrotron radial X-ray diffraction experiments

The vacuum chamber was mounted on the general purpose station at the ECB and diffraction experiments were conducted using X-ray energies of either 25 or 43 keV. X-rays were focused to about 7.5 (H) by 2 (V) μm^2. Diffraction images were collected from the center of the diamond culet employing a Perkin Elmer Flat Panel 1621 Detector for 30 s. In all experimental runs, the sample was pre-compressed before heating (Table 6.1). Temperature at high-pressures was increased slowly (over several hours) to allow the system to equilibrate and maintain the vacuum. After reaching the target temperature, the temperature was kept constant throughout the experiment while the pressure was increased remotely using a gas-membrane system. The pressure was determined from the unit cell volume of ferropericlase using existing thermal equation of state parameters (compiled in Stixrude and Lithgow-Bertelloni, 2011). We conducted experimental runs at pressures up to 74 GPa at temperatures of about 800 K, 1150 K and 1400 K and collected diffraction images in pressure steps of 1–5 GPa to monitor the evolution of sample texture and strain (Table 6.1).

6.2.1.4 Data reduction

The collected X-ray diffraction images were sliced in steps of 5° and analyzed using the program MAUD (Lutterotti et al., 1997) generally following a previously outlined procedure (Wenk et al., 2014) (Fig. 1). The background was corrected for by using polynomial functions. The "radial diffraction in the DAC" model (Singh et al., 1998) was used to fit lattice strains in ferropericlase. The E-WIMW model which is similar to the WIMV model (Matthies and Vinel, 1982), but allows for incomplete and arbitrary pole figure coverage was employed to fit textures.

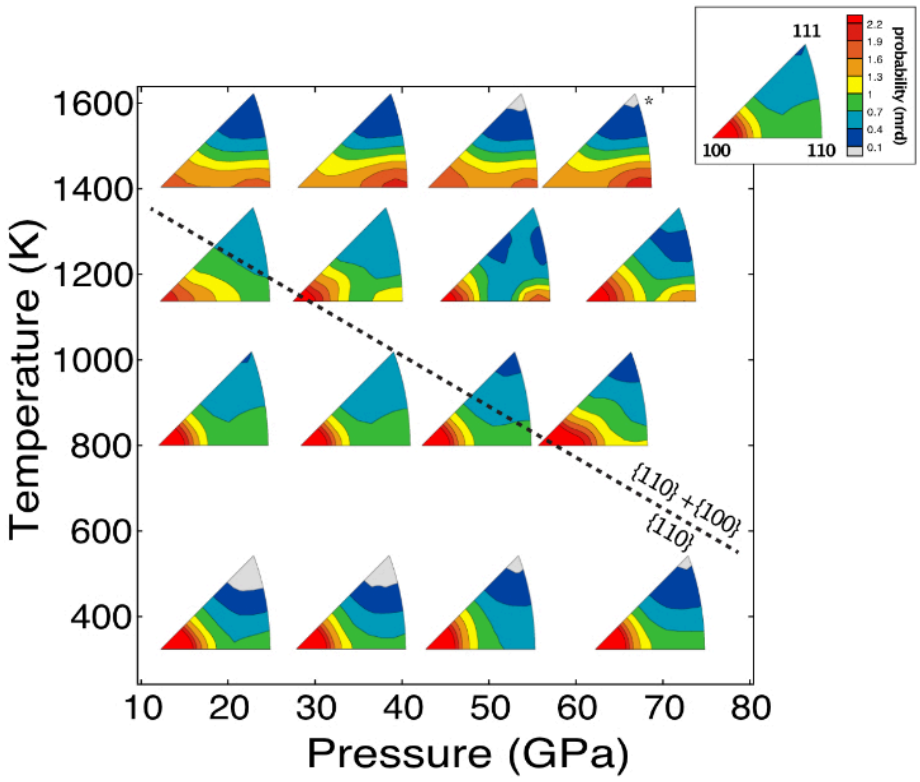

Figure 6.2: Ferropericlase texture evolution observed in our experiments. Data at 300 K are from previous work (Marquardt and Miyagi, 2015) on the same sample material. The lower right corners of the IPFs are placed at the corresponding P/T-conditions. The dashed line is intended for illustration only and highlights the transition from dominant slip on {110} to a regime where slip on 110 and 100 are equally important as judged from the IPF appearances. All textures have been derived from measurements at the center of the sample, except for the point at 65 GPa and 1400 K (denoted with a star) which was collected with the beam approximately 10 µm away from the sample center. The inset shows the axes and color scale of the IPF. (For interpretation of the colors in the figure(s), the reader is referred to the web version of this article.)

6.2.2 Modeling of experimental results and geophysical modeling

6.2.2.1 EVPSC modeling

We used an Elasto-Plastic Self-Consistent code (Wang et al., 2010; Lin et al., 2017) to model the pressure evolution of texture and lattice strains in our experiments. The modeling of the experimental data followed the procedure described before (Merkel et al., 2009) and also applied to periclase (Lin et al., 2017). Modeled lattice strains for the 1400 K experimental run are shown as an example in Fig. S6.1 and compared to the experimental data (Figure 6.2 and Figure 6.3). A second order polynomial was used to represent the pressure dependence of the CRSS (τ) and adjusted to match the experimentally observed lattice strains up to 56 GPa. In the simulation, we

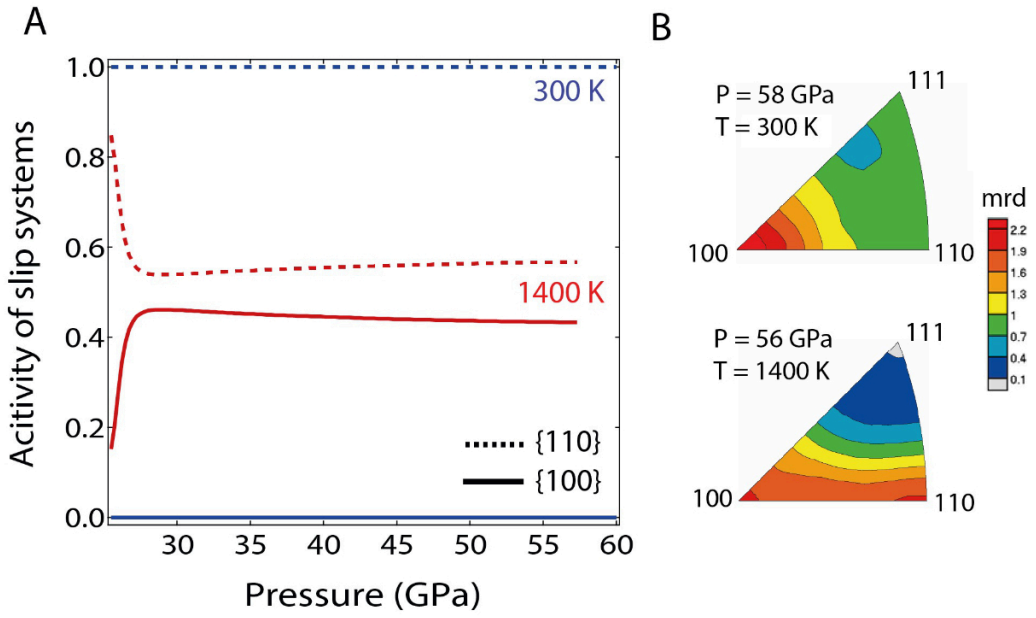

Figure 6.3: Results of EVPSC modeling of the experimental data. (A) Pressure–temperature-dependence of relative slip system activities inferred from modeling the experiments at 1400 K (red) and 300 K (blue). (B) Modeled IPFs of the compression direction at high- P/T. Activity of 100 <011> slip leads to a shift of intensity maximum to 110 in the IPF. Mrd: multiples of random distribution.

excluded data points that have been collected away from the center of the culet. Note that the apparent CRSS are only valid within the experimental pressure range.

No explicit strain hardening was imposed in the simulation due to elevated temperatures. Moreover, it is not possible to separate the relative effects of pressure and strain on the strengthening of the CRSS based on the present experimental data because pressure and strain increase simultaneously during compression. Strain hardening and pressure strengthening are parameterized in EVPSC using the same formalism and have the same effect. Separating the relative contribution of pressure and strain on hardening would require experimental data in which different strains are achieved for the same pressure, which is not possible with current DAC experiment. Here, we hence combined the two effects into the pressure strengthening parameters.

A stress exponent of n 5 was used for all slip systems. We found that increasing or decreasing the value of the stress exponent by 1 or 2 does not significantly change the modeling results. The {111} <110> slip system is given a very high initial CRSS to fully suppress its activity. Different grain-interaction models (affine, secant, tangent) were tested, but resulted in comparable pressure evolutions of lattice strain and texture. The input parameters employed for the modeling of the 1400 K compression run are summarized in Table 6.2.

6.2.2.2 Large-scale modeling

To model large scale seismic anisotropy development we utilized a 2D geodynamic model that has been previously used to predict anisotropy development in a slab subducted along the D″ (McNamara and Zhong, 2005; Merkel et al., 2007; Miyagi et al., 2010). A tracer records strain and temperature history and by coupling this with the VPSC (Lebensohn and Tomé, 1994), we simulated texture development in a slab that is first subducted to the core mantle boundary (CMB), is deformed laterally across the CMB, and then begins to rise away from the CMB. We assumed that the aggregate enters the top of the D″ (~290 km above the CMB) with a random orientation distribution and that only 10 % of total strain accumulated by the strain tracer is accommodated by dislocations. This allows for the additional contribution of diffusion processes (such as climb and creep) which do not generate significant CPO development. In order to show the effect of {100} slip on anisotropy development in the lowermost mantle, we assume a ratio of slip system strengths (CRSS) of 10:1 for slip on {110}<1$\bar{1}$0> and {100}<011>. Slip on {111} is fully suppressed. No hardening was used in the model as work hardening is unlikely to be significant at the low strain rates of the lowermost mantle. Slip on {100}<011> dominates deformation along the streamline with 99 % strain accommodated on {100}<011>. By averaging single-crystal elastic constants of MgO (Karki et al., 1999) over the orientation distribution we calculated the aggregate elastic properties. For averaging of the elastic constants we employed the geometric mean (Matthies and Humbert, 1993) which lies close to the Hill average. Anisotropy development in bridgmanite was also modeled along the streamline in the same manner as was done for ferropericlase. We used previously published CRSS values (Miyagi and Wenk, 2016) and single crystal elastic constants (Wentzcovitch et al., 2004). In this model slip on (001) planes in multiple slip directions accounts for 72 % of strain with the remaining 28 % evenly distributed on (100) and (010) planes.

Table 6.2: Parameters employed for EVPSC modeling of experimental data collected at 1400 K.

Slip system	τ_0 (GPa)	$d\tau/dP$	$d^2\tau/dP^2$ (GPa^{-1})	n
{110}<1$\bar{1}$0>	0.7	0.03	−0.0003	5
{100}<011>	0.9	0.09	−0.0008	5
{111}<1$\bar{1}$0>	50	0	0	5

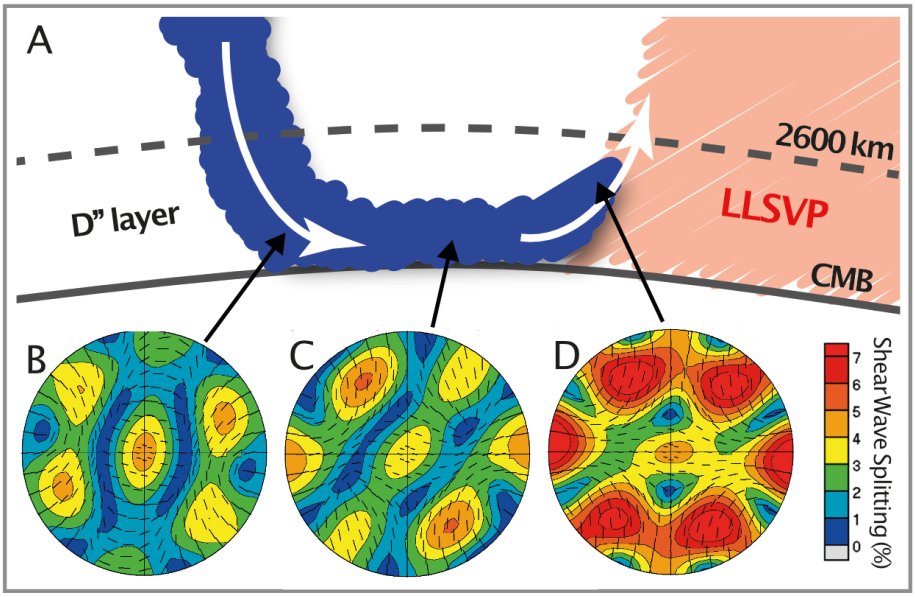

Figure 6.4: Modeled seismic shear wave splitting from ferropericlase at three positions along a slab in the lowermost mantle (supplementary information). (A) Simplified sketch of a subducting slab impinging on the core-mantle-boundary (CMB) and entrained into upwelling at the margin of a Large Low Shear Velocity Province (LLSVP). Stereographic representation of calculated shear wave splitting predicted for ferropericlase where the slab approaches the CMB (B), after moving parallel to the CMB (C), and during upwelling (D). The CMB is horizontal and lines indicate the direction of fast shear wave polarization. The magnitude of predicted shear wave splitting in percent is color-coded. The presented shear wave splitting likely represents a lower bound as, in our calculation, only 10 % of deformation is accommodated by dislocation movement. The corresponding elastic tensors as derived from VPSC are summarized in table S6.1.

6.3 Results and discussion

Texture development represented by inverse pole figures (IPF) of the compression direction as derived from this work and our previous experiments at 300 K (Marquardt and Miyagi, 2015) is summarized in Figure 6.2. Experimental runs at 300 K, 800 K, and 1150 K are characterized by the development of a strong 100 maximum upon initial pressure increase. At experimental temperatures of 300 K and 800 K, texture strength increases when pressure is increased, but the appearance of the IPF is generally unchanged (Figure 6.2), similar to earlier deformation experiments conducted at room temperature on MgO (Merkel, 2002) and (Mg,Fe)O (Tommaseo et al., 2006; Lin et al., 2009; Marquardt and Miyagi, 2015). However, at 800 K we observe a tendency for the maximum to develop a shoulder towards 110 in the IPF. Deformation at higher temperature shows a different behavior. At pressures of about 30–40 GPa at 1150 K, a secondary texture maximum clearly develops at 110. At 1400 K, this maximum is present throughout the entire high-temperature compression in the experiment and gradually strengthens with pressure. According to recent theoretical work (Amodeo et al., 2016) and modeling based on experiments

(Wang et al., 2010; Lin et al., 2017) (Figure S6.3, supplementary information), the secondary maximum at 110 in the IPF is a clear indication for increased activity of {100}<011> slip.

Complementary modeling of both our experimental lattice strains and texture development using a recently developed Elasto-Visco-Plastic Self-Consistent code (EVPSC) allows us to extract slip system activities from our experimental data (Lin et al., 2017) as well as the corresponding absolute values of the slip systems' CRSS by comparing the experimental and simulated textures (Figure S6.2) and lattice strains (Figure S6.1). We note that it is difficult to model complex strain paths acquired prior to stabilization of the heater. For the measured lattice strains at 1400 K there is no data before ~25 GPa. Prior to 25 GPa the sample temperature was increased and the heater took time to stabilize. During this time there are fluctuations in temperature and pressure. This experimental difficulty leads to a complex strain and temperature history before the start of compression at 25 GPa, which cannot be modeled with EVPSC. Therefore, we focus on general trends, particularly the order and relative magnitude of experimental and modeled Q-factors as these are most relevant and most sensitive in determining the absolute CRSS values.

EVPSC modeling to reproduce published high-pressure data at 300 K (Marquardt and Miyagi, 2015) indicates 100 % activity of slip on {110} throughout the entire experimental pressure range (Figure 6.3). However, we find that at 1400 K and high pressures, slip on {110} and {100} contribute about equally to the overall deformation in our experiments, suggesting that slip on {100} becomes favorable with both pressure and temperature in the Earth's mantle.

Even though our conclusion is qualitatively consistent with most recent modeling results on single-crystal MgO (Amodeo et al., 2012; Cordier et al., 2012) , our experimental data are not consistent with a full inversion of the easiest slip plane from {110} to {100} but rather a steady increase of {100} slip system activity. We note that the derived critical resolved shear stresses (CRSS) are difficult to compare directly to numerical models for single crystals. In the theoretical work, the CRSS are derived for single-crystal MgO, whereas the here-derived apparent CRSS are based on experimental data collected on polycrystalline samples. In polycrystalline materials, the strength and relative slip system activities differ from those inferred from the single-crystal CRSS, because they depend on additional effects, such as grain–grain-interactions, grain boundary processes, or back-stresses. This was confirmed by an additional test EVPSC simulation employing the predicted single- crystal CRSS for MgO (Amodeo et al., 2012) that did not reproduce the experimentally derived lattice strains. In particular, if the CRSS of {100} slip is set lower than that of {110} at a given pressure, the lattice strain parameters Q (111) and Q (220) will drop, which is not observed in the experiment.

6.4 Geophysical implications

Based on our findings, we expect a change in the dominant slip system activity to occur at conditions of the mid-lower mantle. Below the depths at which the slip system activity change, strain that builds up inside or in the vicinity of a subducting slab would be mostly accommodated by activity of {100} <011> slip if dislocation creep mechanisms operate. Between the mid- lower mantle and the lowermost mantle, a new type of CPO in ferropericlase would then progressively develop. In parallel, the elastic anisotropy of ferropericlase steadily increases with depth, particularly across the iron spin crossover (Marquardt et al., 2009). These processes can produce a continuous increase of seismic anisotropy of the mantle with depth that, in the lowermost mantle, may reach a threshold strength making it detectable for seismology (Figure 6.4). It is worth noting that recent work indicates the presence of anisotropy about 1000 km above the CMB and well above the D″ layer (de Wit and Trampert, 2015). However, as seismic studies mostly report seismic shear wave splitting in the lowermost mantle (Lay et al., 1998; Garnero, 2004; Panning, 2004; Cottaar and Romanowicz, 2013; Lynner and Long, 2014; Romanowicz and Wenk, 2017), where seismic coverage is good, we restrict the following discussion to this region.

Paralleling previous work (Merkel et al., 2007; Miyagi et al., 2010), we use our results to model texture development in ferropericlase along a geodynamic streamline (Figure 6.4, section 6.22) (McNamara and Zhong, 2005). We then combine the texture information with elasticity data to predict seismic shear wave splitting from deformed ferropericlase in the lower mantle, both in regions where sinking slabs impinge on the core–mantle boundary and in regions of upwellings. Here, the edges of Large Low Shear Velocity Provinces (LLSVP) seem of particular interest as previous work concluded that deformation is localized in these regions leading to detectable seismic anisotropy (Cottaar and Romanowicz, 2013; Lynner and Long, 2014; Garnero et al., 2016).

Our model shows that deformation of ferropericlase with dominant slip on {100} will produce a strong VSH > VSV shear wave splitting for seismic waves propagating parallel to the CMB, i.e. horizontally polarized shear waves VSH travel faster than vertically polarized shear waves VSV, even if only 10 % of the total deformation is accommodated by dislocation glide. Interestingly, the VSH > VSV anisotropy produced by ferropericlase CPO is maintained along the entire geodynamic streamline, likely as a result of the high crystallographic symmetry of ferropericlase, and reaches a maximum in regions of upwellings (Figure 6.4 D). Based on our modeling, ~20 % of ferropericlase alone, as expected for a typical lower mantle, would be sufficient to produce 1–2 % of seismic shear wave splitting as typically observed in the lowermost mantle (Lay et al., 1998; Garnero, 2004; Panning, 2004; Cottaar and Romanowicz, 2013; Lynner and Long, 2014; Romanowicz and Wenk, 2017) (Figure 6.4), at least for seismic ray paths along the slab. The

predicted anisotropy was calculated for pure MgO for which complete datasets of elastic constants at high P / T are available unlike ferropericlase. As ferropericlase is elastically more anisotropic as compared to MgO (Marquardt et al., 2009), the predicted shear wave splitting likely represents a lower bound.

In addition to ferropericlase, post-perovskite and/or bridgmanite will contribute to measured seismic shear wave splitting. The deformation of post-perovskite, the dominant phase in cold regions of D", might also result in a VSH > VSV anisotropy pattern (Miyagi et al., 2010; Wu et al., 2017), thereby enhancing the contribution from ferropericlase. However, slip system activities in post-perovskite, including possible transformation textures, are still debated (Merkel et al., 2007; Miyagi et al., 2010; Dobson et al., 2013; Goryaeva et al., 2015; Wu et al., 2017) particularly as the experimental information on the high temperature behavior of post perovskite is extremely limited (Wu et al., 2017).

In hotter regions of the D", such as upwellings, post-perovskite might become unstable due to the positive Clapeyron slope of the bridgmanite to post-perovskite phase transition (Murakami et al., 2004), stabilizing bridgmanite at high temperatures. Deformation of bridgmanite will result in VSV > VSH shear wave splitting in regions of upwellings (Figure S6.3) (Tsujino et al., 2016). Our results show that ferropericlase, instead, produces a strong VSH > VSV shear wave splitting in these regions (Figure 6.4 D).

The magnitude of VSH > VSV seismic shear wave splitting predicted from our model for ferropericlase, however, strongly depends on the raypath of the probing seismic wave. The strongest shear wave splitting (up to 7 %) is observed for seismic waves propagating along the direction of slab movement, whereas other directions show little shear wave splitting (Figure 6.4 D). Moreover, for seismic waves that travel with some angle to the CMB, the pattern is more complicated and ferropericlase could produce a VSV > VSH anisotropy, particularly in regions of upwelling.

Our model therefore predicts the character and magnitude of observed shear wave splitting, resulting from a combination of ferropericlase and bridgmanite CPO in upwellings to be highly sensitive to the probing seismic raypath. The observed complicated shear wave anisotropy distribution in the vicinity of the African Large Low Shear Velocity Province may thus be explained by competing anisotropy contributions from ferropericlase and bridgmanite CPO (Cottaar and Romanowicz, 2013; Lynner and Long, 2014; Romanowicz and Wenk, 2017).

The actual contributions of these two phases to D″ anisotropy will ultimately depend on the deformation behavior of a multi- phase-assemblage at conditions of the lowermost mantle. Limited information from rotational Drickamer apparatus (Girard et al., 2016), diamond-anvil cell work at 300 K (Miyagi and Wenk, 2016), and experiments and modeling in analogue systems (Wang et al., 2013; Kaercher et al., 2016) indicate that strain heterogeneity on the grain scale

may play a significant role for the rheological behavior of multiphase systems and the resulting CPO pattern. Possible changes in strain partitioning caused by temperature variations or strain (rate) may further complicate the resulting anisotropy pattern. Besides possible differences in CPO development in multiphase mixtures as compared to single-phase systems, a solid state shape preferred orientation (SPO) of ferropericlase and post-perovskite or bridgmanite may also contribute to generating seismic anisotropy. This would require SPO to develop and a large elastic contrast between the two phases. Also, aligned melt pockets could in principle contribute to the observed seismic anisotropy (Kendall and Silver, 1996). Despite these open questions, our results provide direct experimental proof for {100}<110> slip in ferropericlase at conditions of the lower mantle and demonstrate that ferropericlase may play an important role in generating seismic shear wave splitting in the lowermost mantle.

Acknowledgements

This research was supported through the projects "GeoMaX" funded under the Emmy-Noether Program of the German Science Foundation (MA4534/3-1) as well as grant MA4534/4-1. HM acknowledges support from the Bavarian Academy of Sciences. LM acknowledges support from CDAC and NSF (EAR-0337006 and EAR-1654687). SM acknowledges support from the Institut Universitaire de France and the program PNP of CNRS/INSU. We thank D. Frost for providing the ferropericlase powders and Konstantin Glazyrin for assistance at the ECB. We further acknowledge technical assistance by A. Ehnes and I. Schwark (Infrastructure for Extreme Conditions Research ECSI, DESY).

Supplementary Material

See page 86 for supplementary Figures and Tables.

References

Amodeo, J., Carrez, P. & Cordier, P. (2012). Modelling the effect of pressure on the critical shear stress of MgO single crystals. *Philosophical Magazine*. Taylor & Francis Group **92**, 1523–1541.

Amodeo, J., Dancette, S. & Delannay, L. (2016). Atomistically-informed crystal plasticity in MgO polycrystals under pressure. *International Journal of Plasticity*. Elsevier Ltd **82**, 177–191.

Carrez, P., Ferré, D. & Cordier, P. (2009). Peierls-Nabarro modelling of dislocations in MgO from ambient pressure to 100 GPa. *Modelling and Simulation in Materials Science and Engineering* **17**.

Cordier, P., Amodeo, J. & Carrez, P. (2012). Modelling the rheology of MgO under Earth's mantle pressure, temperature and strain rates. *Nature*. Nature Publishing Group **481**, 177–180.

Cottaar, S., Li, M., McNamara, A. K., Romanowicz, B. & Wenk, H. R. (2014). Synthetic seismic anisotropy models within a slab impinging on the core-mantle boundary. *Geophysical Journal International* **199**.

Cottaar, S. & Romanowicz, B. (2013). Observations of changing anisotropy across the southern margin of the African LLSVP. *Geophysical Journal International* **195**, 1184–1195.

de Wit, R. W. L. & Trampert, J. (2015). Robust constraints on average radial lower mantle anisotropy and consequences for composition and texture. *Earth and Planetary Science Letters* **429**.

Dobson, D. P., Miyajima, N., Nestola, F., Alvaro, M., Casati, N., Liebske, C., Wood, I. G. & Walker, A. M. (2013). Strong inheritance of texture between perovskite and post-perovskite in the D″ layer. *Nature Geoscience* **6**.

Garnero, E. J. (2004). Variable Azimuthal Anisotropy in Earth's Lowermost Mantle. *Science* **306**, 259–261.

Garnero, E. J., McNamara, A. K. & Shim, S.-H. (2016). Continent-sized anomalous zones with low seismic velocity at the base of Earth's mantle. *Nature Geoscience*. Nature Publishing Group **9**, 481–489.

Girard, J., Amulule, G., Farla, R., Mohiuddin, A. & Karato, S. (2016). Shear deformation of bridgmanite and magnesiowüstite aggregates at lower mantle conditions. *Science* **351**, 144–147.

Girard, J., Chen, J. & Raterron, P. (2012). Deformation of periclase single crystals at high pressure and temperature: Quantification of the effect of pressure on slip-system activities. *Journal of Applied Physics*.

Goryaeva, A. M., Carrez, P. & Cordier, P. (2015). Modeling defects and plasticity in MgSiO3 post-perovskite: Part 2—screw and edge [100] dislocations. *Physics and Chemistry of Minerals* **42**.

Kaercher, P., Miyagi, L., Kanitpanyacharoen, W., Zepeda-Alarcon, E., Wang, Y., De Carlo, F. & Wenk, H.-R. (2016). Two-phase deformation of lower mantle mineral analogs. *Earth and Planetary Science Letters*. Elsevier B.V. **456**, 134–145.

Karato, S. (1998). Some remarks on the origin of seismic anisotropy in the D" layer. *Earth Planets and Space* 1019–1028.

Karki, B. B., Wentzcovitch, R. M., De Gironcoli, S. & Baroni, S. (1999). First-principles determination of elastic anisotropy and wave velocities of MgO at lower mantle conditions. *Science* **286**.

Kendall, J.-M. & Silver, P. G. (1996). Constraints from seismic anisotropy on the nature of the lowermost mantle. *Nature*, 409–412.

Lay, T., Williams, Q. & Garnero, E. J. (1998). The core–mantle boundary layer and deep Earth dynamics. *Nature* **392**, 461–468.

Lebensohn, R. A. & Tomé, C. N. (1994). A self-consistent viscoplastic model: prediction of rolling textures of anisotropic polycrystals. *Materials Science and Engineering A* **175**, 71–82.

Liermann, H.-P., Merkel, S., Miyagi, L., Wenk, H.-R., Shen, G., Cynn, H. & Evans, W. J. (2009). Experimental method for in situ determination of material textures at simultaneous high pressure and high temperature by means of radial diffraction in the diamond anvil cell. *The Review of scientific instruments* **80**, 104501.

Liermann, H. P. *et al.* (2015). The Extreme Conditions Beamline P02.2 and the Extreme Conditions Science Infrastructure at PETRA III. *Journal of synchrotron radiation* **22**, 908–24.

Lin, F., Hilairet, N., Raterron, P., Addad, A., Immoor, J., Marquardt, H., Tomé, C. N., Miyagi, L. & Merkel, S. (2017). Elasto-viscoplastic self consistent modeling of the ambient temperature plastic behavior of periclase deformed up to 5.4 GPa. *Journal of Applied Physics* **122**.

Lin, F., Speziale, S., Mao, Z., Marquardt, H. & Science, G. (2013). Effects of the electronic spin transitions of iron in lower--mantle minerals: implications for deep--mantle geophysics and geochemistry. 244–275.

Lin, J.-F., Wenk, H.-R., Voltolini, M., Speziale, S., Shu, J. & Duffy, T. S. (2009). Deformation of lower-mantle ferropericlase (Mg,Fe)O across the electronic spin transition. *Physics and Chemistry of Minerals* **36**, 585–592.

Lutterotti, L., Matthies, S., Wenk, H.-R., Schultz, A. S. & Richardson, J. W. (1997). Combined texture and structure analysis of deformed limestone from time-of-flight neutron diffraction spectra. *Journal of Applied Physics*. AIP Publishing **81**, 594.

Lynner, C. & Long, M. D. (2014). Lowermost mantle anisotropy and deformation along the boundary of the African LLSVP. *Geophysical Research Letters* **41**, 3447–3454.

Marquardt, H. & Miyagi, L. (2015). Slab stagnation in the shallow lower mantle linked to an increase in mantle viscosity. *Nature Geoscience* **8**, 311–314.

Marquardt, H., Speziale, S., Reichmann, H. J., Frost, D. J., Schilling, F. R. & Garnero, E. J. (2009). Elastic shear anisotropy of ferropericlase in Earth's lower mantle. *Science* **324**, 224–226.

Matthies, S. & Humbert, M. (1993). The Realization of the Concept of a Geometric Mean for Calculating Physical Constants of Polycrystalline Materials. *physica status solidi (b)* **177**.

Matthies, S. & Vinel, G. W. (1982). An Example Demonstrating a New Reproduction Method of the ODF of Texturized Samples from Reduced Pole Figures. **115**, 115–120.

McNamara, A. K. & Zhong, S. (2005). Thermochemical structures beneath Africa and the Pacific Ocean. *Nature* **437**.

Merkel, S. (2002). Deformation of polycrystalline MgO at pressures of the lower mantle. *Journal of Geophysical Research* **107**, 2271.

Merkel, S., McNamara, A. K., Kubo, A., Speziale, S., Miyagi, L., Meng, Y., Duffy, T. S. & Wenk, H. R. (2007). Deformation of (Mg,Fe)SiO3 post-perovskite and D″ anisotropy. *Science* **316**, 1729–1732.

Merkel, S., Tomé, C. & Wenk, H.-R. (2009). Modeling analysis of the influence of plasticity on high pressure deformation of hcp-Co. *Physical Review B* **79**, 064110.

Miyagi, L., Kanitpanyacharoen, W., Kaercher, P., Lee, K. K. M. & Wenk, H. R. (2010). Slip systems in MgSiO3 post-perovskite: Implications for D″ anisotropy. *Science*.

Miyagi, L. & Wenk, H.-R. (2016). Texture development and slip systems in bridgmanite and bridgmanite + ferropericlase aggregates. *Physics and Chemistry of Minerals*. Springer Berlin Heidelberg.

Murakami, M., Hirose, K., Kawamura, K., Sata, N. & Ohishi, Y. (2004). Post-Perovskite Phase Transition in MgSiO3. *Science* **304**.

Nowacki, A., Walker, A. M., Wookey, J. & Kendall, J. M. (2013). Evaluating post-perovskite as a cause of D" anisotropy in regions of palaeosubduction. *Geophysical Journal International* **192**, 1085–1090.

Nowacki, A., Wookey, J. & Kendall, J. M. (2011). New advances in using seismic anisotropy, mineral physics and geodynamics to understand deformation in the lowermost mantle. *Journal of Geodynamics* **52**, 205–228.

Panning, M. (2004). Inferences on Flow at the Base of Earth's Mantle Based on Seismic Anisotropy. *Science* **303**, 351–353.

Romanowicz, B. & Wenk, H. R. (2017). Anisotropy in the deep Earth. *Physics of the Earth and Planetary Interiors*. Elsevier B.V. **269**, 58–90.

Singh, A. K., Balasingh, C., Mao, H. K., Hemley, R. J. & Shu, J. (1998). Analysis of lattice strains measured under nonhydrostatic pressure. *Journal of Applied Physics* **83**, 7567–7575.

Stixrude, L. & Lithgow-Bertelloni, C. (2011). Thermodynamics of mantle minerals - II. Phase equilibria. *Geophysical Journal International* **184**.

Stretton, I., Heidelbach, F., Mackwell, S. & Langenhorst, F. (2001). Dislocation creep of magnesiowüstite (Mg0.8Fe0.2O). *Earth and Planetary Science Letters* **194**, 229–240.

Tommaseo, C. E., Devine, J., Merkel, S., Speziale, S. & Wenk, H. R. (2006). Texture development and elastic stresses in magnesiowustite at high pressure. *Physics and Chemistry of Minerals* **33**, 84–97.

Tsujino, N., Nishihara, Y., Yamazaki, D., Seto, Y., Higo, Y. & Takahashi, E. (2016). Mantle dynamics inferred from the crystallographic preferred orientation of bridgmanite. *Nature* **539**, 81–84.

Walker, A. M., Dobson, D. P., Wookey, J., Nowacki, A. & Forte, A. M. (2018). The anisotropic signal of topotaxy during phase transitions in D″. *Physics of the Earth and Planetary Interiors* **276**.

Walker, A. M., Forte, A. M., Wookey, J., Nowacki, A. & Kendall, J. M. (2011). Elastic anisotropy of D″ predicted from global models of mantle flow. *Geochemistry, Geophysics, Geosystems* **12**.

Wang, H., Wu, P. D., Tomé, C. N. & Huang, Y. (2010). A finite strain elastic-viscoplastic self-consistent model for polycrystalline materials. *Journal of the Mechanics and Physics of Solids* **58**, 594–612.

Wang, Y., Hilairet, N., Nishiyama, N., Yahata, N., Tsuchiya, T., Morard, G. & Fiquet, G. (2013). High-pressure, high-temperature deformation of CaGeO 3 (perovskite)?MgO aggregates: Implications for multiphase rheology of the lower mantle. *Geochemistry, Geophysics, Geosystems* **14**, 3389–3408.

Wenk, H.-R., Lutterotti, L., Kaercher, P., Kanitpanyacharoen, W., Miyagi, L. & Vasin, R. (2014). Rietveld texture analysis from synchrotron diffraction images. II. Complex multiphase materials and diamond anvil cell experiments. *Powder Diffraction* **29**, 220–232.

Wenk, H. R., Cottaar, S., Tomé, C. N., McNamara, A. & Romanowicz, B. (2011). Deformation in the lowermost mantle: From polycrystal plasticity to seismic anisotropy. *Earth and Planetary Science Letters*. Elsevier B.V. **306**, 33–45.

Wenk, H. R., Speziale, S., McNamara, A. K. & Garnero, E. J. (2006). Modeling lower mantle anisotropy development in a subducting slab. *Earth and Planetary Science Letters* **245**, 302–314.

Wentzcovitch, R. M., Karki, B. B., Cococcioni, M. & De Gironcoli, S. (2004). Thermoelastic Properties of MgSiO3-Perovskite: Insights on the Nature of the Earth's Lower Mantle. *Physical Review Letters* **92**.

Wu, X., Lin, J. F., Kaercher, P., Mao, Z., Liu, J., Wenk, H. R. & Prakapenka, V. B. (2017). Seismic anisotropy of the D″ layer induced by (001) deformation of post-perovskite. *Nature Communications* **8**.

Yamazaki, D., Yoshino, T., Matsuzaki, T., Katsura, T. & Yoneda, A. (2009). Texture of (Mg,Fe)SiO3 perovskite and ferropericlase aggregate: Implications for rheology of the lower mantle. *Physics of the Earth and Planetary Interiors* **174**.

Chapter 6
Evidence for {100}<011> slip in ferropericlase in Earth's lower mantle from high-pressure/high-temperature experiments

Supplementary Material

Supplementary Figures and Tables

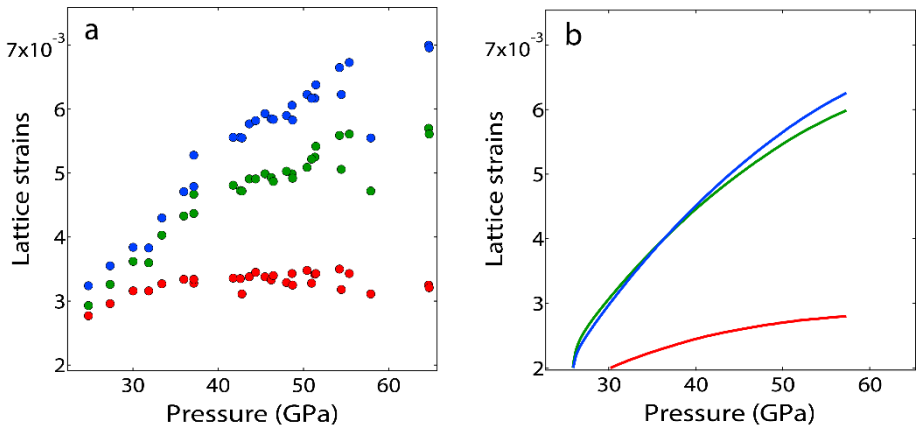

Figure S6.1: Measured (a) and modeled (b) lattice strains (secant model, 20% axial strain at the highest pressure) as a function of pressure: Q111: blue; Q220: green; Q200: red.

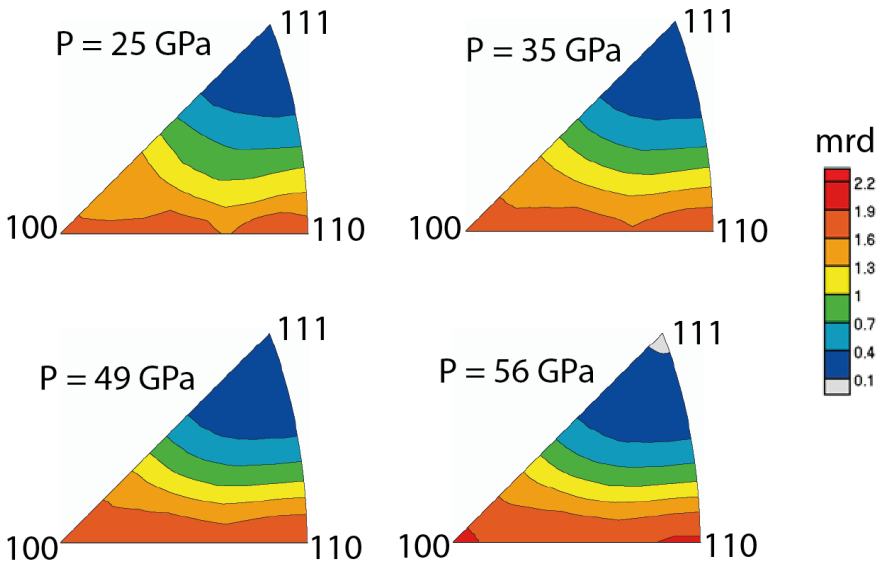

Figure S6.2: Modeled texture evolution at 1400 K with simultaneous activity of slip on {110} and {100} (secant model, 20% total strain). The starting texture at 25 GPa is that of the experiment. Note that as result of discretizing the orientation distribution function of the experimental starting texture to generate an input set of orientations for EVPSC, the IPF of the starting texture (P = 25 GPa) shows small differences with respect to the one shown in Figure 6.2.

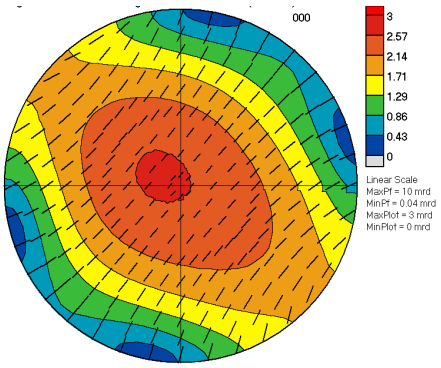

Figure S6.3: Modeled seismic shear wave splitting from bridgmanite in regions of upwelling corresponding to position "D" in Fig. 4. The CMB is horizontal and lines indicate the direction of fast shear wave polarization. The magnitude of predicted shear wave splitting is color-coded.

Table S6.1: Elastic Stiffness Tensors derived using the VPSC code and used for Figure 6.4 B-D, all numbers in GPa.

Figure 4B					
906.0	385.4	393.6	0.5	0.6	7.6
385.4	928.0	371.7	0.0	-0.4	-2.5
393.6	371.7	919.7	-0.5	-0.2	-5.1
0.5	0.0	-0.5	266.0	-5.2	-0.4
0.6	-0.4	-0.2	-5.2	288.8	0.6
7.6	-2.5	-5.1	-0.4	0.6	280.1
Figure 4C					
929.1	364.9	390.9	0.2	0.9	9.8
364.9	946.4	373.6	0.2	-0.7	-4.1
390.9	373.6	920.4	-0.5	-0.2	-5.7
0.2	0.2	-0.5	268.2	-6.0	-0.7
0.9	-0.7	-0.2	-6.0	285.6	0.3
9.8	-4.1	-5.7	-0.7	0.3	260.1
Figure 4D					
946.6	344.9	393.4	-0.2	1.3	-7.0
344.9	969.8	370.2	0.9	-0.6	11.2
393.4	370.2	921.4	-0.7	-0.7	-4.2
-0.2	0.9	-0.7	265.4	-4.3	-0.5
1.3	-0.6	-0.7	-4.3	287.6	-0.2
-7.0	11.2	-4.2	-0.5	-0.2	243.3

Chapter 6
Evidence for {100}<011> slip in ferropericlase in Earth's lower mantle from high-pressure/high-temperature experiments

Chapter 7

Weak Cubic $CaSiO_3$ Perovskite in Earth's Mantle

J. IMMOOR[1], L. MIYAGI[2], H.- P. LIERMANN[3], S. SPEZIALE[4], K. SCHULZE, J. BUCHEN[5], A. KURNOSOV[1], H. MARQUARDT[7,*]

[1]Bayerisches Geoinstitut BGI, University of Bayreuth, 95440 Bayreuth, Germany; [2]University of Utah, 115 So. 1460 E., Salt Lake City, Utah 84112-0111, USA; [3]Photon Sciences, Deutsches Elektronen-Synchrotron (DESY), 22607 Hamburg, Germany; [4]German Research Center for Geosciences GFZ, 14473 Potsdam, Germany; [5]Materials Physics and Technology at Extreme Conditions, Laboratory of Crystallography, University of Bayreuth, 95440 Bayreuth, Germany; [6]Seismological Laboratory, California Institute of Technology, Pasadena, California, USA; [7]University of Oxford, Department of Earth Sciences, Oxford, OX1 3AN, United Kingdom
**Correspondence to: Hauke.Marquardt@earth.ox.ac.uk*

This chapter has been resubmitted after revision on December10th, 2021 and is currently under review to:

Nature

The published version can be found under: https://doi.org/10.1038/s41586-021-04378-2

Cubic $CaSiO_3$ perovskite is a major phase in subducted oceanic crust, where it forms at a depth of about 550 km from majoritic garnet (Irifune and Klemme, 2007; Hirose et al., 2017). We measured the plastic strength of cubic $CaSiO_3$ perovskite at pressure and temperature conditions typical for a subducting slab up to a depth of about 1200 km. Contrary to tetragonal $CaSiO_3$ previously investigated at room temperature (Shieh et al., 2004; Miyagi et al., 2009), we find that cubic $CaSiO_3$ perovskite is a comparably weak phase at temperatures of the lower mantle. We find its viscosity to be substantially lower as compared to bridgmanite and ferropericlase, possibly making cubic $CaSiO_3$ perovskite the weakest lower mantle phase. Our findings suggest that cubic $CaSiO_3$ perovskite will govern the dynamics of subducting slabs. It further provides a mechanism to separate subducted oceanic crust from the underlying mantle. Depending on the depth of the separation,

basaltic crust could accumulate at the boundary between the upper and lower mantle, where cubic $CaSiO_3$ perovskite may contribute to the seismically observed regions of low shear wave velocities in the uppermost lower mantle (Ballmer et al., 2015; Gréaux et al., 2019), or sink to the core-mantle boundary and explain the seismic anomalies associated with Large Low Shear Velocity Provinces LLSVPs beneath Africa and the Pacific (Garnero et al., 2016; Thomson et al., 2019; Jones et al., 2020).

$CaSiO_3$ perovskite is expected to be the third most abundant phase in Earth's transition zone and lower mantle, where it may account for up to 25 Vol.% of subducted basaltic crust and up to 10 Vol.% of a pyrolitic mantle (Irifune and Klemme, 2007; Hirose et al., 2017). Direct evidence for its existence has recently been reported from analysis of inclusions in super-deep diamonds (Nestola et al., 2018). At room temperature (*T*) and high pressure (*P*), $CaSiO_3$ perovskite has a tetragonal crystal structure, but undergoes a phase transition to a cubic structure with increasing temperature, stabilizing the cubic phase along a typical mantle geotherm (Komabayashi et al., 2007; Sun et al., 2016; Gréaux et al., 2019; Thomson et al., 2019). It has been inferred that the elastic properties of cubic $CaSiO_3$ perovskite might explain regions of reduced shear wave velocities in the uppermost lower mantle (Gréaux et al., 2019) as well as some of the unique seismic properties of the Large Low Shear Velocity Provinces (LLSVP) observed by seismic tomography in the deep lower mantle (Garnero et al., 2016; Thomson et al., 2019; Jones et al., 2020).

While recent works succeeded to measure elastic wave velocities of cubic $CaSiO_3$ perovskite at high-pressure/-temperature (Gréaux et al., 2019; Thomson et al., 2019), experimental information on its rheology is absent. Previous studies of the deformation behavior of $CaSiO_3$ are limited to its tetragonal polymorph at room *T* (refs. Shieh et al., 2004; Miyagi et al., 2009) due to experimental difficulties preventing access to mantle-like *P-T*-conditions. These works suggest that $CaSiO_3$ perovskite is characterized by a plastic strength, exceeding that of $MgSiO_3$ bridgmanite, the dominant phase in Earth's lower mantle. Early computational work, however, predicted that the lattice friction, i.e. the Peierls stress, of the <110> $\{1\bar{1}0\}$ slip system in cubic $CaSiO_3$ perovskite is almost zero (Ferré et al., 2009b), which appears incompatible with a very large plastic strength. Theoretical work further suggested that the Peierls stress increases with structural distortions in perovskite-structured materials (Ferré et al., 2009a). The deformation behavior of cubic $CaSiO_3$ perovskite might thus markedly differ from that of its tetragonal counterpart.

Here, we synthesized and deformed cubic $CaSiO_3$ perovskite at 1150(±50) K (Figure 7.1) in a recently developed high-pressure/-temperature apparatus (Immoor et al., 2020) using synchrotron-based radial x-ray diffraction at the Extreme Conditions Beamline, P02.2, at PETRA III, DESY, Hamburg, Germany. High-pressure lattice strains, *Q(hkl)*, were extracted from the

recorded diffraction images by fitting the experimental observations using the program MAUD (See Methods) where *hkl* refers to the Miller indices of the respective lattice planes. The deviatoric stress *t* supported by the sample was calculated from the average of measured lattice strains using the identity $t = 6 \cdot <Q(hkl)> \cdot G$, where the high-pressure shear modulus, *G*, at 1150 K was taken from ref. (Thomson et al., 2019). Texture development was observed in $CaSiO_3$ perovskite throughout the experiment. The observation of texture development throughout the experiment, as well as plasticity modelling, shows that plastic deformation occurred in the sample (Extended Data Figure 7.3, 7.4) and measured stresses can thus be treated as approximations for the sample's plastic strength (Merkel, 2002). The observed texture strength in our high-temperature experiments is higher than in previous experiments at room temperature (Miyagi et al., 2009), a result of the sample's lower strength.

In Figure 7.2, we compare the here-derived high-temperature strength of cubic $CaSiO_3$ perovskite to previously derived values for (Mg,Fe)O ferropericlase (Immoor et al., 2018) and bridgmanite (Girard et al., 2016; Couper et al., 2020), as well as to reported strengths at room temperature (Merkel et al., 2003; Miyagi et al., 2009; Marquardt and Miyagi, 2015). We note that almost all shown values have been determined by radial x-ray diffraction in the diamond-anvil cell, permitting a direct comparison. Strikingly, cubic $CaSiO_3$ perovskite is characterized by a high-temperature plastic strength that is substantially lower than that reported for bridgmanite and even ferropericlase, which has previously been regarded as the weakest major lower mantle phase (Yamazaki and Karato, 2001b; Marquardt and Miyagi, 2015; Girard et al., 2016; Thielmann et al., 2020), only possibly rivalled by post-perovskite below ~2500 km depth (Goryaeva et al., 2015). It is striking that the strength of $CaSiO_3$ measured here at 1150 K is substantially lower than the strength of bridgmanite previously derived at 2750 K (at 27.5 GPa).

A particularly interesting observation is the large strength contrast between tetragonal $CaSiO_3$ measured at 295 K (Figure 7.2 a) and cubic $CaSiO_3$ perovskite at 1150 K (Figure 7.2 b). While strength is expected to decrease with temperature, the here-observed decrease is much larger than expected from a rise in temperature alone as evident by comparison to ferropericlase and bridgmanite (Figure 7.2). It appears likely that the tetragonal lattice distortion experienced by $CaSiO_3$ perovskite upon temperature decrease leads to an additional increase in strength. This observation is qualitatively consistent with computational work predicting Peierls stresses to increase with lattice distortions in perovskite-structured materials (Ferré et al., 2009a).

We use the here-derived strength values together with the previous results shown in Figure 7.2 to estimate the viscosity contrast between cubic $CaSiO_3$ perovskite, bridgmanite and ferropericlase in the lower mantle. While our measurements have been performed at pressure and temperature conditions typical for the slab's interior at shallow lower-mantle conditions, a major difference between our experiments and deformation in Earth's mantle is the strain rate and the

magnitude of stress. Assuming that the observed rheological behavior is governed by a dislocation-dominated process as expected for high strain rates in both our experiments and subducted slabs in Earth's mantle, it can be described by

$\dot{\varepsilon} = A \cdot \sigma^n$, where $\dot{\varepsilon}$ is the strain rate, σ is stress, n is the stress exponent, and A is a pre-factor.

We used the identity above, together with the definition of viscosity $\eta = \sigma/2\dot{\varepsilon}$, to calculate viscosity ratios between the major lower mantle phases bridgmanite, ferropericlase, and $CaSiO_3$ perovskite using the strength values in Figure 7.2 b. Initially, we assumed that the strain rates in all experiments were the same (10^{-4} s^{-1}, ref. Marquardt and Miyagi, 2015) and that samples were deformed by similar processes and hence are described by the same stress exponent (3 - 5). However, deviations from these assumptions were tested (see Extended Data Table 7.1). Under these assumptions, the calculated viscosity ratios are independent of the values chosen for mantle stress and strain rate, and only mildly sensitive to the chosen stress exponent (Figure 7.3, see also methods).

Figure 7.3 shows two endmember scenarios assuming either uniform strain rate or stress throughout the aggregate. Figure 7.3 a reflects a situation where the rock deforms as a whole and strain rate is uniform, a situation that is characteristic for a load-bearing framework (LBF) type deformation. Figure 7.3 b reflects a situation where strain partitions in the weaker phase and stress is thus equally distributed between the phases, a situation that is characteristic for an interconnected weak layer (IWL) type deformation. Cubic $CaSiO_3$perovskite is always the weakest mantle phase and often shows a viscosity that is several orders of magnitude smaller as compared to bridgmanite and ferropericlase. At 1000 km depths, corresponding to a pressure of about 40 GPa where experimental results for all phases are available, we find cubic $CaSiO_3$ to have a viscosity that is 1.4 to 4 orders of magnitude lower as compared to bridgmanite and 1 to 3 order of magnitude lower than ferropericlase (for $n = 3$). The viscosity contrast is particularly pronounced for the IWL scenario, which is likely to develop in large strain regions of the mantle. To test the robustness of our findings, we evaluated the effect of assuming different experimental strain rates and stress exponents for bridgmanite, ferropericlase, and $CaSiO_3$ perovskite (see Methods). We found that viscosities consistently increased from $CaSiO_3$ perovskite to ferropericlase to bridgmanite for a wide range of model parameters. We note that the calculation of viscosity contrasts by necessity involves several assumptions and relies on poorly constrained parameters as detailed in Methods, future experimental and theoretical work might aim to better quantify these. The presence of hydrogen in the lower mantle might further affect the rheological

behavior of $CaSiO_3$ perovskite (and bridgmanite), even though a recent study showed that the effect might be rather small (Muir and Brodholt, 2018).

The presence of weak cubic $CaSiO_3$perovskite has wide-ranging consequences for the dynamics of subducting slabs and the interpretation of seismic observations. The formation of $CaSiO_3$ perovskite from majoritic garnet, a comparably hard phase (Kavner et al., 2000), at around 550 km depth in subducted oceanic crust (Saikia et al., 2008) will lead to a substantial weakening of the oceanic crust. Previous works on two-phase deformation of a bridgmanite–ferropericlase assemblage, a proxy for a lower mantle rock, have predicted that strain starts to partition into the weak ferropericlase that can form an IWL network during deformation, thereby lowering the viscosity of the two-phase assemblage by several orders of magnitude (Takeda, 1998a; Yamazaki and Karato, 2001b; Marquardt and Miyagi, 2015; Girard et al., 2016; Thielmann et al., 2020). However, the onset of strain localization largely depends on the viscosity contrast between the phases and the volume fraction of the weak phase (Thielmann et al., 2020). Our results suggest that the viscosity contrast between bridgmanite and cubic $CaSiO_3$ perovskite is substantially larger as compared to the one between bridgmanite and ferropericlase. Moreover, the volume fraction of $CaSiO_3$ perovskite in subducted oceanic crust is larger than the ferropericlase fraction in a pyrolitic lower mantle rock.

Taken this together, we expect strain localization to occur in subducted oceanic crust after the onset of cubic $CaSiO_3$ perovskite formation. $CaSiO_3$ perovskite gradually forms with depths from majoritic garnet and its volume fraction continuously increases between about 500 km and 700 km depth (Saikia et al., 2008). Once the interconnection volume threshold is reached and the accumulated strain is sufficiently large, strain will start to partition between phases and an IWL network will develop, leading to marked weakening of the crustal part of the subducted slab. Deformation of the crust will initially be governed by a LBF of the hard phase(s), which depending on depth are majoritic garnet, bridgmanite, and stishovite (Hunt et al., 2019). In this scenario, the effective viscosity contrast can be approximated by a constant strain rate assumption (Figure 7.3 a). With increasing deformation, strain will start to partition into the weak $CaSiO_3$ phase, leading to rock weakening and initiating a continuous transition towards a deformation scenario where stress is equally distributed between all phases (Figure 7.3 b). The increase in effective viscosity contrasts between the phases that is caused by this transition will accelerate strain partitioning, further weakening the subducted crust.

Since we expect cubic $CaSiO_3$ perovskite to form and strain to build up from around 550 km depth, we speculate that the strain weakening effect in subducted oceanic crust will already be significant at the time of bridgmanite and ferropericlase formation at around 660 km depth in the surrounding mantle. The weak layer of subducted oceanic crust would thus be sandwiched between comparably hard mantle rocks and could easily be separated from the surrounding

mantle by shear forces (Van Keken et al., 1996), similar to weak sediments in the shallower parts of subduction zone. At depths between 660 km and 720 km depths, basaltic oceanic crust is less dense than ambient mantle (Hirose et al., 1999), but below about 720 km, after garnet has completely dissolved into perovskite-structured phases, oceanic crust becomes denser than ambient mantle (Hirose et al., 1999, 2005). Depending on the depth-dependent buoyancy contrast to the surrounding mantle, low-viscosity oceanic crust could thus segregate and accumulate around 660 km depth or migrate towards the core-mantle boundary, behaving like an "upside-down plume". The low viscosity of cubic $CaSiO_3$ perovskite provides an intrinsic mechanism to separate slab materials and to accumulate recycled oceanic crust either at the boundary between the upper and lower mantle or at the core-mantle boundary, where cubic $CaSiO_3$ perovskite may contribute to seismically observed regions of low shear wave velocities in the uppermost lower mantle (Ballmer et al., 2015) as well as the LLSVPs beneath Africa and the Pacific as hypothesized earlier (Garnero et al., 2016; Thomson et al., 2019; Jones et al., 2020). Deep recycling of oceanic crust has further been inferred to contribute to the geochemical diversity observed in ocean island basalts at the surface (Hofmann, 1997).

The above-mentioned implications require the presence of cubic $CaSiO_3$ perovskite and hence the tetragonal-cubic transition to occur at temperatures below the geotherm (Komabayashi et al., 2007; Thomson et al., 2019). If lower mantle $CaSiO_3$ perovskite contains titanium or aluminium as suggested by the analysis of a diamond inclusion (Nestola et al., 2018), the tetragonal-cubic transition is shifted to higher temperatures (Kurashina et al., 2004; Komabayashi et al., 2007; Thomson et al., 2019), possibly intersecting a cold subduction geotherm (Thomson et al., 2019). The tetragonal-cubic transition could then lead to sudden changes of rheological properties which would affect the dynamic behavior of a subducting slab, possibly leading to slab buckling, delamination and/or stagnation. The dependence of this dynamic change on the availability of titanium and aluminum could help explain the diverse behavior of slabs in the lower mantle (Fukao and Obayashi, 2013). Details of the interaction of a weak subducting crust, as indicated by our experiments, with the surrounding mantle should be explored by future geodynamic modelling, as should be the effect of the presence of an Al-bearing phase in subducted oceanic crust that might further complicate slab rheology.

References

Ballmer, M. D., Schmerr, N. C., Nakagawa, T. & Ritsema, J. (2015). Earth Sc Iences: Compositional mantle layering revealed by slab stagnation at ~1000-km depth. *Science Advances* **1**, 1–9.

Couper, S., Speziale, S., Marquardt, H., Liermann, H. P. & Miyagi, L. (2020). Does Heterogeneous Strain Act as a Control on Seismic Anisotropy in Earth's Lower Mantle? *Frontiers in Earth Science* **8**.

Ferré, D., Carrez, P. & Cordier, P. (2009a). Peierls dislocation modelling in perovskite (CaTiO3): Comparison with tausonite (SrTiO3) and MgSiO3 perovskite. *Physics and Chemistry of Minerals* **36**.

Ferré, D., Cordier, P. & Carrez, P. (2009b). Dislocation modeling in calcium silicate perovskite based on the Peierls-Nabarro model. *American Mineralogist* **94**.

Fukao, Y. & Obayashi, M. (2013). Subducted slabs stagnant above, penetrating through, and trapped below the 660 km discontinuity. *Journal of Geophysical Research: Solid Earth* **118**, 5920–5938.

Garnero, E. J., McNamara, A. K. & Shim, S.-H. (2016). Continent-sized anomalous zones with low seismic velocity at the base of Earth's mantle. *Nature Geoscience*. Nature Publishing Group **9**, 481–489.

Girard, J., Amulule, G., Farla, R., Mohiuddin, A. & Karato, S. (2016). Shear deformation of bridgmanite and magnesiowüstite aggregates at lower mantle conditions. *Science* **351**, 144–147.

Goryaeva, A. M., Carrez, P. & Cordier, P. (2015). Modeling defects and plasticity in MgSiO3 post-perovskite: Part 2—screw and edge [100] dislocations. *Physics and Chemistry of Minerals* **42**.

Gréaux, S., Irifune, T., Higo, Y., Tange, Y., Arimoto, T., Liu, Z. & Yamada, A. (2019). Sound velocity of CaSiO 3 perovskite suggests the presence of basaltic crust in the Earth's lower mantle. *Nature* **565**, 218–221.

Hirose, K., Fei, Y., Ma, Y. & Mao, H. K. (1999). The fate of subducted basaltic crust in the Earth's lower mantle. *Nature* **397**.

Hirose, K., Sinmyo, R. & Hernlund, J. (2017). Perovskite in Earth's deep interior. *Science*.

Hirose, K., Takafuji, N., Sata, N. & Ohishi, Y. (2005). Phase transition and density of subducted MORB crust in the lower mantle. *Earth and Planetary Science Letters* **237**.

Hofmann, A. (1997). Mantle geochemistry: the message from oceanic volcanism. *Nature* **385**, 219–229.

Hunt, S. A., Whitaker, M. L., Bailey, E., Mariani, E., Stan, C. V. & Dobson, D. P. (2019). An Experimental Investigation of the Relative Strength of the Silica Polymorphs Quartz, Coesite, and Stishovite. *Geochemistry, Geophysics, Geosystems* **20**.

Immoor, J., Marquardt, H., Miyagi, L., Lin, F., Speziale, S., Merkel, S., Buchen, J., Kurnosov, A. & Liermann, H. P. (2018). Evidence for {100}<011> slip in ferropericlase in Earth's lower mantle from high-pressure/high-temperature experiments. *Earth and Planetary Science Letters*. Elsevier B.V. **489**, 251–257.

Immoor, J., Marquardt, H., Miyagi, L., Speziale, S., Merkel, S., Schwark, I., Ehnes, A. & Liermann, H. (2020). An improved setup for radial diffraction experiments at high pressures and high temperatures in a resistive graphite-heated diamond anvil cell An improved setup for radial diffraction experiments at high pressures and high temperatures in a resistive grap. *Review of Scientific Instruments*. AIP Publishing, LLC **045121**, 045121-1-045121–7.

Irifune, T. & Klemme, S. (2007). Mineralogy of the Earth - Phase Transitions and Mineralogy of the Lower Mantle. *Treatise on Geophysics*.

Jones, T. D., Maguire, R. R., van Keken, P. E., Ritsema, J. & Koelemeijer, P. (2020). Subducted oceanic crust as the origin of seismically slow lower-mantle structures. *Progress in Earth and Planetary Science* **7**.

Kavner, A., Sinogeikin, S. V., Jeanloz, R. & Bass, J. D. (2000). Equation of state and strength of natural majorite. *Journal of Geophysical Research: Solid Earth* **105**.

Komabayashi, T., Hirose, K., Sata, N., Ohishi, Y. & Dubrovinsky, L. S. (2007). Phase transition in CaSiO3 perovskite. *Earth and Planetary Science Letters* **260**, 564–569.

Kurashina, T., Hirose, K., Ono, S., Sata, N. & Ohishi, Y. (2004). Phase transition in Al-bearing CaSiO3 perovskite: Implications for seismic discontinuities in the lower mantle. *Physics of*

the Earth and Planetary Interiors **145**.
Marquardt, H. & Miyagi, L. (2015). Slab stagnation in the shallow lower mantle linked to an increase in mantle viscosity. *Nature Geoscience* **8**, 311–314.
Merkel, S. (2002). Deformation of polycrystalline MgO at pressures of the lower mantle. *Journal of Geophysical Research* **107**, 2271.
Merkel, S., Wenk, H. R., Badro, J., Montagnac, G., Gillet, P., Mao, H. K. & Hemley, R. J. (2003). Deformation of (Mg0.9,Fe0.1)SiO3 Perovskite aggregates up to 32 GPa. *Earth and Planetary Science Letters* **209**, 351–360.
Miyagi, L., Merkel, S., Yagi, T., Sata, N., Ohishi, Y. & Wenk, H. R. (2009). Diamond anvil cell deformation of CaSiO3 perovskite up to 49 GPa. *Physics of the Earth and Planetary Interiors* **174**, 159–164.
Muir, J. M. R. & Brodholt, J. P. (2018). Water distribution in the lower mantle: Implications for hydrolytic weakening. *Earth and Planetary Science Letters* **484**.
Nestola, F. *et al.* (2018). CaSiO3 perovskite in diamond indicates the recycling of oceanic crust into the lower mantle. *Nature* **555**.
Saikia, A., Frost, D. J. & Rubie, D. C. (2008). Splitting of the 520-kilometer seismic discontinuity and chemical heterogeneity in the mantle. *Science* **319**.
Shieh, S. R., Duffy, T. S. & Shen, G. (2004). Elasticity and strength of calcium silicate perovskite at lower mantle pressures. *Physics of the Earth and Planetary Interiors* **143**.
Sun, N., Mao, Z., Yan, S., Wu, X., Prakapenka, V. B. & Lin, J. F. (2016). Confirming a pyrolitic lower mantle using self-consistent pressure scales and new constraints on CaSiO3 perovskite. *Journal of Geophysical Research: Solid Earth* **121**.
Takeda, Y.-T. (1998). Flow in rocks modelled as multiphase continua: application to polymineralic rocks. *Journal of Structural Geology* **20**, 1569–1578.
Thielmann, M., Golabek, G. J. & Marquardt, H. (2020). Ferropericlase Control of Lower Mantle Rheology: Impact of Phase Morphology. *Geochemistry, Geophysics, Geosystems* **21**.
Thomson, A. R., Crichton, W. A., Brodholt, J. P., Wood, I. G., Siersch, N. C., Muir, J. M. R., Dobson, D. P. & Hunt, S. A. (2019). Seismic velocities of CaSiO3 perovskite can explain LLSVPs in Earth's lower mantle. *Nature*. Springer US **572**, 643–647.
Van Keken, P. E., Karato, S. & Yuen, D. A. (1996). Rheological control of oceanic crust separation in the transition zone. *Geophysical Research Letters* **23**.
Yamazaki, D. & Karato, S. (2001). Some mineral physics constraints on the rheology and geothermal structure of Earth's lower mantle. *American Mineralogist* **86**, 385–391.

Acknowledgements

We acknowledge technical assistance by A. Ehnes and I. Schwark. We thank Andrew Thomson for providing a table with the high-temperature shear modulus of $CaSiO_3$ perovskite. This research was supported through the German Science Foundation (grants MA4534/3-1 and MA4534/4-1) as well the European Union's Horizon 2020 research and innovation Programme (ERC grant 864877). HM acknowledges support from the Bavarian Academy of Sciences. LM acknowledges support from CDAC and NSF (EAR-0337006 and EAR-1654687).

HM, HPL, LM, SS designed the research. JI prepared the experiments. All author contributed to the Synchrotron experiments. JI and LM analysed the data. HM performed the modelling. HM

wrote the initial draft of the manuscript. All authors contributed to the final writing of the manuscript.

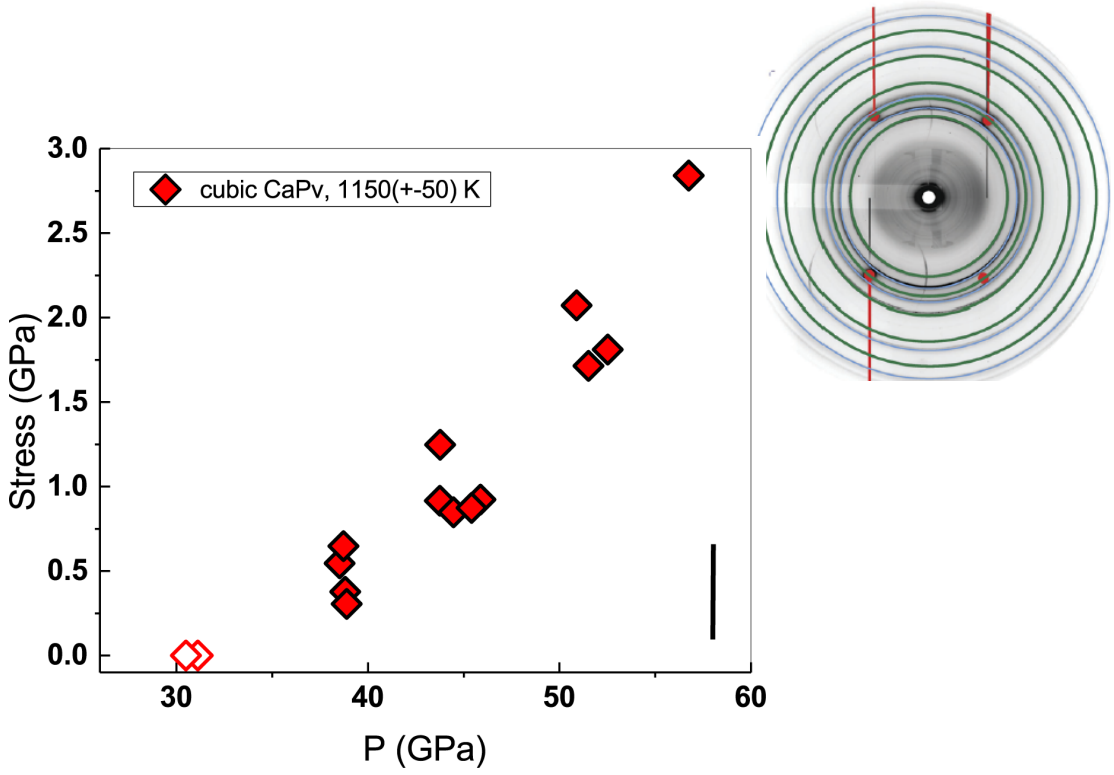

Figure 7.1: **Deviatoric stress measured in cubic $CaSiO_3$ perovskite at lower mantle pressures and T = 1150(±50) K.** Texture development is observed from 39 GPa (see Methods), indicating plastic flow. Inset shows a typical diffraction pattern collected after in-situ high-pressure/high-temperature synthesis of cubic $CaSiO_3$ perovskite in the diamond-anvil cell showing Debye rings of cubic $CaSiO_3$ (green colored rings) and platinum (blue colored rings). Open symbols denote data that have been collected shortly after synthesis and have been excluded from the strength calculation. The size of the experimental errors, propagated from the uncertainties in measured Q-values, is indicated by the bar in the lower right corner.

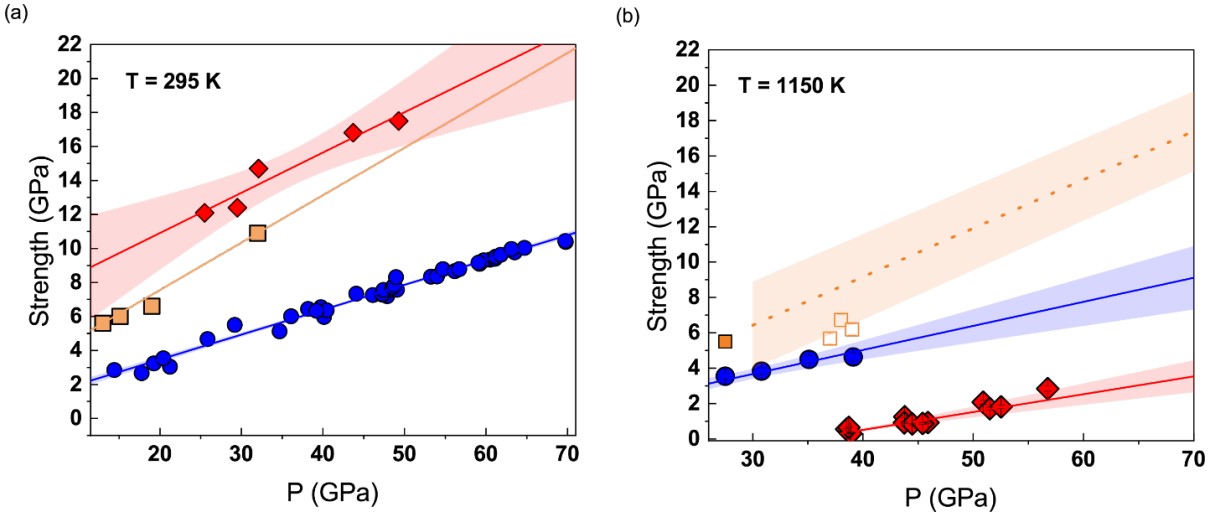

Figure 3.6: Strength of major lower mantle phases at high pressures. (a) strength values measured at room temperature by previous works. Red: tetragonal $CaSiO_3$ perovskite (Miyagi et al., 2009); orange: $Mg_{0.9}Fe_{0.1}SiO_3$ bridgmanite (Merkel et al., 2003); blue: $(Mg_{0.8}Fe_{0.2})O$ ferropericlase (Marquardt and Miyagi, 2015). (b) Here-derived high-temperature strength of cubic $CaSiO_3$ perovskite at lower mantle pressures (red solid diamonds) compared to the strength of $(Mg_{0.8}Fe_{0.2})O$ measured at 1150 K (blue solid circles) (Immoor et al., 2018) and the stress measured on bridgmanite deformed as part of a multi-phase assemblage at 1000 K at comparably low strains, likely representing a lower bound to the high-temperature strength of bridgmanite (Couper et al., 2020) (open squares). The solid orange square denotes the strength of bridgmanite at 2750 K, taken from Girard et al., 2016 (their run "gamma 25"). Best-fit lines are shown along with their 95 % confidence range. Given the limited amount of data on the high-temperature strength reported for bridgmanite, the strength of bridgmanite at 1150 K was derived from the data measured for bridgmanite at 295 K (Merkel et al., 2003) by applying two different temperature corrections represented by the shaded region (see Methods). Even though we acknowledge that this procedure is uncertain, the overlap of our derived range with the data collected on two-phase samples (squares) suggest that it provides a reasonable estimate.

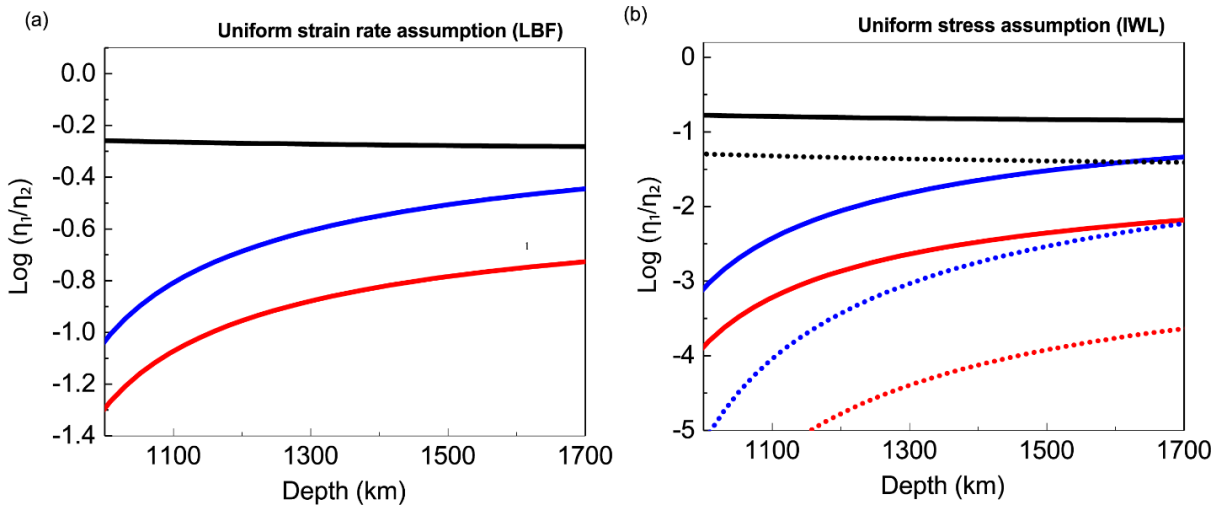

Figure 7.2: Depth-dependent viscosity contrast between major lower mantle phases at ~1150 K. The viscosity contrast is shown for pairs of mantle phases of viscosity η_1 and η_2. Red curve: η_{CaSiO3}/η_{Bm}; Blue curve: η_{CaSiO3}/η_{Fp}; Black curve: η_{Fp}/η_{Bm}. (a) viscosity contrast calculated under the assumption that strain rate is equal in both phases. This assumption represents the stage of initial deformation which is dominated by a load-bearing framework (LBF) of the harder phase. (b) Viscosity contrast calculated for a uniform stress assumption, representing a scenario of progressed deformation that has led to the development of an interconnected weak layer (IWL) of the weak phase. Calculations have been performed with a stress exponent n = 3 (solid curves) and n = 5 (dotted curves).

Supplementary Material

Methods:

Experimental details:

A resistive-heated diamond-anvil cell (DAC), based on a customised Mao-Bell type DAC and designed for radial x-ray diffraction experiments, was used for the experiments (Immoor et al., 2020). Diamonds with culet sizes of 300 µm were employed, together with a gasket made of an amorphous boron epoxy mixture that was inserted in a Kapton foil. A resistive-heater that surrounds the diamond tips was made of two thin flexible graphite layers that are in tight contact with the diamond anvils. To allow x-rays to pass through the heater, a beam path was carved into the graphite sheets (Liermann et al., 2009; Immoor et al., 2020). The entire DAC was positioned inside a vacuum chamber designed at the Extreme Condition Beamline (ECB, P02.2) at PETRA III of the Deutsches Elektronen Synchrotron (DESY) (Liermann et al., 2015; Immoor et al., 2020). During the experiments, a vacuum of better then 10^{-4} mbar was maintained to avoid oxidation of the cell and diamonds. The outside of the vacuum chamber was kept at low temperatures by a water-cooling system (Liermann et al., 2015; Immoor et al., 2020). The starting material was finely-ground powder of $CaSiO_3$ wollastonite mixed with a small amount of fine-powdered platinum to determine the experimental pressure employing previously published thermal equation of state parameters (Fei et al., 2007b). The sample was heated at a pressure of ~30 GPa, until the appearance of new diffraction rings indicated the formation of $CaSiO_3$ perovskite (Figure 7.1). Temperature was increased slowly (hours) to allow the system to equilibrate and maintain the vacuum. Pressure was then increased at a constant temperature of 1150(±50) K, leading to the deformation of the sample. Temperature was determined as the average of the measurement of two thermocouples placed between the heater and below the gasket (Immoor et al., 2020), with the given uncertainty reflecting the difference between the two measurements. Pressure was increased remotely using a gas-membrane system and diffraction images were taken after pressure stabilized. X-ray diffraction experiments were performed at the Extreme Conditions Beamline (ECB) P02.2 at PETRA III at DESY (Liermann et al., 2015). X-rays with an energy of 25 keV were focused to 8 (h) x 3 (v) µm². The diffraction images were recorded on a Perkin Elmer XRD 1621 flat panel detector, sliced using Fit2d software (Hammersley et al., 1996) and analyzed using the software package MAUD (Lutterotti et al., 1997) (Extended Data Figure 7.1). The "radial diffraction in the DAC" model (Singh et al., 1998) was used to fit lattice strains (110, 111, 200, 211 reflections) in $CaSiO_3$ perovskite. The E-WIMW model which is similar to the WIMV model (Matthies and Vinel, 1982), but allows for incomplete and arbitrary pole figure

coverage was employed to fit textures. Cylindrical symmetry was imposed. The orientation distribution function (ODF) was exported to BEARTEX (Wenk et al., 1998) to plot Inverse Pole Figures (IPF). Derived lattice strains and texture evolution are shown in extended data Figure 7.2 and 7.3. A clear texture development is observed throughout the experiment, where texture strength increased from 1.5 multiples of random distribution (mrd) after synthesis to about 1.75 mrd at the highest pressures. It is important to note that both the sample's strength and texture are derived from the same set of grains sampled by the x-rays. It is therefore not possible by experimental design that some highly stressed grains that cause texture development are missing from our strength measurement.

Visco-Plastic Self-Consistent (VPSC) Modelling of Texture Development

We performed Visco-Plastic Self-Consistent (VPSC) simulations (Lebensohn and Tomé, 1993) to model slip system activites and to determine the amount of plastic strain required to reproduce the experimentally measured increase of texture strength (Extended Data Figure 7.4). Simulations were performed using VPSC version 6 with a tangent approximation for the inclusion matrix interaction. The starting texture was discretized into 3000 grains from the experimentally measured ODF at 31.1 GPa. This was then used as the starting texture for plasticity simulations. Different amounts of strain were applied in the simulation until the texture strength measured at 52.2 GPa was reproduced by the model. The best-fit model required 20% plastic strain with dominant 110 slip (79 % of total strain is on 110).

Modelling of the strength of bridgmanite at 1150 K and lower mantle pressures:

In absence of direct measurements of the plastic strength of single-phase bridgmanite at relevant pressures and high temperatures, we applied a temperature correction to 295 K DAC experiments (Merkel et al., 2003). We used the average value of two different approaches, where (1) the effect of temperature on the strength of bridgmanite is assumed to be the same as that measured for ferropericlase, (2) the 295 K results were shifted to lower strength values to match those measured for bridgmanite deformed in a DAC within a multi-phase assemblage (Couper et al., 2020).

Modelling of viscosity contrast between lower mantle phases:

We used our experimental data to calculate viscosity contrasts between major lower mantle phases using the identities:

$$\dot{\varepsilon} = A \cdot \sigma^n \tag{7.1}$$

and

$$\eta = \sigma/2\dot{\varepsilon} \tag{7.2}$$

Here, η is viscosity, $\dot{\varepsilon}$ is the strain rate, σ is stress, n is the stress exponent, and A is a pre-factor.

The above relations can be combined to calculate the viscosity contrast between any two phases (denoted by subscripts) for either a uniform stress or uniform strain rate scenario, according to:

$$\frac{\eta_1}{\eta_2} = \frac{\dot{\varepsilon}_2 \cdot {\sigma_1}^{n_1}}{\dot{\varepsilon}_1 \cdot {\sigma_2}^{n_2}} \cdot \sigma_g^{(n_2 - n_1)} \quad \text{(for uniform geophysical stress } \sigma_g\text{)} \tag{7.3}$$

$$\frac{\eta_1}{\eta_2} = \frac{{A_2}^{\left(\frac{1}{n_2}\right)}}{{A_1}^{\left(\frac{1}{n_1}\right)}} \cdot \dot{\varepsilon}_g^{\left(\frac{1}{n_1} - \frac{1}{n_2}\right)} \quad \text{(for uniform geophysical strain rate } \dot{\varepsilon}_g\text{)} \tag{7.4}$$

Under the assumption that the strain rates in all experiments were the same and samples deformed by similar processes and hence are described by the same stress exponent n, the above equations can be simplified to

$$\frac{\eta_1}{\eta_2} = \left(\frac{\sigma_1}{\sigma_2}\right)^n \quad \text{(for uniform geophysical stress)} \tag{7.5}$$

$$\frac{\eta_1}{\eta_2} = \frac{\sigma_1}{\sigma_2} \quad \text{(for uniform geophysical strain rate)} \tag{7.6}$$

To test the effect of this simplification on the here-derived viscosity contrasts (Figure 7.3), we used equations (7.3) and (7.4) to test the effect of different stress exponents for the three mantle minerals and differences in experimental strain rates over a relevant range. The results are

summarized in Extended Data Table 7.1. We find that cubic $CaSiO_3$ consistently shows a lower viscosity than both bridgmanite and ferropericlase, often by several orders of magnitude. It shows a particularly low viscosity in our uniform stress models.

Extended Data:

Extended Data Table 7.1: Viscosity contrast between $CaSiO_3$ perovskite and bridgmanite (left) or ferropericlase (right) calculated from strength values at 40 GPa and ~1150 K (see Figure 7.2 b). The effect of varying the stress exponent and experimental strain rate on calculated viscosity contrasts was tested. In calculating the values in the table, we assumed a stress exponent of 4 and an experimental strain rate of 10^{-4} s^{-1} for $CaSiO_3$. We further fixed the mantle stress to 10 MPa and the mantle strain rate to 10^{-14} s^{-1} for calculations at uniform stress and strain rate, respectively.

$CaSiO_3$ perovskite / bridgmanite				$CaSiO_3$ perovskite / ferropericlase			
n_{Bm}	$\dot{\varepsilon}_{Bm}$ (s^{-1})	$LOG(\eta_{CaSiO3}/\eta_{Bm})$		n_{Fp}	$\dot{\varepsilon}_{Fp}$ (s^{-1})	$LOG(\eta_{CaSiO3}/\eta_{Fp})$	
		σ_g = constant	$\dot{\varepsilon}_g$ = constant			σ_g = constant	$\dot{\varepsilon}_g$= constant
3	10^{-3} – 10^{-5}	-5.9 to -3.9	-0.1 to -0.7	3	10^{-3} – 10^{-5}	-5.1 to -3.1	-0.5 to 0.2
4	10^{-3} – 10^{-5}	-5.8 to -3.8	-1.5 to -1.0	4	10^{-3} – 10^{-5}	-4.8 to -2.8	-1.2 to -0.7
5	10^{-3} – 10^{-5}	-5.8 to -3.8	-1.9 to -1.5	5	10^{-3} – 10^{-5}	-4.5 to -2.5	-1.7 to -1.3

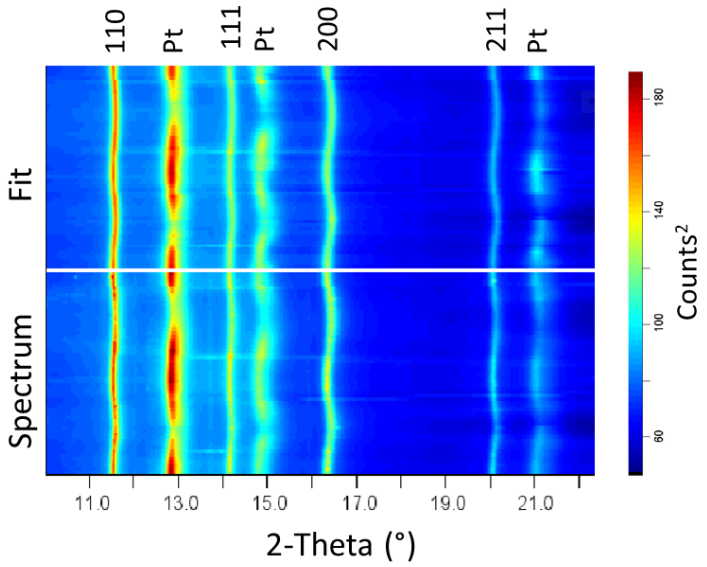

Extended Data Figure 7.1: Unrolled diffraction image collected at 52.5 GPa and 1150(±50) K (bottom) along with the best-fit model (top). The curvature is a measure of lattice strains and was used to calculate the strength of $CaSiO_3$ perovskite.

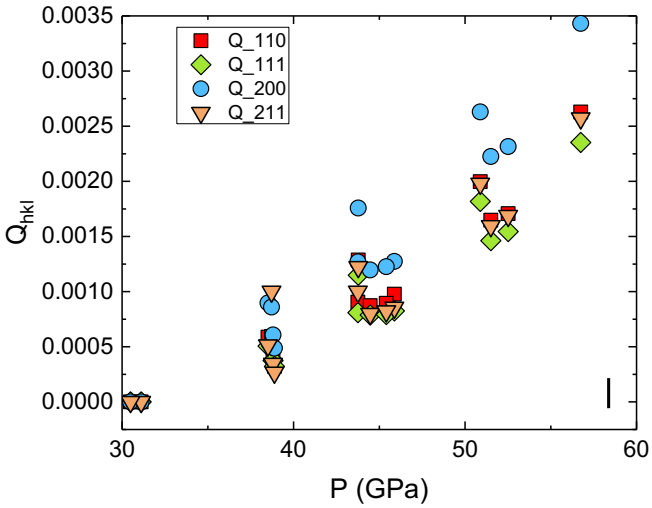

Extended Data Figure 7.2: Experimentally derived lattice strains of cubic $CaSiO_3$ at a temperature of 1150(±50) K. The error of the derived lattice strains is similar to the symbol sizes as shown in the lower right corner.

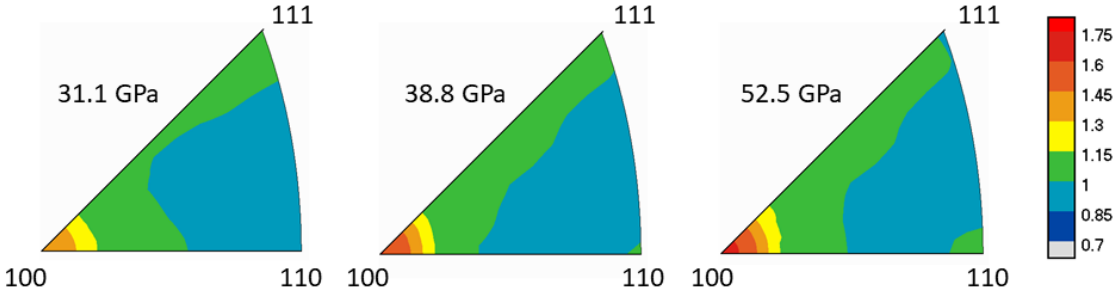

Extended Data Figure 7.3: Texture development observed in experiments. Texture strength is indicated by the colours. 100 texture increases with pressure throughout the experiment, increasing from about 1.5 mrd to 1.75 mrd, indicating plastic flow.

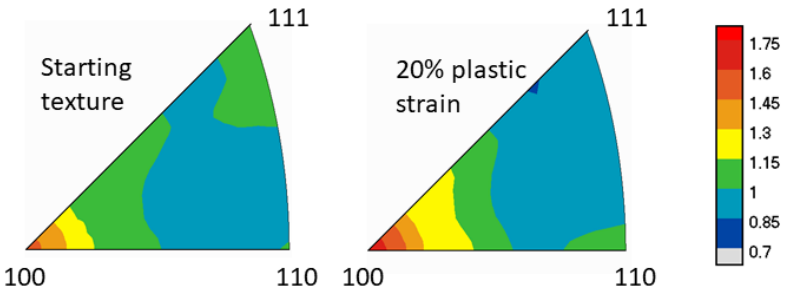

Extended Data Figure 7.4: VPSC modelling of texture development. The measured experimental texture after sample synthesis was used as starting texture. 20 % of plastic strain leads to a texture strength comparable to the one measured at 52.2 GPa (see Extended Data Figure 7.3).

References

Couper, S., Speziale, S., Marquardt, H., Liermann, H. P. & Miyagi, L. (2020). Does Heterogeneous Strain Act as a Control on Seismic Anisotropy in Earth's Lower Mantle? *Frontiers in Earth Science* **8**.

Fei, Y., Ricolleau, A., Frank, M., Mibe, K., Shen, G. & Prakapenka, V. (2007). Toward an internally consistent pressure scale. *Proceedings of the National Academy of Sciences* **104**, 9182–9186.

Hammersley, A. P., Svensson, S. O., Hanfland, M., Fitch, A. N. & Häusermann, D. (1996). Two-dimensional detector software: From real detector to idealised image or two-theta scan. *High Pressure Research* **14**.

Immoor, J., Marquardt, H., Miyagi, L., Speziale, S., Merkel, S., Schwark, I., Ehnes, A. & Liermann, H. (2020). An improved setup for radial diffraction experiments at high pressures and high temperatures in a resistive graphite-heated diamond anvil cell An improved setup for radial diffraction experiments at high pressures and high temperatures in a resistive grap. *Review of Scientific Instruments*. AIP Publishing, LLC **045121**, 045121-1-045121–7.

Lebensohn, R. A. & Tomé, C. N. (1993). A self-consistent anisotropic approach for the simulation of plastic deformation and texture development of polycrystals: Application to zirconium alloys. *Acta Metallurgica Et Materialia* **41**.

Liermann, H.-P., Merkel, S., Miyagi, L., Wenk, H.-R., Shen, G., Cynn, H. & Evans, W. J. (2009). Experimental method for in situ determination of material textures at simultaneous high pressure and high temperature by means of radial diffraction in the diamond anvil cell. *The Review of scientific instruments* **80**, 104501.

Liermann, H. P. *et al.* (2015). The Extreme Conditions Beamline P02.2 and the Extreme Conditions Science Infrastructure at PETRA III. *Journal of synchrotron radiation* **22**, 908–24.

Lutterotti, L., Matthies, S., Wenk, H.-R., Schultz, A. S. & Richardson, J. W. (1997). Combined texture and structure analysis of deformed limestone from time-of-flight neutron diffraction spectra. *Journal of Applied Physics*. AIP Publishing **81**, 594.

Matthies, S. & Vinel, G. W. (1982). On the Reproduction of the Orientation Distribution Function of Texturized Samples from Reduced Pole Figures Using the Conception of a Conditional Ghost Correction. *physica status solidi (b)* **112**.

Merkel, S., Wenk, H. R., Badro, J., Montagnac, G., Gillet, P., Mao, H. K. & Hemley, R. J. (2003). Deformation of (Mg0.9,Fe0.1)SiO3 Perovskite aggregates up to 32 GPa. *Earth and Planetary Science Letters* **209**, 351–360.

Singh, A. K., Balasingh, C., Mao, H. K., Hemley, R. J. & Shu, J. (1998). Analysis of lattice strains measured under nonhydrostatic pressure. *Journal of Applied Physics* **83**, 7567–7575.

Wenk, H. R., Matthies, S., Donovan, J. & Chateigner, D. (1998). BEARTEX: a Windows-based program system for quantitative texture analysis. *Journal of Applied Crystallography*. International Union of Crystallography **31**, 262–269.

(Eidesstattliche) Versicherungen und Erklärungen

(§ 9 Satz 2 Nr. 3 PromO BayNAT)

Hiermit versichere ich eidesstattlich, dass ich die Arbeit selbstständig verfasst und keine anderen als die von mir angegebenen Quellen und Hilfsmittel benutzt habe (vgl. Art. 64 Abs. 1 Satz 6 BayHSchG).

(§ 9 Satz 2 Nr. 3 PromO BayNAT)

Hiermit erkläre ich, dass ich die Dissertation nicht bereits zur Erlangung eines akademischen Grades eingereicht habe und dass ich nicht bereits diese oder eine gleichartige Doktorprüfung endgültig nicht bestanden habe.

(§ 9 Satz 2 Nr. 4 PromO BayNAT)

Hiermit erkläre ich, dass ich Hilfe von gewerblichen Promotionsberatern bzw. -vermittlern oder ähnlichen Dienstleistern weder bisher in Anspruch genommen habe noch künftig in Anspruch nehmen werde.

(§ 9 Satz 2 Nr. 7 PromO BayNAT)

Hiermit erkläre ich mein Einverständnis, dass die elektronische Fassung meiner Dissertation unter Wahrung meiner Urheberrechte und des Datenschutzes einer gesonderten Überprüfung unterzogen werden kann.

(§ 9 Satz 2 Nr. 8 PromO BayNAT)

Hiermit erkläre ich mein Einverständnis, dass bei Verdacht wissenschaftlichen Fehlverhaltens Ermittlungen durch universitätsinterne Organe der wissenschaftlichen Selbstkontrolle stattfinden können.

…….
Ort, Datum, Unterschrift